

Tidal Disruption of Substructure in Galaxy Clusters


by
Eric Hayashi
B.Sc. University of Guelph 1998

A Thesis Submitted in Partial Fulfillment of the
Requirements for the Degree of
MASTER OF SCIENCE
in the Department of Physics and Astronomy

We accept this thesis as conforming
to the required standard.




Dr. J. F. Navarro, Supervisor (Department of Physics & Astronomy)



Dr. F. D. A. Hartwick, Departmental Member (Department of Physics & Astronomy)



Dr. D. A. Harrington, Outside Member (Department of Chemistry)



Dr. T. R. Quinn, External Examiner (University of Washington)

© Eric Hayashi, 2001,
University of Victoria.

*All rights reserved. Thesis may not be reproduced in whole or in part,
by mimeograph or other means, without the permission of the author.*

Supervisor: Dr. J. F. Navarro

Abstract

Overmerging in the context of cosmological N -body simulations is defined as the absence of substructure in the dark matter halos of galaxy clusters due to numerical or physical disruption mechanisms. In early simulations of galaxy clusters the rapid disruption of bound clumps of N -body particles produced a smooth, featureless cluster mass distribution that did not resemble a real galaxy cluster, in which luminous matter is concentrated in discrete galaxies. We investigate recent claims (Ghigna *et al.*, 1998; Klypin, Gottlöber & Kravtsov, 1999) that the overmerging problem has been resolved in the latest generation of cosmological simulations simply as a result of increased numerical resolution. To this end we perform a series of simulations of the evolution of satellite halos in bound orbits within a static cluster potential in order to investigate the effects of varying mass and force resolution on the mass loss experienced by substructure due to tidal stripping. We find that satellites on radial orbits with apocentre-to-pericentre ratios greater than about 3:1 lose approximately the same fraction of their remaining mass each time they pass through pericentre. Conversely, tidal stripping of satellites on circular orbits is characterized by a sharp decline in mass during the first orbit followed by continuous mass loss at a reduced rate in subsequent orbits.

We use our results to test semi-analytic models for predicting mass loss and to establish a correlation between the disruption timescale of a satellite and the fraction of mass it loses during its first orbit. These tools are used to construct a toy model for the dynamical evolution of a galaxy cluster. We find that tidal disruption of satellites is sufficient to erase most substructure within the central regions of the cluster after a Hubble time. The number density of surviving substructure halos predicted by our model is compared with the results of cosmological simulations and observations from the Canadian Network for Observational Cosmology (CNOC) cluster survey.

The density profile of surviving satellite halos is similar to that of the Virgo cluster simulation of Ghigna *et al.* (1998), and is not consistent with the observed distribution of galaxies in the CNOc ensemble cluster.

We conclude that overmerging due to physical disruption mechanisms remains a problem in the central regions of cluster simulations. This suggests that a dissipational hydrodynamic component is needed to properly model the dynamics of galaxy cluster, as was originally proposed by White & Rees (1978).

Examiners:



Dr. J. F. Navarro, Supervisor (Department of Physics & Astronomy)



Dr. F. D. A. Hartwick, Departmental Member (Department of Physics & Astronomy)



Dr. D. A. Harrington, Outside Member (Department of Chemistry)



Dr. T. R. Quinn, External Examiner (University of Washington)

Contents

Abstract	ii
Contents	iv
List of Tables	v
List of Tables	vi
List of Figures	vi
List of Figures	vii
Acknowledgments	viii
1 Introduction	1
2 Tidal Stripping of Satellite Galaxies	5
2.1 <i>N</i> -body Basics	6
2.2 Simulations	10
2.2.1 Initial Conditions	11
2.2.2 Isolation Runs	13
2.2.3 Bound Orbits	18
2.3 Results	22
2.3.1 Mass Loss	24
2.3.2 Internal Structure	27
2.4 Modeling Mass Loss	29
2.4.1 Tidal Approximation	39
2.4.2 Impulse Approximation	43
2.4.3 Modeling Cumulative Mass Loss	46
2.5 Summary	51
3 Dynamical Evolution of Galaxy Clusters	54
3.1 Supplementary Simulations	55

3.1.1	Mass Loss	56
3.1.2	Disruption Timescale Predictions	61
3.2	A Toy Model for Cluster Evolution	68
3.3	Comparison with Other Work	75
3.4	Limitations and Future Work	82
3.5	Summary	83
4	Concluding Remarks	85
A	Properties of the NFW Model	88
	Bibliography	90

List of Tables

2.1	Softening lengths and relaxation times	17
2.2	Numerical parameters of our simulations	18
2.3	Error statistics for tidal and impulse approximation predictions . . .	46
2.4	Predicted and observed disruption times for three orbits	51
3.1	Numerical parameters of our simulations	56
3.2	Predicted and observed disruption times for 16 orbits	66

List of Figures

2.1	Density profile for unevolved halos	14
2.2	Cumulative energy profiles for optimally softened halos	15
2.3	Cumulative energy profiles for non-optimally softened halos	16
2.4	Mass shells of optimally softened halos	19
2.5	Mass shells of non-optimally softened halos	20
2.6	Positions of satellite particles projected in orbital plane	23
2.7	Time evolution of self-bound mass of satellite	26
2.8	Half-mass radius	30
2.9	Mean density within half-mass radius	31
2.10	Square of circular velocity at half-mass radius	32
2.11	Circular velocity profiles $r_{ap} = 300 r_s, r_{per} = 15 r_s$ orbit	33
2.12	Circular velocity profiles for $r_{ap} = 300 r_s, r_{per} = 30 r_s$ orbit	34
2.13	Circular velocity profiles for $r_{ap} = 300 r_s, r_{per} = 60 r_s$ orbit	35
2.14	Density profiles for $r_{ap} = 300 r_s, r_{per} = 15 r_s$ orbit	36
2.15	Density profiles for $r_{ap} = 300 r_s, r_{per} = 30 r_s$ orbit	37
2.16	Density profiles for $r_{ap} = 300 r_s, r_{per} = 60 r_s$ orbit	38
2.17	Tidal radius and mass and density within tidal radius	41
2.18	Tidal approximation predictions for optimally softened halos	42
2.19	Tidal approximation predictions for non-optimally softened halos	44
2.20	Impulse approximation predictions for optimally softened halos	47
2.21	Impulse approximation predictions for non-optimally softened halos	48
2.22	Cumulative mass loss predictions	52
3.1	Pericentric and apocentric radii of all orbits	57
3.2	Self-bound mass for orbits with $r_{per} = 15 r_s$	59
3.3	Self-bound mass for orbits with $r_{apo} = 300 r_s$	60
3.4	Self-bound mass for circular orbits	62
3.5	Cumulative mass loss predictions for radial orbits	64
3.6	Cumulative mass loss predictions for circular orbits	65
3.7	Impulse approximation predictions in first orbit	67

3.8	Disruption timescale versus self-bound mass	69
3.9	Orbital parameters of surviving satellites	72
3.10	Number density profile of surviving satellites	74
3.11	Number of surviving satellites as a function of time	76
3.12	Comparison of number density profile with Ghigna <i>et al.</i> (2000) . . .	77
3.13	Comparison of projected number density with CNOC cluster	80

Acknowledgments

This work would not have been possible without the guidance and financial support of my supervisor, Julio Navarro. I have benefited greatly from his insightful commentary and constructive criticism during the past two and a half years. I am grateful to Ann Gower for initially encouraging me to visit the University of Victoria as a potential graduate student. Thanks also to David Hartwick for making the coffee room an interesting place to be at 10:30 in the morning. Finally, I would like to thank the members of the faculty who contributed to the purchase of “manta,” the computer whose screen I have spent countless hours staring at for the past two years.

Many thanks are due to my fellow graduate students in both physics and astronomy for making life in the Elliot building bearable and even enjoyable at times. They remind me of a line from a Bob Dylan song: “strange how people who suffer together have stronger connections than people who are most content.” Many thanks to my officemate James Taylor for many useful (and, admittedly, some not so useful) discussions about mass loss and tidal tails, and more importantly for being interested and enthusiastic about my research even on days when I wasn’t. Special thanks to Dr. Stephen Gwyn for convincing me that I could finish writing my thesis in time to defend before the end of term. Thanks, Stephen - next margarita’s on me.

Most of all, I would like to thank my parents, Robert and Kay, for their generosity and support throughout my university years.

Chapter 1

Introduction

Abstract

The history of overmerging in cosmological N -body simulations is reviewed. In this context, overmerging is defined as the disruption of substructure in the mass distribution of galaxy clusters due to numerical effects or physical processes. Overmerging was observed in the first galaxy cluster simulations (White, 1976), and helped motivate the classic picture of galaxy formation by dissipational collapse of gas in the potential wells of massive dark matter halos (White & Rees, 1978).

Recent simulations of structure formation in the context of the cold dark matter (CDM) cosmology (Ghigna *et al.*, 1998; Klypin, Gottlöber & Kravtsov, 1999; Springel *et al.*, 2000) suggest that the overmerging problem can be solved by increasing the resolution of collisionless simulations, without including a dissipational component. This work explores that contention by considering the disruption timescales of substructure due to the primary mechanism of tidal disruption. To this end, numerous N -body simulations are performed in order to investigate the effects of varying mass and force resolution on the mass loss experienced by substructure halos on various orbits. We use these results to develop semi-analytic models which allow us to predict the disruption timescales of satellite halos in clusters and to subsequently construct a toy model for the dynamical evolution of a galaxy cluster. The spatial distribution of surviving substructure predicted by our model is compared with the results of cosmological simulations and observations of real galaxy clusters.

Over the past four decades, the formation of clusters of galaxies has been studied extensively with numerical simulations. The idea that galaxy clusters form as gravitational instabilities in an expanding universe is generally attributed to van Albada

(1961). Early simulations based on this scenario adopted a bottom-up approach to structure formation, assuming that galaxies had collapsed prior to the turnaround time of the cluster. Various authors including Aarseth (1963), Peebles (1970), and White (1976) adapted the N -body simulation method (pioneered by Aarseth to simulate stellar systems), to model clusters by evolving systems of several hundred point mass particles, representing galaxies, under their mutual gravitational interaction.

In particular, White (1976) noticed a peculiar absence of substructure in his 700 particle simulation of the Coma cluster. Groups of particles which had collapsed into tightly bound units were rapidly transformed into “amorphous,” relaxed systems as a result of tidal forces, merging of bound clumps, and dynamical friction, thereby producing a smooth, featureless cluster mass distribution at the final time. This was in stark contrast to the appearance of real galaxy clusters in which luminous matter is concentrated in discrete galaxies. In a classic paper, White & Rees (1978) suggested that gravitational physics alone is insufficient to accurately model the formation of galaxies and clusters. They proposed that dissipational collapse of gas in the potential wells of massive dark matter halos resulted in highly concentrated baryonic cores, capable of withstanding disruption by dynamical processes.

This solution to the so-called “overmerging” problem was the basis of a new paradigm for galaxy formation in a dark matter-dominated universe. By that time, observations of the velocity dispersion of galaxies in clusters, and of rotation curves of galaxies had provided strong evidence that as much as 90% of the matter in the universe is in the form of unseen, dark matter. While the nature of the dark matter remains one of the foremost unsolved questions in modern cosmology, the currently favoured theory is based on the cold dark matter (CDM) model originally proposed by Peebles (1982) and Blumenthal *et al.* (1984).¹

¹Cold dark matter is made up of massive, weakly interacting subatomic particles that move at relatively slow (nonrelativistic) speeds. It is “cold” in the sense that temperature is a macroscopic measure of the average speed of particles in an ordinary gas, i.e. a low temperature gas is made up

Throughout the 80's and early 90's, increasingly high resolution cluster simulations in the context of the CDM cosmological model continued to show very little substructure.² The cause of overmerging has been a matter of some debate in the literature. Carlberg (1994), for example, attributed the disruption of substructure to two-body heating of subhalos (substructure halos) by cluster halo particles. Moore, Katz, & Lake (1996), however, argued that the timescale for this process was much longer than a Hubble time given the mass and force resolution of cluster simulations at that time. These authors concluded that tidal heating by the cluster potential and impulsive heating by encounters between subhalos, possibly enhanced by insufficient force resolution, were primarily responsible for overmerging.

The situation changed dramatically with the advent of the latest generation of high resolution N -body simulations. Improvements in hardware and algorithmic advances have made possible simulations containing more than one million particles, and several groups have demonstrated that, with sufficient numerical resolution, one can resolve a wealth of substructure where none appeared at lower resolution (Ghigna *et al.*, 1998; Klypin, Gottlöber & Kravtsov, 1999; Springel *et al.*, 2000). Many hundreds of subhalos survive within the virialized region of cluster halos, and as a result, several authors have declared “an end to the overmerging problem.”

As always, the ultimate test of theory lies in agreement with observations. Recently, Klypin *et al.* (1999) and Moore *et al.* (1999) have pointed out that the number of low mass subhalos predicted by CDM simulations on galactic scales exceeds the number of observed satellites in our galaxy by a factor of 10 to 100. This may be a symptom of a finite cross-section of interaction between dark matter particles (Spergel & Steinhardt, 2000), or possibly an indication of suppressed star formation in the dark halos of dwarf galaxy-sized objects due to feedback (Binney, Gerhard, & Silk, 2001) or reionization of the intergalactic medium (Bullock *et al.*, 2000; Moore, 2001).

of slowly moving particles

²The reader is referred to Moore (2000) for “a brief history of ‘N’ and overmerging.”

We seek to further test the CDM paradigm for structure formation by addressing the question: is the distribution of substructure consistent with the observed distribution of galaxies in clusters? In a real galaxy cluster, for instance, the oldest and most massive elliptical galaxies often reside at the centre of the cluster where tidal forces are strongest. Naively one might expect the physical processes responsible for overmerging, namely tidal heating by the mean cluster potential, to be most effective at disrupting subhalos in the innermost regions of the cluster. By calculating the spatial distribution of substructure predicted by collisionless (dark matter only) N -body simulations in the limit of infinite numerical resolution, we hope to determine whether a dissipational baryonic component is indeed necessary to model the formation of galaxy clusters properly.

The structure of this thesis is as follows. In Chapter 2 we describe the set of simulations performed in order to investigate the influence of mass and force resolution on the tidal stripping of a satellite galaxy. We develop semi-analytic models for the mass loss experienced by satellites and use these in Chapter 3 to model the dynamical evolution of a galaxy cluster. The predictions of our model are subsequently compared with the results of high resolution cluster formation simulations and with observations of real galaxy clusters. We summarize the results of the present work and discuss possibilities for future work in Chapter 4.

Chapter 2

Tidal Stripping of Satellite Galaxies

Abstract

Tidal disruption of cluster substructure is investigated in a series of simulations of a satellite galaxy in a bound orbit within a static host potential. We represent both the galaxy and the cluster by spherical dark matter halos of the form proposed by Navarro, Frenk, & White (1996). Our procedure for generating initial conditions is described, and the effects of varying mass and force resolution on the evolution of the self-bound mass and the density profile of the satellite are investigated. We find that halos simulated with low mass resolution (less than ~ 1000 particles) are prematurely disrupted due to relaxation effects. Interestingly, the use of small softening lengths results in shorter two-body relaxation timescales which also leads to the premature disruption of halos. Satellite halos are repeatedly stripped of mass as they orbit in the tidal field of the cluster, losing a constant fraction of their remaining bound mass every pericentric passage until they are completely disrupted. This is in contrast to the standard tidal approximation which predicts that satellites are stripped down only to the tidal radius at pericentre and therefore avoid total disruption.

Mass loss due to tidal stripping is modeled by the tidal radius approximation and the impulse approximation, and the predictions of these methods are compared to the observed self-bound mass of the satellite. Both techniques provide reasonable predictions of mass loss on an orbit-by-orbit basis, with the impulse approximation being slightly more accurate, but also more computationally expensive than the tidal radius method. Similar results are obtained for cumulative mass loss predictions using exponential extrapolations of the tidal and impulse methods, as well as repeated applications of the impulse approximation.

Cosmological simulations of galaxy cluster formation represent an extremely complicated dynamical environment, consisting of an evolving cluster potential and hundreds of satellites constantly orbiting, merging and interacting with one another. In this chapter we describe a series of much simpler simulations comprised of a single satellite galaxy in a static cluster potential. The results of these simulations enable us to better understand the physical and numerical effects responsible for the disruption of substructure in cosmological simulations. We also use our simulation results to develop semi-analytic methods for modeling the mass loss experienced by satellite galaxies.

This chapter is organized as follows. In Section 2.1 we review some concepts relevant to N -body simulations and to the interpretation of their results. We describe our methods for generating initial conditions and for performing simulations in Section 2.2, and present the results of these simulations in Section 2.3. In Section 2.4 we use semi-analytic models based on the tidal radius and impulse approximation to predict the mass loss experienced by satellite halos. Finally, we discuss our findings in Section 2.5.

2.1 N -body Basics

Ideally one would like to model dark matter as a self-gravitating collisionless fluid whose evolution in phase space is described by the collisionless Boltzmann equation,

$$\frac{df}{dt} \equiv \frac{\partial f}{\partial t} + \mathbf{v} \cdot \nabla f - \nabla \Phi \cdot \frac{\partial f}{\partial \mathbf{v}} = 0, \quad (2.1)$$

where $f(\mathbf{x}, \mathbf{v}, t)$ is the distribution function of the system and the gravitational potential Φ is given by Poisson's equation:

$$\nabla^2 \Phi(\mathbf{r}, t) = 4\pi G \int f(\mathbf{r}, \mathbf{v}, t) d\mathbf{v}. \quad (2.2)$$

In practice, solving this seven-dimensional coupled system of equations numerically is computationally prohibitive, hence the N -body technique is employed. In essence, the N -body method is a Monte Carlo approach that uses a finite number of discrete particles to represent the smooth mass distribution of the dark matter. Particles interact gravitationally with one another, and their trajectories are calculated by integrating Newton's equations of motion.

Clearly, by its very nature this approach introduces collisional effects into simulations of a perfectly collisionless fluid. Close encounters between massive N -body particles can significantly deflect a particle's orbit from that of a test particle moving in the mean potential of a collisionless system. In addition, the Newtonian gravitational force between two particles, $F_{12} = Gm_1m_2/r_{12}^2$, becomes large at small separations, and extremely small timesteps are needed to accurately reproduce their trajectories. In order to reduce the computational expense due to close encounters and binaries, and to better approximate a collisionless system, a softened potential is usually introduced, e.g. the Plummer model:

$$\Phi(r) = -\frac{Gm}{\sqrt{r^2 + \epsilon^2}} \quad (2.3)$$

$$a(r) = -\frac{Gmr}{(r^2 + \epsilon^2)^{\frac{3}{2}}}, \quad (2.4)$$

where $a(r)$ is the acceleration, or force per unit mass, and ϵ is the softening length. In practice, a piecewise spline kernel is usually preferred since the Plummer model converges slowly to the Newtonian limit, whereas a spline softened potential is exactly Newtonian for $r > 2 \epsilon$:

$$\Phi(r) = -\frac{Gm}{\epsilon} \begin{cases} -\frac{7}{5} + \frac{2}{3}u^2 - \frac{3}{10}u^4 + \frac{1}{10}u^5 & 0 \leq u \leq 1 \\ -\frac{1}{15}u^{-1} - \frac{8}{3} + \frac{4}{3}u^2 - u^3 + \frac{3}{4}u^4 - \frac{1}{30}u^5 & 1 \leq u \leq 2 \\ \frac{1}{u} & u \geq 2 \end{cases} \quad (2.5)$$

$$a(r) = -\frac{Gm}{r^2} \begin{cases} \frac{4}{3}u^3 - \frac{6}{5}u^5 + \frac{1}{2}u^6 & 0 \leq u \leq 1 \\ -\frac{1}{15} + \frac{8}{5}u^3 - 3u^4 + \frac{6}{5}u^5 - \frac{1}{6}u^6 & 1 \leq u \leq 2 \\ 1 & u \geq 2 \end{cases} \quad (2.6)$$

where $u = r/\epsilon$.

Force softening effectively imposes a spatial resolution limit to an N -body simulation; on scales smaller than the softening length, results are generally untrustworthy. On the other hand, softening allows longer integration timesteps to be used and also minimizes collisional effects by increasing the two-body relaxation timescale of the simulated system. The two-body relaxation timescale is usually defined as the characteristic time for collisions to perturb a particle from the course it would take if the dark matter was smoothly distributed, as opposed to concentrated in particles. For a system of N point particles, this timescale is

$$t_{relax} = \frac{0.1N}{\ln N} t_{cross}, \quad (2.7)$$

where $t_{cross} = R/\sigma \sim \sqrt{R^3/GM}$ is the average crossing time of the system of size R , mass M and velocity dispersion σ (Binney & Tremaine, 1987).

For a softened system of particles, Thomas and Couchman (1992) and van Kampen (1995) find the relaxation timescale

$$t_{relax} = \frac{N}{8 \ln \Lambda} t_{cross}, \quad (2.8)$$

where $\ln \Lambda = \ln(b_{max}/b_{min})$ is the Coulomb logarithm, which contains the ratio of maximum and minimum impact parameters (Binney & Tremaine, 1987). In a softened system, the minimum impact parameter, $b_{min} \simeq 4\epsilon$ (Farouki & Salpeter, 1982), and the maximum impact parameter is equal to the size of the system, R . For a system of point masses, we have $\Lambda \sim N$ as in equation 2.7, so for the softened system we take

$\Lambda = \min(N, R/4\epsilon)$. Smaller softening values therefore correspond to larger values of the Coulomb logarithm and shorter relaxation timescales. The choice of softening length thus represents a balance between maximizing force resolution (small ϵ) and maximizing the relaxation timescale (large ϵ).

Mass resolution, i.e. the fraction of the total mass of the system invested in each N -body particle, is primarily a function of the total number of particles in the simulation. In practice this number is limited by computational issues such as the processing power available and the efficiency of the simulation code. For the past three decades, computational power has increased steadily at the exponential rate predicted by Moore's empirical law of computing (Moore, 1965). In addition, N -body codes have evolved significantly from the original direct summation methods which scale in numbers of operations as N^2 , to tree-based codes which incorporate approximations into the force computation in order to reduce the scaling to $N \log N$. N -body simulations have benefited greatly from these technological advancements to the point where $N \gtrsim 10^6$ simulations are now commonplace, where such resolution was at the very limit of computational feasibility only five years ago.

The number of particles needed to sufficiently sample the distribution function of a simulated system is highly problem-dependent. In order to resolve the innermost regions (within of dark matter halos in cosmological simulations, for example, Moore *et al.* (1998) find that $N > 10^7$ is required,¹ whereas a more modest number of particles is sufficient for a wide range of other problems. Presently, however, there exists no general theory to predict the minimum number of particles required for a robust solution. The traditional approach is to perform a series of simulations with increasing mass and force resolution and look for convergence in the results.

In addition to mass and force resolution, many technical aspects of the simulation code itself must also be considered, including the size of timesteps, the force accuracy,

¹This refers to the slope of the density profile within 10% of the virial radius of the centre of the cluster.

and the accuracy of the integrator (Lake *et al.*, 1995). Fortunately, a number of well-tested codes are available, some of which are parallelized in order to take advantage of massively parallel computer architectures.

Numerical effects clearly play a significant role in N -body simulations and must be considered when interpreting their results. Insufficient mass resolution and small softening values (small N and small ϵ) both contribute to short two-body relaxation timescales in softened systems, and therefore enhance the disruption of substructure in N -body simulations. We address these issues by performing convergence studies in which mass and force resolution are varied in a series of otherwise identical simulations.

2.2 Simulations

In this section we describe the set of simulations performed in order to investigate the influence of mass and force resolution on the tidal stripping of a cluster galaxy. All of these simulations were performed with Navarro's smoothed-particle hydrodynamics (SPH) code which uses a binary tree method to compute gravitational forces between N -body particles (Navarro & White, 1993). Note that our simulations are comprised of collisionless dark matter particles only, and make no use of the hydrodynamic aspect of the code. Time integration is performed using a second-order Runge-Kutta integrator and forces are softened with a spline kernel. Readers are encouraged to consult Navarro & White (1993) and Navarro & Benz (1990) for further technical details concerning this code. These simulations were performed on a Sun Ultra 2 workstation (300 MHz dual UltraSPARCII CPU, 1048 Mb memory) and require about one hour of CPU time to evolve a 3000 particle halo in isolation for 10 crossing times, and about five CPU hours to evolve such a halo for 10 orbits in a static cluster potential.

2.2.1 Initial Conditions

We assume that dark matter halos are characterized by the universal density profile proposed by Navarro, Frenk, & White (1996; 1997), hereafter NFW:

$$\rho(r) \propto \frac{1}{r/r_s(1+r/r_s)^2} \quad (2.9)$$

where r_s is a characteristic scale radius. The corresponding mass and energy profiles and other relevant formulae are presented in Appendix A. The following procedure based on the transformation method for generating nonuniform random deviates (Press *et al.*, 1992) was used to initialize the spatial coordinates of halo particles:²

- generate a positive uniform random deviate, $0 < x_1 < 1$, and multiply by the total mass of the halo which is imposed by truncating the divergent NFW mass profile at some finite cutoff radius.
- solve the inverse function of the cumulative NFW mass profile $M(r)$ for the radius corresponding to this random mass, $m_{ran} = x_1 m_{tot}$:

$$r = M^{-1}(m_{ran}) \quad (2.10)$$

- assume spherical symmetry and supply two additional uniform random deviates, x_2 and x_3 , to generate the remaining two orthogonal coordinates

$$\phi = 2\pi x_2 \quad (2.11)$$

$$\theta = \cos^{-1}(2x_3 - 1) \quad (2.12)$$

²Initial conditions are trivially generated for density profiles with known analytic solutions for the phase-space distribution function, e.g. the Hernquist profile (Hernquist, 1990). The semi-analytic distribution function presented by Widrow (2000) for the NFW model therefore represents an alternate method for initializing our halo particles.

Particle velocities are generated as in Hernquist (1993) by assuming isotropy and by drawing speeds from a Gaussian distribution whose dispersion is given by the spherical Jeans equation:

$$\overline{v_r^2} = \frac{1}{\rho(r)} \int_r^\infty \rho(r) \frac{d\Phi}{dr} dr \quad (2.13)$$

$$= \frac{1}{\rho(r)} \int_r^\infty \rho(r) \frac{GM(r)}{r^2} dr \quad (2.14)$$

Force softening is incorporated at this stage via a top-hat kernel, i.e. the mass of each particle is evenly distributed over the number of radial bins spanned by the softening length before calculating the cumulative mass profile, $M(r)$ in equation (2.14).

A single halo model was initialized with four different mass resolutions and two softening schemes. Mass resolution was varied by keeping the total mass fixed and varying the number of particles, N , with $N = 100, 300, 1000, 3000$. The value of the concentration parameter, c , equal to the ratio of the virial radius (in this case the imposed cutoff radius of the halo) to the characteristic scale radius, r_s , was chosen to be 10. The half-mass radius, $r_{1/2}$, for a halo with this cutoff and concentration is $\simeq 3.6 r_s$.

One set of halos was initialized using the softening scaling suggested by van Kampen (2000a):

$$\epsilon_{plummer} \approx \frac{r_{1/2}}{2 N^{1/3}} \quad (2.15)$$

where $r_{1/2}$ is the half-mass radius of the system. This scaling is based on maintaining a mean nearest particle distance greater than the interparticle separation for which the softened force is half its Newtonian value. Note that the factor of 2 in the denominator of this expression is appropriate for a Plummer softening, and varies slightly depending on the type of softening used, e.g. for spline softening, we find $\epsilon_{spline} \approx r_{1/2}/1.3 N^{1/3}$. The $1/N^{1/3}$ scaling, however, is independent of the form of softening, and effectively increases the two-body relaxation timescale of the system

by a factor of three over that of a system of point masses. Of course the relaxation time can be made arbitrarily large by increasing the softening value, but this results in inaccurate particle trajectories on scales smaller than the softening length and produces artificially extended and “cold” (low velocity dispersion) halos. The van Kampen scaling law suggests an upper limit to the softening length based on the estimated mean nearest neighbour separation of particles within the half-mass radius. We refer to halos initialized with a softening length equal to the right-hand side of equation (2.15) as being “optimally softened.”

A second set of halos was initialized with a single softening length, $\epsilon = 0.1 r_s$, in order to resemble the numerical environment of a cosmological simulation. We refer to these as “non-optimally” softened halos. Figure 2.1 shows the density profiles of halo realizations with each of the four different mass resolutions. Initial density profiles are independent of force resolution since varying the softening length changes only the velocity distribution of halo particles. The reduced chi-square statistic, $\chi_{red}^2 = \chi^2/N_{bins}$, where N_{bins} is the number of bins over which the density profile is calculated, is less than unity for all four realizations.

Kinetic and potential energy profiles for the optimally and non-optimally softened halo set are also shown in Figures 2.2 and 2.3, respectively. In all cases the “binding” radius, the radius at which the total energy of the halo becomes negative ($r \simeq 0.75 r_s$), is well-reproduced by the N -body halos. The softening values and two-body relaxation timescales for both sets of halos are shown in Table 2.1.

2.2.2 Isolation Runs

Each halo was evolved in isolation using vacuum boundary conditions for 10 crossing times in order to ensure that the system was in equilibrium. The average crossing time and other simulation parameters are defined in Table 2.2. The softening length for each simulation was set to the same softening value used in generating

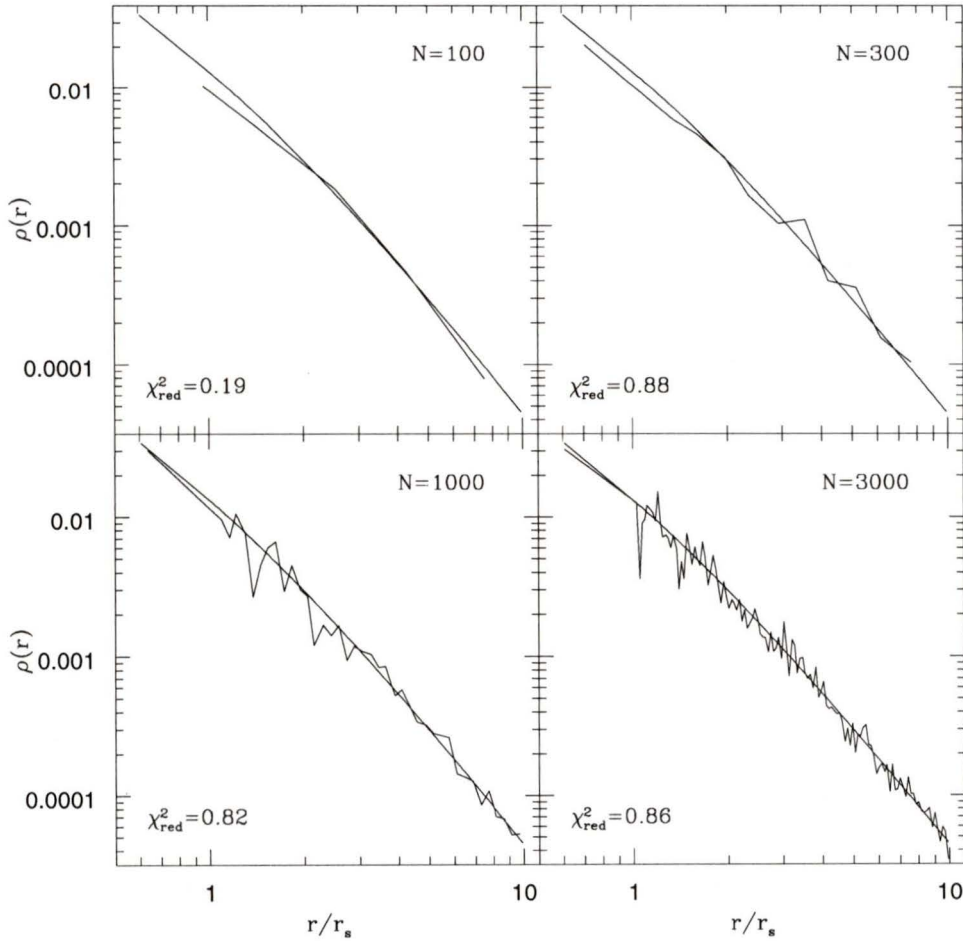


Figure 2.1: Density profiles for unevolved NFW halos with $N=100$, 300, 1000, and 3000 particles. Profiles are calculated by binning particles in spherical shells containing 25 particles each. Jagged solid line shows the density in each bin in units of m_{tot}/r_s^3 , plotted at the average radius of particles in that bin. Smooth solid line shows the corresponding analytic NFW profile. χ_{red}^2 is the chi-square statistic reduced by the number of bins.

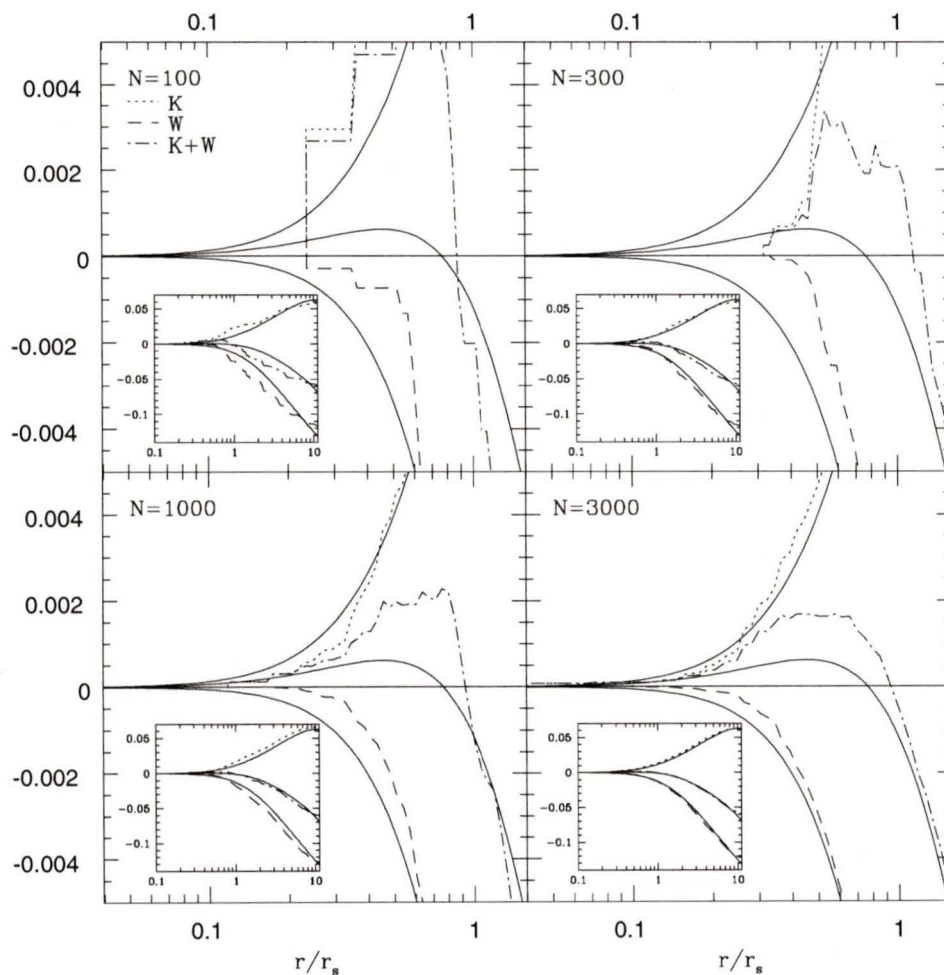


Figure 2.2: Cumulative kinetic (K), potential (W), and total (K+W) energy profiles for optimally softened unevolved NFW halos with $N=100$, 300, 1000, and 3000 particles, in units of GM^2/r_s , where M is the total mass of the halo. Profiles are shown for central region, $r < r_s$, and entire halo (inset). Solid lines show analytic and semi-analytic solutions given in Appendix A.

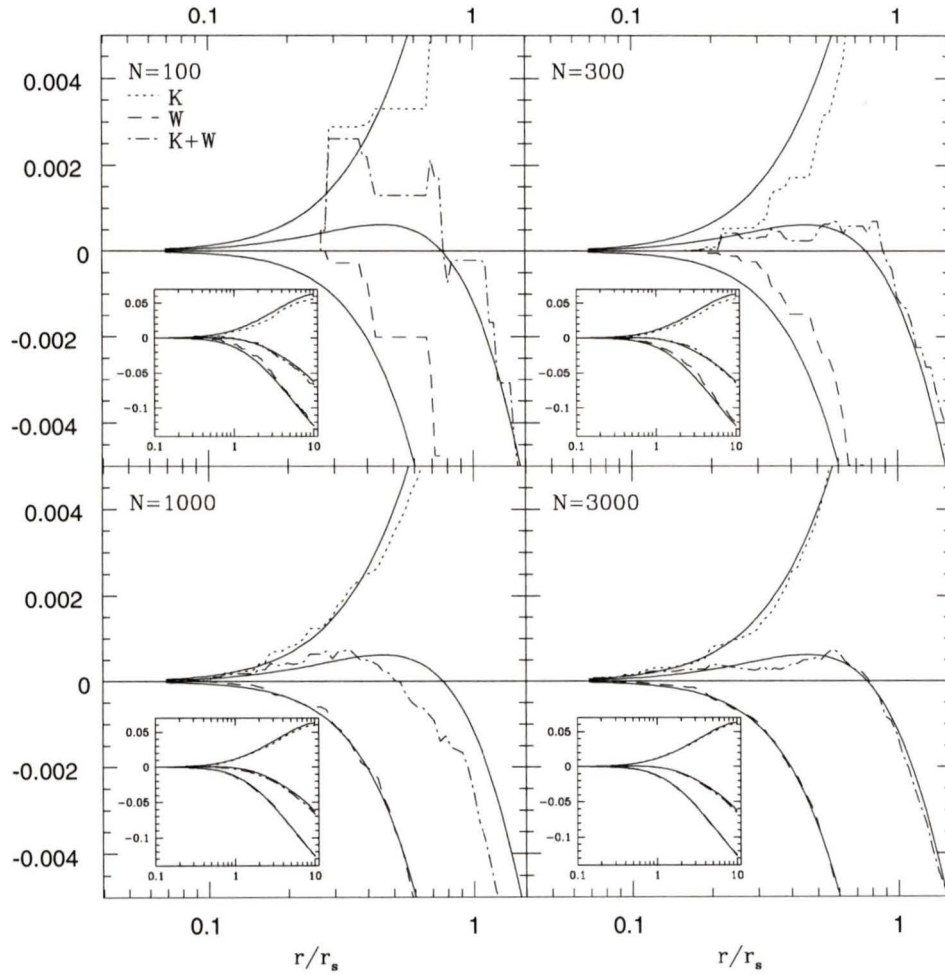


Figure 2.3: Same as Figure 2.2 for non-optimally softened unevolved halos.

		t_{relax}/t_{cross}	
N	ϵ/r_s	$\frac{0.1N}{\ln(N)}$	$\frac{0.1N}{\ln(\Lambda)}$
100	0.388	2.17	6.52
300	0.269	5.26	15.79
1000	0.180	14.48	43.45
3000	0.125	37.47	112.48
100	0.100	2.17	3.46
300	0.100	5.26	10.38
1000	0.100	14.48	34.60
3000	0.100	37.47	103.79

Table 2.1: Softening lengths and relaxation times for two sets of NFW halos. Two-body relaxation timescales for a system of point masses (third column) are shown for comparison with those of the softened particle distributions (fourth column).

the initial conditions. Halos evolved in this manner show no unusual changes in structure or energy despite the different softening schemes used in generating the initial conditions (top-hat kernel) and in the simulation code itself (spline kernel).

The time evolution of radii enclosing 10%, 20%, etc. of each halo's total mass (measured with respect to the centre of mass), as well as the total kinetic and potential energy of each halo as a function of time are shown in Figures 2.4 and 2.5 for the optimally and non-optimally softened sets of halos, respectively. As expected, noise in the mass shell radii decreases with increasing numbers of particles. However, with the exception of the 100% mass shell radius which simply tracks the position of the outermost halo particle, the radii of the mass shells after 10 crossing times are approximately equal to their initial values, except for the $\epsilon = 0.1 r_s$, $N = 100$ isolation run. In this case, the innermost mass shells appear to contract as the outer ones expand. This is the familiar phenomenon of core collapse in stellar dynamics. As particles collide, they exchange energy with one another. Particles that gain kinetic energy from interactions tend to expand the halo, while those that lose energy fall toward the centre. As a result, the $\epsilon = 0.1 r_s$, $N = 100$ halo is in a much different dynamical state compared to the other halos after being evolved in isolation for 10

parameter	code value	description
r_s	1	scale radius of satellite halo
m_{sat}	1	mass of satellite halo
G	1	gravitational constant
r_{cut}	10	cutoff radius of satellite halo
$c \equiv r_{cut}/r_s$	10	concentration of satellite halo
$r_{1/2}$	$\simeq 3.6$	half-mass radius of satellite halo
R_s	10	scale radius of host potential
$M_{host} = M(10 R_s)$	300	mass of host within 10 scale radii
$t_{cross} = \sqrt{\frac{r_{cut}^3}{Gm}}$	$\simeq 31.6$	satellite halo crossing time
$v_c(r_{1/2}) = \sqrt{\frac{Gm}{2r_{1/2}}}$	$\simeq 0.37$	satellite halo circular velocity at half-mass radius
$t_c(r_{1/2}) = \frac{2\pi r_{1/2}}{v_c(r_{1/2})}$	$\simeq 61.1$	circular orbital period at half-mass radius of satellite

orbital parameters										
r_{ap}	r_{per}	v_{ap}	v_{per}	J	E_{orb}	e	ϵ_{circ}	t_{orb}	$\frac{t_{orb}}{t_{cross}}$	$\frac{t_{df}}{t_{orb}}$
300	15	0.224	4.479	67.18	-2.28	0.905	0.261	556.6	17.6	20.0
300	30	0.376	3.762	112.86	-2.24	0.818	0.430	581.7	18.4	28.3
300	60	0.594	3.913	178.09	-2.13	0.538	0.751	639.9	20.2	35.4

Table 2.2: Numerical parameters of our simulations, where $e = (r_{ap} - r_{per}) / (r_{ap} + r_{per})$ is the generalized orbital eccentricity and $\epsilon_{circ} \equiv J / J_{circ}(E)$ is the orbital circularity, defined by the ratio between the orbital angular momentum and the angular momentum of a circular orbit with the same energy.

crossing times. The outer regions have expanded and are much less bound than they were initially, and a higher density core has developed within $\sim 1 r_s$ of the halo centre.

2.2.3 Bound Orbits

We use our evolved equilibrium halos to simulate the orbit of a satellite halo in the potential of a much larger, more massive host. In order to reduce computational expense, the host is modeled as a static, spherically symmetric NFW potential whose analytic form is given in Appendix A. Its characteristic scale radius, R_s , is chosen to be ten times that of the satellite, and its mass within $10 R_s$ is normalized to 300

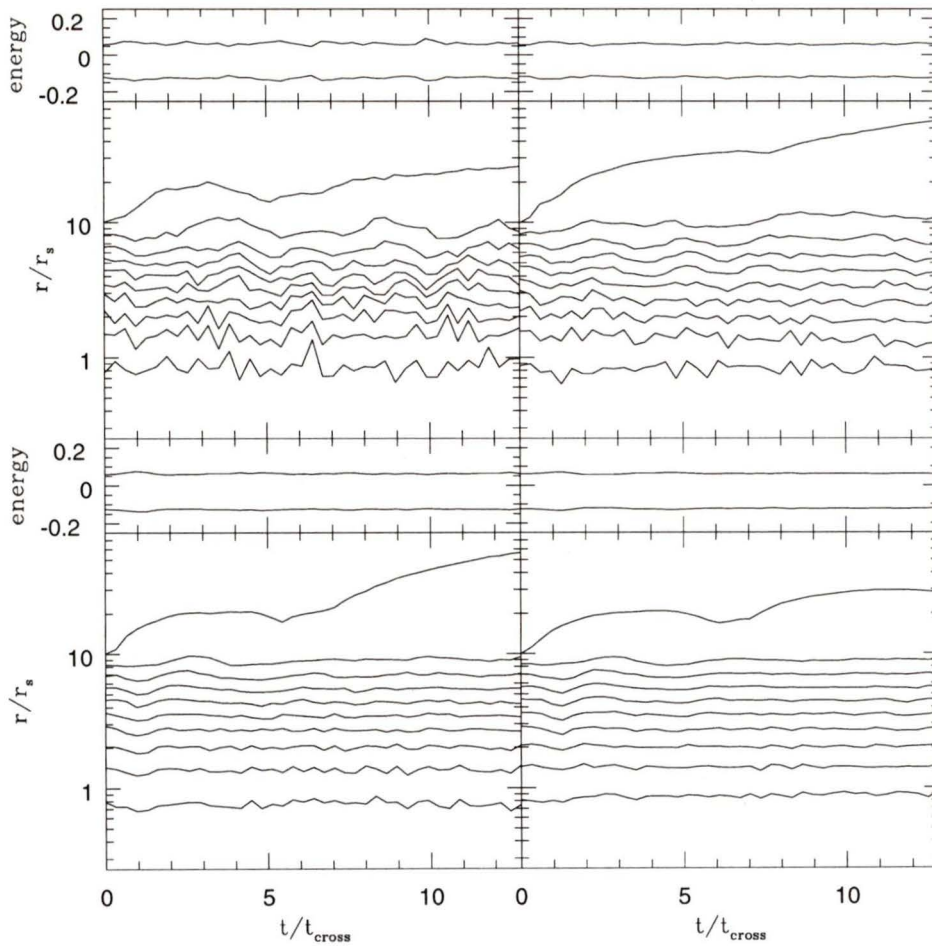


Figure 2.4: Radii containing 10%, 20%, etc. of halo particles as a function of time for optimally softened halos evolved in isolation. Top panel in each plot shows time evolution of total kinetic (positive) and total potential (negative) energy for each halo in units of GM^2/r_s , where M is the total mass of the halo.

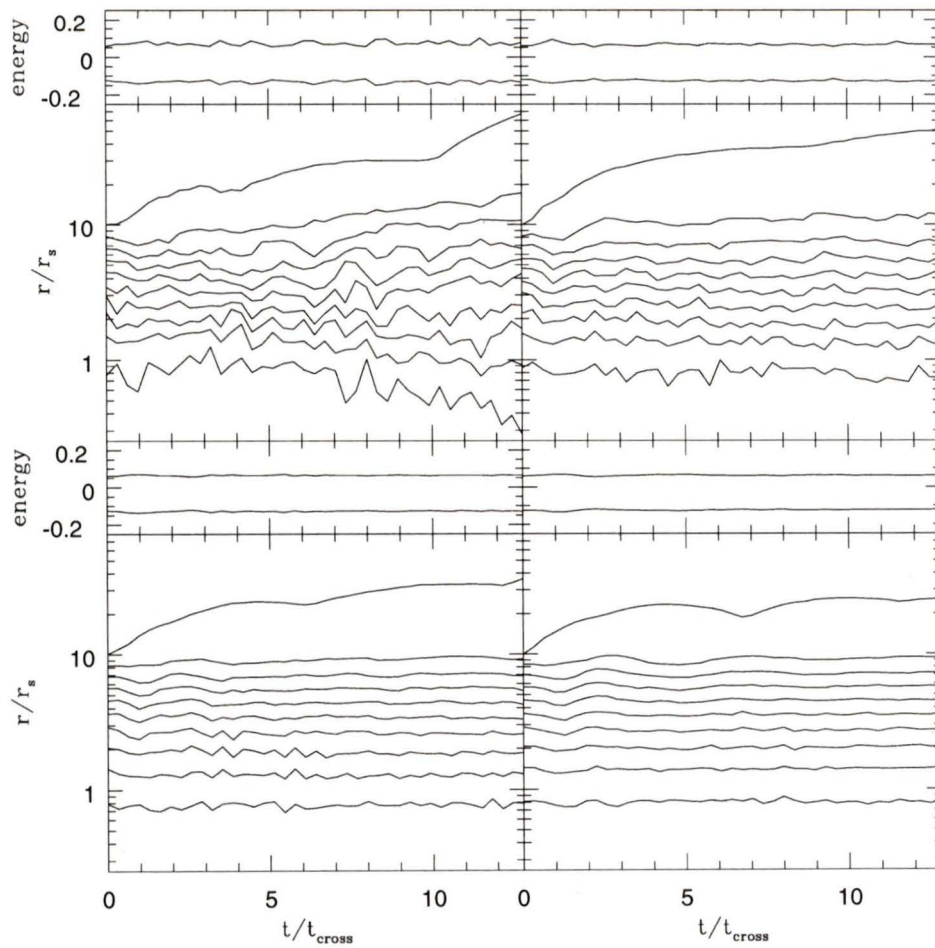


Figure 2.5: Same as Figure 2.4 for non-optimally softened halos.

times the total mass of the satellite halo. Unlike the “live” N -body satellite halo, the analytic potential has no cutoff radius, and effectively extends to infinity. The static potential is trivially softened to avoid large forces near the centre using the force law, $F_{host} = GM(R)/(R^2 + \epsilon_{host}^2)$, with $\epsilon_{host} = 0.1 R_s$. Three different elliptical orbits were simulated, all with the same apocentre, $r_{ap} = 300 r_s$, but different pericentres, $r_{per} = 15, 30,$ and $60 r_s$. Numerical parameters for these simulations are presented in Table 2.2.

Although we neglect dynamical friction by using a fixed, static potential, a simple calculation verifies that this effect is small for satellites much less massive than the host system. Lacey & Cole (1993) derive the following expression for the dynamical friction timescale

$$t_{df} \simeq \frac{\epsilon_{circ}^{0.78}}{0.855} \frac{V_c r_c^2}{G m_{sat} \ln \Lambda} \quad (2.16)$$

where r_c is the orbital radius of a satellite of mass m_{sat} in a singular isothermal halo with circular velocity V_c , $\epsilon_{circ} \equiv J/J_{circ}(E)$ is the orbital circularity of the satellite, defined by the ratio between the orbital angular momentum and the angular momentum of a circular orbit with the same energy, and the Coulomb logarithm is approximated by $\ln \Lambda = \ln(M_{host}/m_{sat})$. Setting $r_c = r_{ap}$, we find $t_{df} \gtrsim 20 t_{orb}$ for all three orbits (see Table 2.2). We therefore do not expect dynamical friction to play a significant role during the first several orbits.

Note that assigning physical units to the code units for length and mass defines physical units for all other quantities. For example, if we take $[r] \equiv r_s = 10$ kpc and $[m] \equiv m_{sat} = 10^{12} M_\odot$ the unit of time in our simulations is $[t] = \sqrt{[r]^3/G[m]} = 1.5 \times 10^7$ yr. Using this choice of parameters, our satellite halo represents a Milky Way-sized galaxy, and the host potential corresponds to that of a galaxy cluster. Due to the scale-free nature of gravity, however, an equally valid choice of units causes our satellite to represent a dwarf galaxy in the host halo of the Milky Way.

Initial velocities for the three elliptical orbits are obtained by solving the equations

of motion for this potential. The centre of an evolved halo was identified using the “moving centre” technique described by Tormen *et al.* (1997). This algorithm zeroes in on the densest region of the particle distribution by calculating the centre of mass of particles within spheres of increasingly smaller radius. The radius of the sphere is iteratively reduced by a constant factor (we use 0.95) until some fixed number of particles remains, e.g. 10% of the total. The simulation was initialized by placing the centre of a halo previously evolved in isolation for 10 crossing times at apocentre and by adding the calculated initial velocity to all particles in the halo.

Figure 2.6 shows several snapshots of the satellite particle positions during the first radial orbit of the $N = 3000$, $r_{ap} = 300 r_s$, $r_{per} = 60 r_s$ run. The effects of tidal stripping and mass loss are clearly visible in the form of elongated tidal tails, which extend for many scale radii beyond the mass of the remaining satellite. Simulation outputs were generated every 40 time units so that about 15 outputs were produced during each radial orbit.

2.3 Results

The simulations we have described feature a single N -body satellite in a bound orbit in the gravitational potential of a much larger, more massive host system. Because the host is represented by a fixed, static potential, changes in the structure of the satellite effected by the host are primarily due to differential tidal forces. Processes such as dynamical friction and particle-halo heating, which may play a significant role in the disruption of substructure in fully self-consistent N -body simulations, are not relevant here. We investigate the response of the satellite to the tidal field of the host in two ways. Firstly, we quantify mass loss using an energy criterion to identify particles which no longer remain bound to the satellite halo. Secondly, we look at changes in the satellite’s internal structure by examining its half-mass radius and density profile as a function of time.

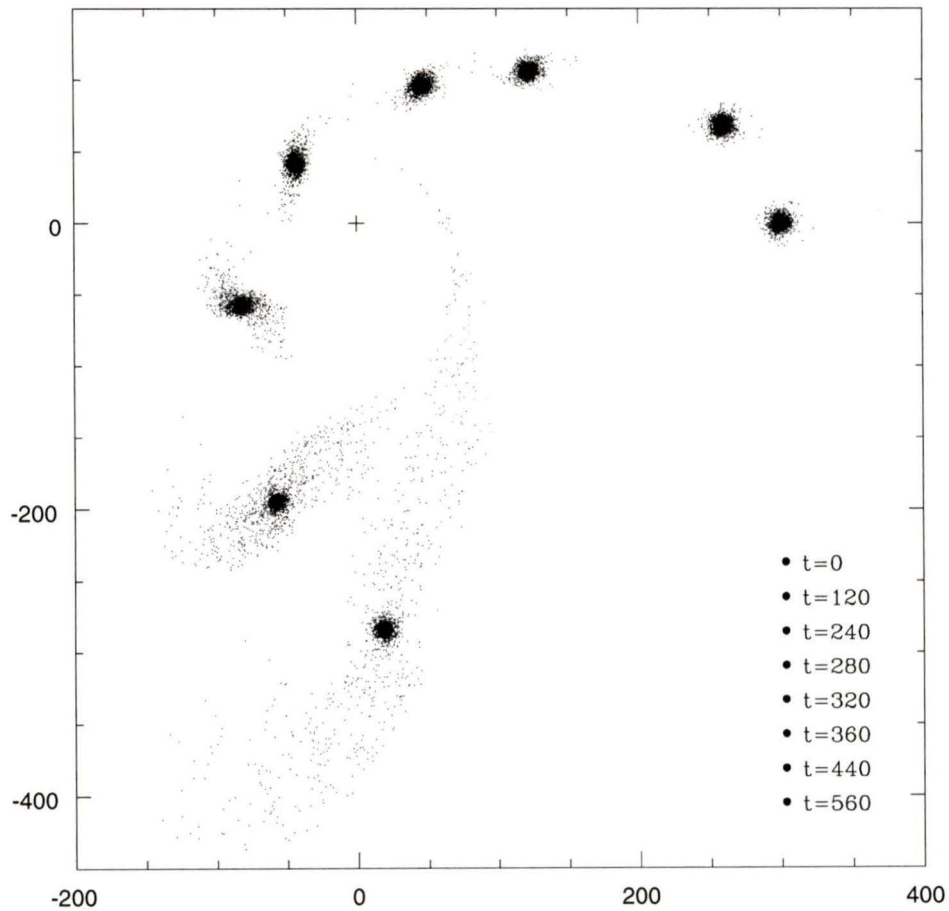


Figure 2.6: Positions of satellite halo particles projected in the orbital plane at several time outputs for the $N = 3000$, $r_{ap} = 300 r_s$, $r_{per} = 60 r_s$ run. Cross marks the centre of the static host potential. Time increases as the halo moves counter-clockwise from $t = 0$ at the initial, rightmost position to $t = 560$ in arbitrary code units at the bottommost position.

2.3.1 Mass Loss

Tidal stripping of satellite particles is readily evident in our simulations; the satellite appears increasingly elongated along the path of its orbit as it approaches pericentre, and during each pericentric passage a substantial fraction of particles are physically separated from the satellite by the tidal field of the host (see Figure 2.6). One way of quantifying this mass loss due to tidal stripping is by identifying the satellite particles which remain gravitationally self-bound. We use the following unbinding algorithm, previously described by Tormen *et al.* (1998), to define the satellite's self-bound mass:

- identify the centre of mass and average velocity of particles in the densest region of the halo as determined by the moving centre technique
- calculate the kinetic energy of particles in this reference frame, and the potential energy due the other particles in the halo
- remove all particles with positive total (kinetic plus potential) energy from consideration and calculate the centre of mass and average velocity of the remaining particles
- recalculate the kinetic and potential energy of each particle in the new reference frame
- repeat the previous two steps until the number of particles with negative total energy remains constant; these particles constitute the self-bound mass of the system
- repeat the process for the next simulation time output, using only the self-bound particles to identify the halo centre with the moving centre technique

The self-bound mass of each satellite as a function of time is shown in Figure 2.7. In general, the self-bound mass curves have a step-like appearance, with most of the

mass loss occurring at orbital pericentre, i.e. $t/t_{orb} = 0.5, 1.5, 2.5$, etc. where t_{orb} is the radial period. In addition, the logarithmic “size” of these steps appears to be fairly constant, especially for the higher resolution simulations. That is, a given satellite halo loses roughly the same percentage of its remaining self-bound mass after each pericentric passage.

As expected, satellites which pass closer to the centre of the host potential lose more mass during each pericentric passage than do halos with larger pericentric radii. Satellites on these more radial orbits experience stronger tidal forces at pericentre, but also pass through pericentre at higher velocities compared to halos on more circular orbits. The result is a large, abrupt drop in the self-bound mass of halos on elliptical orbits with $r_{per} = 15 r_s$, and a smaller, more gradual decrease for $r_{per} = 60 r_s$ orbits.

Upon inspection of Figure 2.7 several trends are apparent:

1. Non-optimally softened halos with $N = 100$ and $N = 300$ particles are disrupted much faster than other halos. The mass loss curves of these halos also appear much more erratic compared to the smooth, regularly spaced steps of the $N = 1000$ and $N = 3000$ halos.
2. The mass loss curves of halos on orbits with $r_{per} = 30 r_s$ and $r_{per} = 60 r_s$ appear to converge nicely with increasing mass resolution. For the $r_{per} = 60 r_s$ orbit in particular, increasing the number of particles from $N = 100$ to $N = 1000$ reduces the amount of mass lost by the satellite during each orbit, and virtually identical results are obtained for the $N = 1000$ and $N = 3000$ halos.
3. Optimally softened halos with $N = 100, 300$, and 1000 particles eventually start to lose *less* mass than the higher resolution $N = 3000$ halo in the case of the $r_{per} = 15 r_s$ orbit. In fact, the two lowest resolution halos virtually stop losing mass when $\sim 10\%$ of their original mass remains.

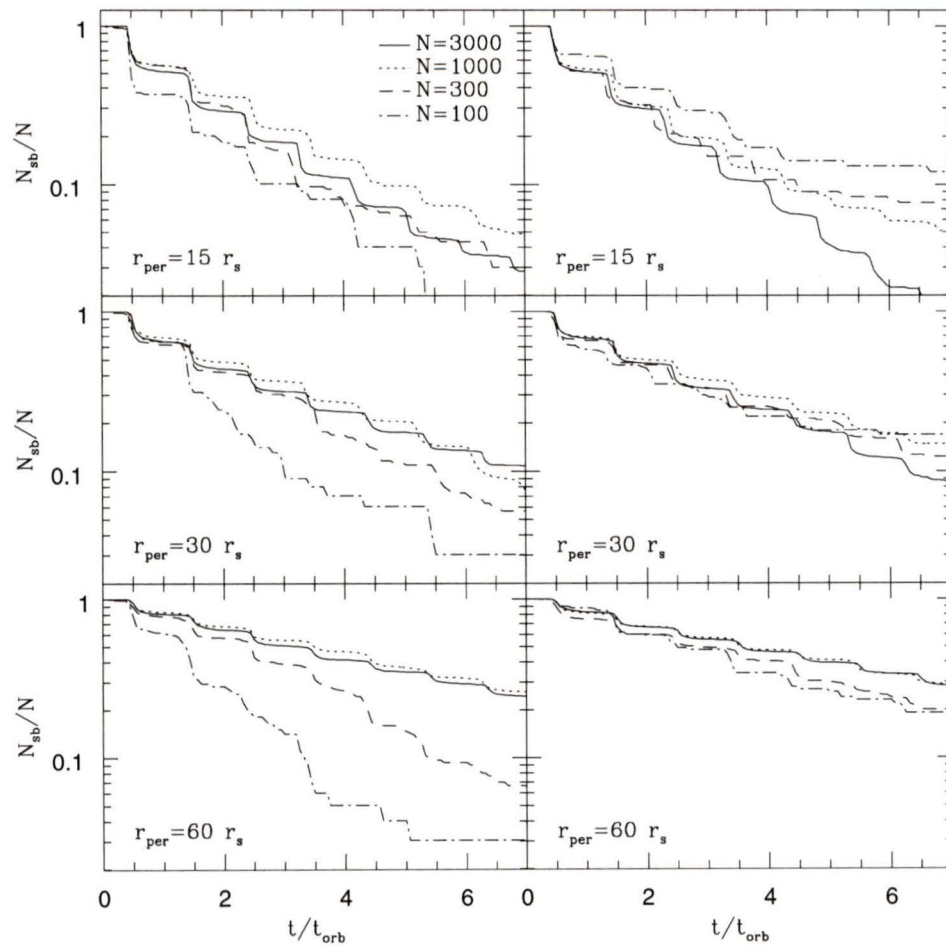


Figure 2.7: Time evolution of self-bound mass of satellite halo for three different elliptical orbits with apocentric radius, $r_{ap} = 300 r_s$, and pericentric radius, r_{per} , as shown. Left and right side correspond to simulations performed with non-optimally and optimally softening halos, respectively (see Table 2.2 for softening lengths).

How can we understand these results? Conventional wisdom suggests that at fixed mass resolution, halos simulated with large softening values are less bound and therefore more easily disrupted than those with smaller softenings. Nevertheless, the non-optimally softened 100 and 300 particle halos (both $\epsilon = 0.1 r_s$) are without exception disrupted faster than their optimally softened counterparts ($\epsilon = 0.388 r_s$ and $0.269 r_s$, respectively).

The key to this apparent contradiction is that each halo was evolved in isolation for several crossing times before being inserted into orbit in the cluster potential. As previously noted, the non-optimally softened 100 particle halo appeared to relax significantly over the course of 10 crossing times. As a result, the outer layers of this halo have expanded and are more easily stripped by tidal forces when it is placed in the host potential. The dense core which remains continues to evaporate at an accelerated rate since $t_{relax} \propto N$ and the number of bound particles decreases as the halo loses mass. This effect is even more noticeable for the $r_{per} = 60 r_s$ orbit because the orbital period is longer and the halo has more time to relax during each orbit (see Table 2.2).

Relaxation effects are less significant for the optimally softened halos since their relaxation timescales are longer than those of the non-optimally softened halos (see Table 2.1). In the $r_{per} = 60 r_s$ orbit mass is stripped gradually from the outer regions of the halo and each halo loses approximately the same fraction of its remaining mass during each pericentric passage. In the $r_{per} = 15 r_s$ orbit, halos are stripped much more violently, losing $\sim 50\%$ of their mass in each orbit. Once the halo is reduced to a dense core of about 10 tightly bound particles mass loss effectively ceases.

2.3.2 Internal Structure

The internal structure of our halos was originally characterized by the NFW density profile. How does this change as the satellite is tidally stripped? Figure 2.8

shows the time evolution of the radius containing half the remaining self-bound mass, hereafter referred to as the half-mass radius ($r_{1/2}$). In all cases, $r_{1/2}$ decreases (though not monotonically) as a function of time. The non-optimally softened $N = 100$ halo, for example, is quickly reduced to a small number of bound particles and its half-mass radius fluctuates greatly from time to time, but on average continues to decrease with time. This indicates that mass is lost preferentially from the outer regions of the halo, since losing mass from the central regions would tend to increase the half-mass radius.

The half-mass radius is somewhat more sensitive to numerical effects than the self-bound mass, and appears to converge more slowly to the results of the optimally softened $N = 3000$ simulation. Even when satellites with different mass resolution experience the same mass loss (e.g. the $r_{per} = 60 r_s$, $N = 1000$ and $N = 3000$ runs), the half-mass radius is significantly smaller for halos with fewer particles indicating the formation of denser cores due to shorter relaxation timescales. The time evolution of the mean density within the half-mass radius, $N_{sb}/N/r_{1/2}^3$, is shown in Figure 2.9. After several orbits, the mean density is significantly higher in the $N = 100$ and $N = 300$ halos compared to the 1000 and 3000 particle halos. This suggests that the relaxation timescale of these halos is sufficient to suppress artificial relaxation due to numerical effects. In Figure 2.10, we plot the ratio of the self-bound mass to the half-mass radius, $N_{sb}/N/r_{1/2}$, i.e. the square of the circular velocity at the half-mass radius, $v_c^2(r_{1/2})$. In the high resolution $N = 1000$ and $N = 3000$ halos, this quantity tends to decrease at a relatively constant rate as the satellite orbits in the host potential. In fact, our results indicate that the half-mass circular velocity of the $N = 3000$ halos changes by as much as 40% to 50% per orbit. This suggests that low circular velocities might serve as a signature of tidal mass loss in cluster galaxies. The circular velocity profiles of satellite halos at apocentre are shown in Figures 2.11, 2.12, and 2.13 for orbits with $r_{per} = 15, 30$, and $60 r_s$, respectively. The peak circular velocity changes by $\sim 15\%$ per orbit in the most extreme case, the $r_{per} = 15 r_s$ orbit. In all cases the circular velocity profile has declined significantly after the first few

orbits.

The time evolution of the density profiles of the self-bound mass of the $N = 3000$ satellite halos are shown in Figures 2.14, 2.15, and 2.16 for orbits with $r_{per} = 15, 30,$ and $60 r_s$, respectively. We examine the density profile of the satellite halo each time it reaches apocentre and fit the density with an NFW profile using the Levenberg-Marquardt method of minimizing χ^2 (Press *et al.*, 1992). We exclude the first bin from the fit since this region is smaller than the softening length, and is artificially underdense due to numerical effects. We also restrict the fit to bins within the radius containing only 70% of the self-bound mass. Beyond this radius, the density falls off steeply and an NFW profile is unable to simultaneously fit the inner and outer regions of the halo.

The density in the outer regions decreases steadily with time as mass is tidally stripped from satellite. The central density also decreases significantly, as tidal heating depletes the innermost region of particles causing the formation of flat core of relatively constant density. The concentration value, $c_{70\%}$ cited for each profile in Figures 2.14 to 2.16 is simply the ratio of the 70% bound mass radius to the scale radius of the fitted profile. Although these values tend to decrease as a function of time, their actual significance is questionable because we assume at all times that the outermost radius of the halo is the 70% mass radius. The NFW profile provides a reasonable fit to this restricted range of the self-bound halo although we find $\chi_{red}^2 > 1$ for all fits. After several orbits it becomes difficult to fit an NFW profile to the halo density since the inner region becomes more shallow than r^{-1} and the outer region becomes steeper than r^{-3} .

2.4 Modeling Mass Loss

The simulations we have presented clearly demonstrate that satellites undergo significant mass loss in the tidal field of a massive host. The regular and consistent

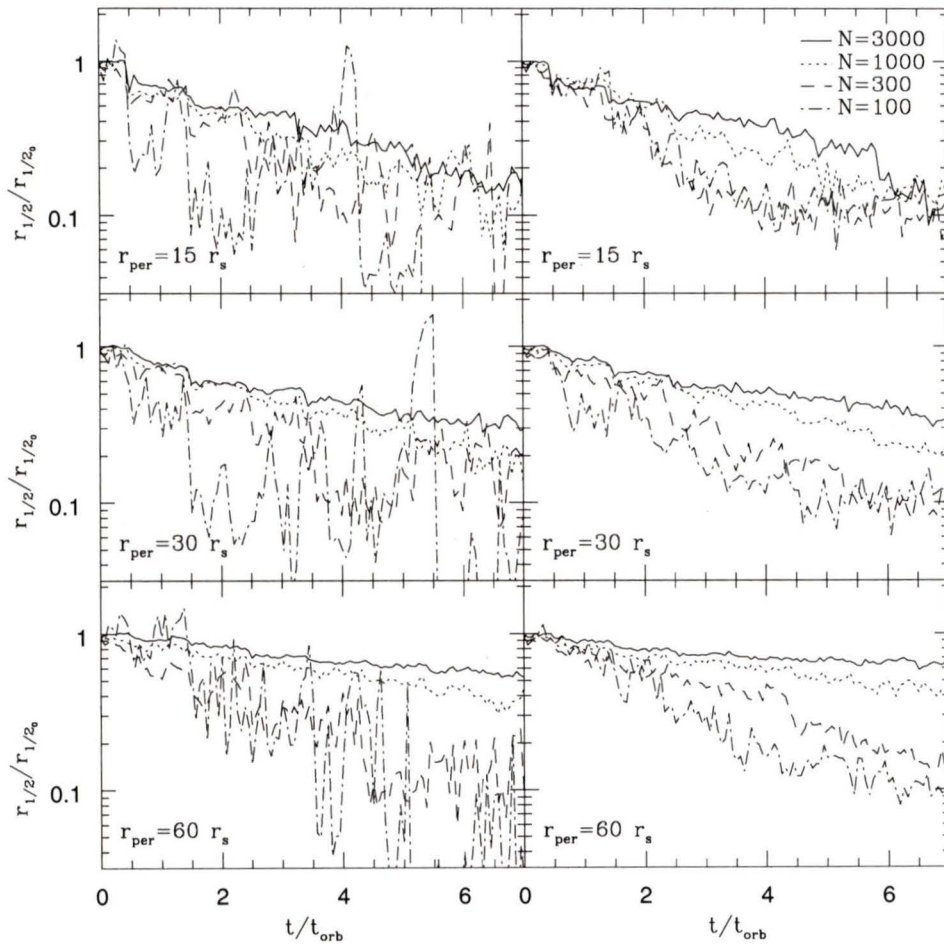


Figure 2.8: Radius containing half the remaining self-bound mass, $r_{1/2}$, scaled to the initial half-mass radius, $r_{1/2_0}$, as a function of time in radial periods for elliptical orbits with apocentric radius, $r_{ap} = 300 r_s$, and pericentric radius, r_{per} , as shown. Left and right side correspond to simulations performed with non-optimally and optimally softened halos, respectively.

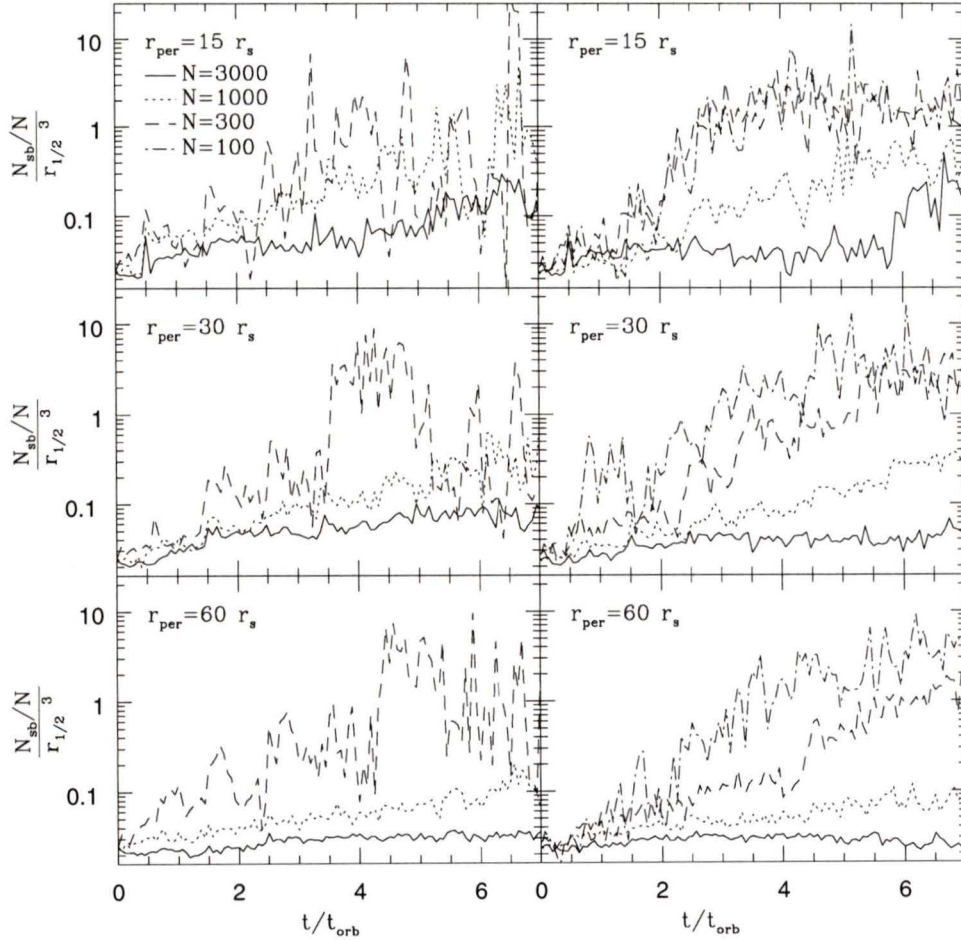


Figure 2.9: Mean density within radius containing half the remaining self-bound mass, $N_{sb}/N/r_{1/2}^3$, as a function of time in radial periods for elliptical orbits with apocentric radius, $r_{ap} = 300 r_s$, and pericentric radius, r_{per} , as shown. Left and right side correspond to simulations performed with non-optimally and optimally softened halos, respectively. Non-optimally softened $N = 100$ halo not shown because it is noise dominated.

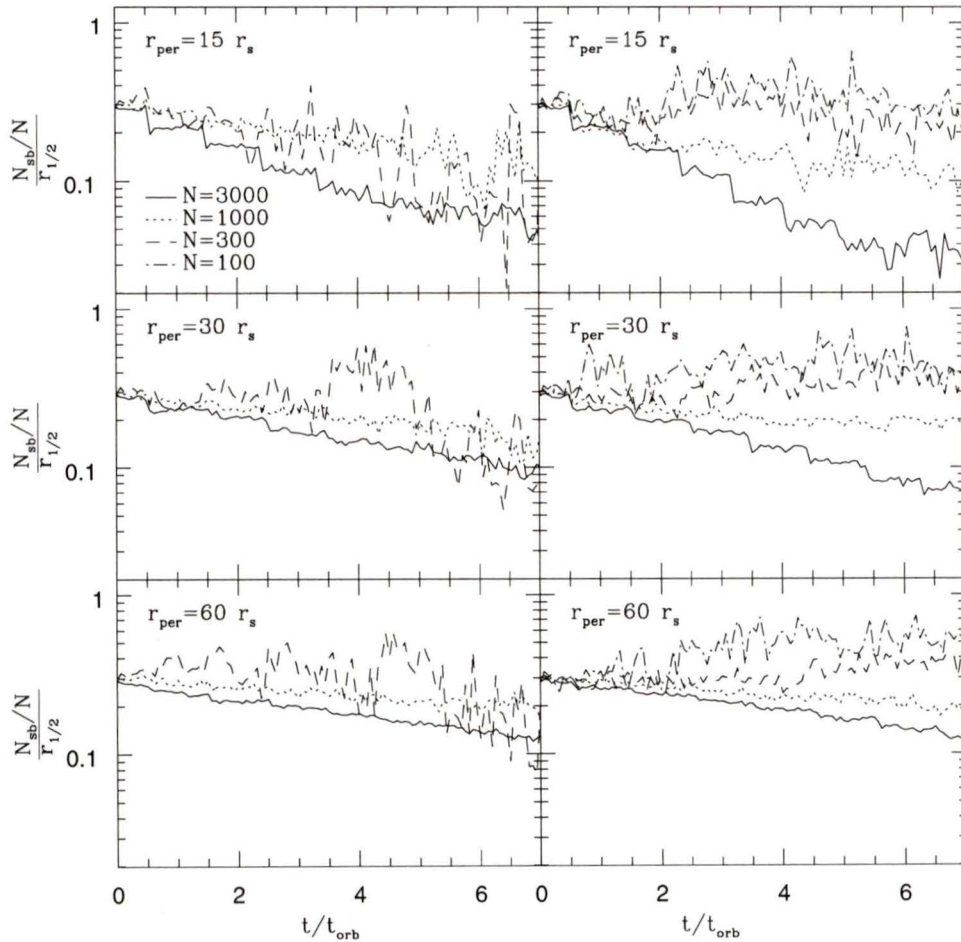


Figure 2.10: Circular velocity squared at the half-mass radius of the satellite halo, $v_c(r_{1/2})^2$, as a function of time in radial periods for elliptical orbits with apocentric radius, $r_{ap} = 300 r_s$, and pericentric radius, r_{per} , as shown. Left and right side correspond to simulations performed with non-optimally and optimally softened halos, respectively. Non-optimally softened $N = 100$ halo not shown because it is noise dominated.

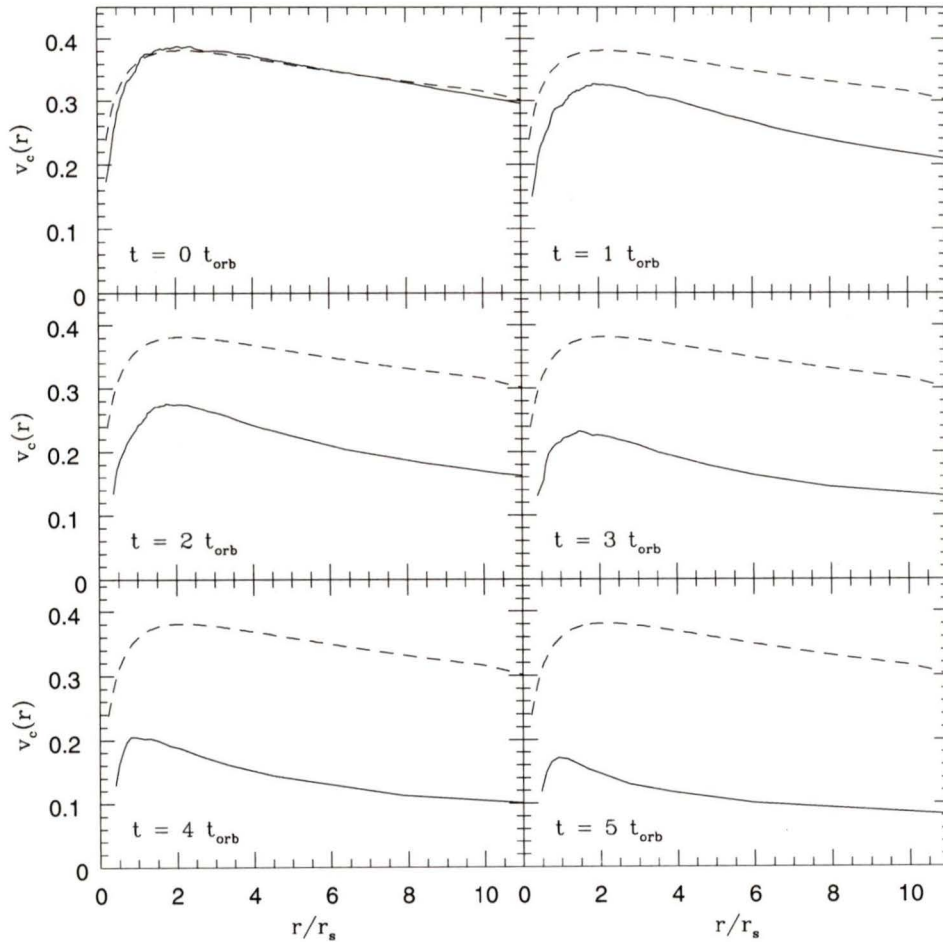


Figure 2.11: Circular velocity profiles of optimally softened $N = 3000$ satellite halos at consecutive apocentric passages for the $r_{ap} = 300 r_s$, $r_{per} = 15 r_s$ orbit in units of $\sqrt{Gm_{sat}/r_s}$. Particles are binned as in Figure 2.1, taking the centre of mass determined by the moving centre method as the halo centre. Dashed line shows analytic NFW circular velocity profile corresponding to initial halo for comparison.

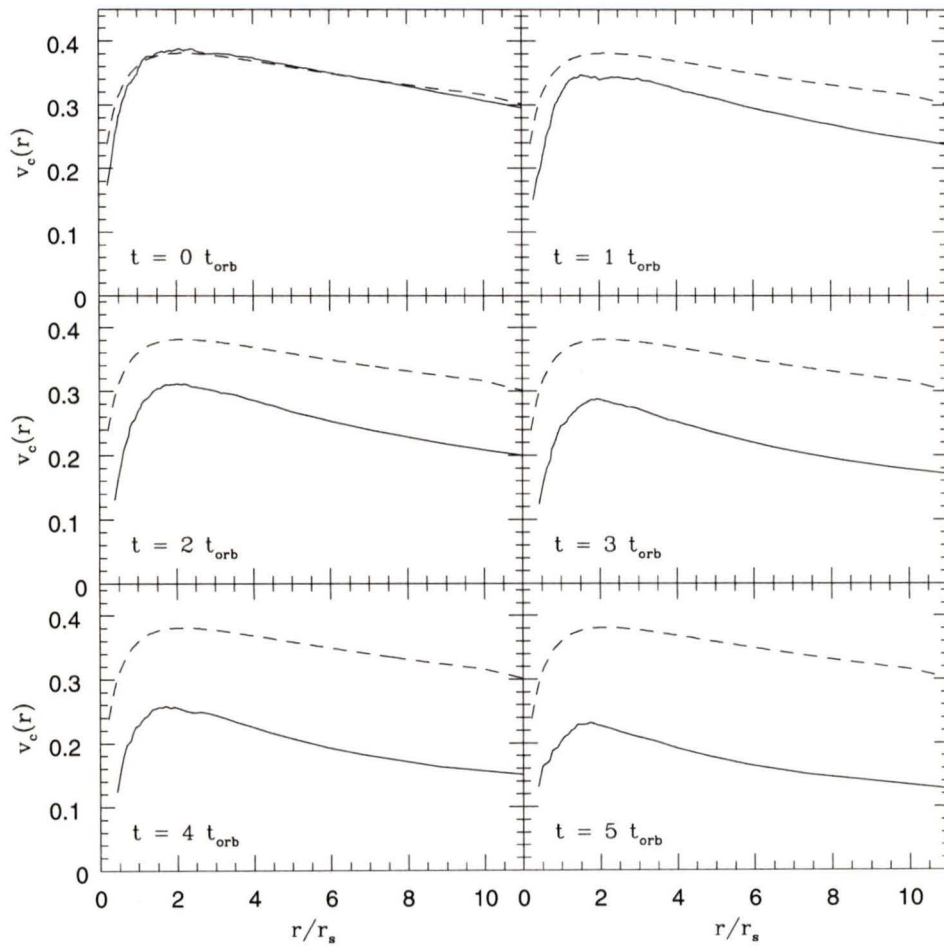


Figure 2.12: Same as Figure 2.11 for the $r_{\text{ap}} = 300 r_s$, $r_{\text{per}} = 30 r_s$ orbit.

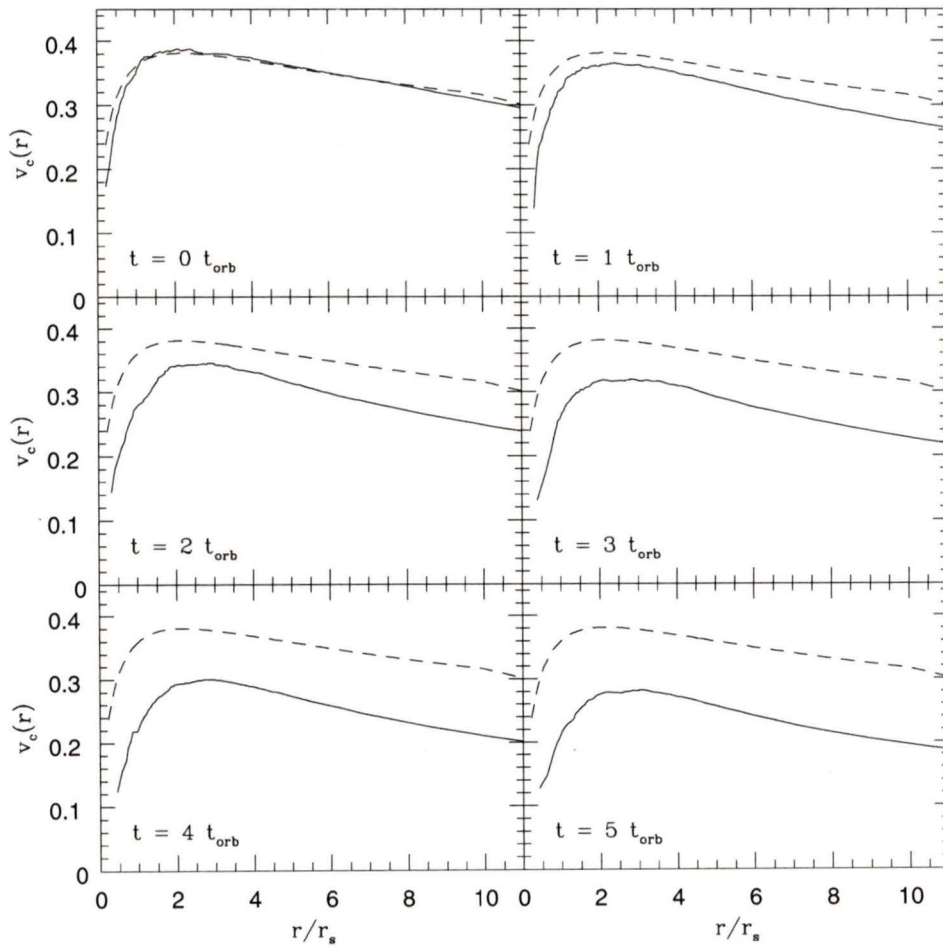


Figure 2.13: Same as Figure 2.11 for the $r_{\text{ap}} = 300 r_s$, $r_{\text{per}} = 60 r_s$ orbit.

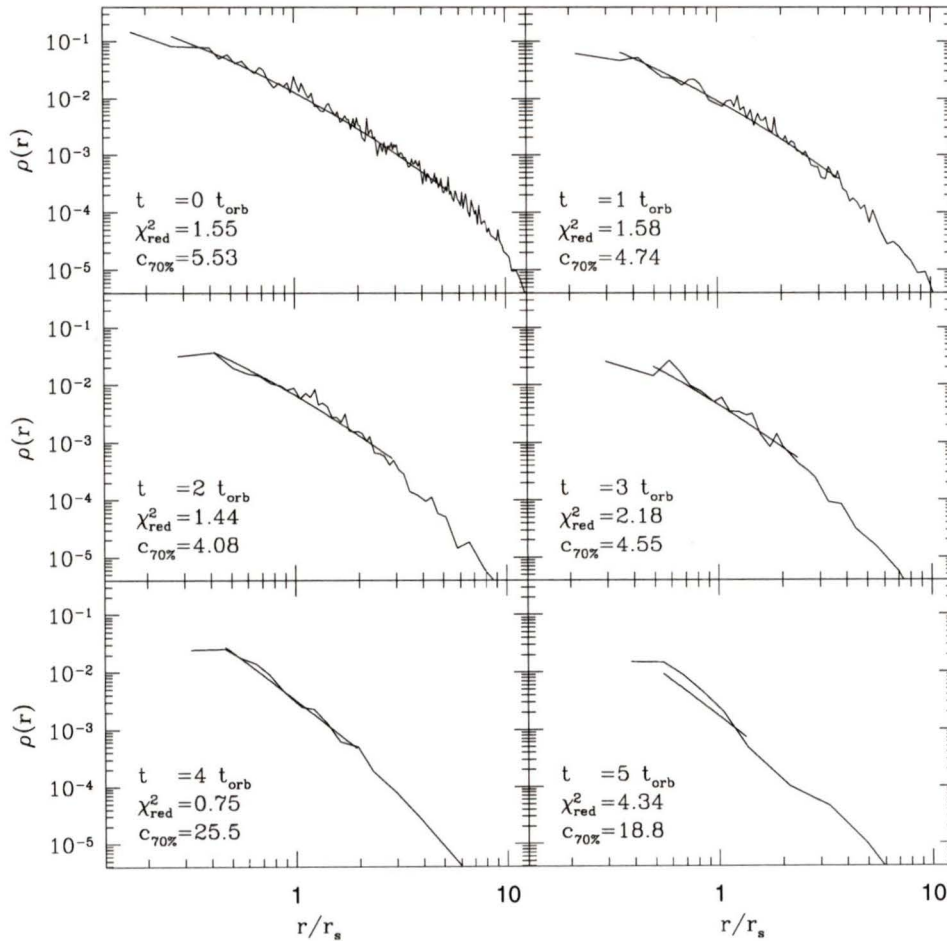


Figure 2.14: Density profiles of optimally softened $N = 3000$ satellite halos at consecutive apocentric passages for the $r_{ap} = 300 r_s$, $r_{per} = 15 r_s$ orbit. Density profiles and χ_{red}^2 are calculated as in Figure 2.1, taking the centre of mass determined by the moving centre method as the halo centre. NFW fits to the halo profile with the radius containing 70% of the remaining self-bound mass are shown as smooth solid lines. The concentration value shown, $c_{70\%}$, is the 70% bound mass radius divided by the scale radius of the fitted profile.

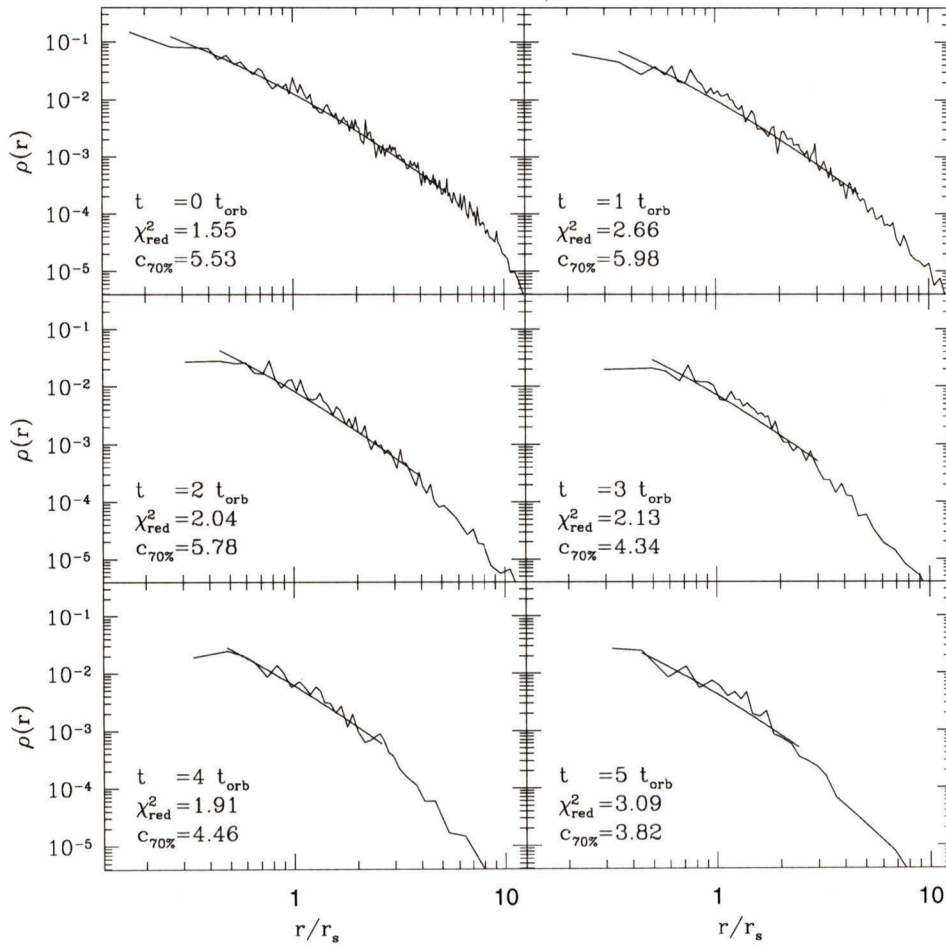


Figure 2.15: Same as Figure 2.14 for the $r_{\text{ap}} = 300 r_s$, $r_{\text{per}} = 30 r_s$ orbit.

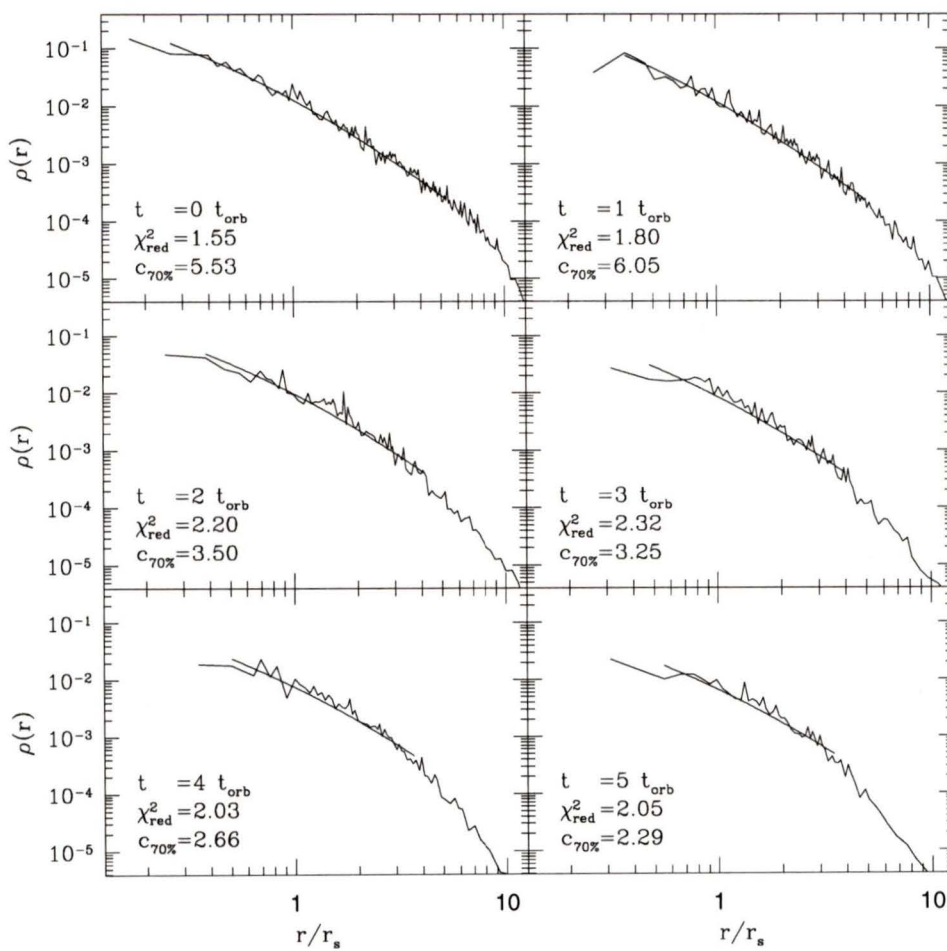


Figure 2.16: Same as Figure 2.14 for the $r_{\text{ap}} = 300 r_s$, $r_{\text{per}} = 60 r_s$ orbit.

pattern of mass loss we observe suggests that the mass loss is well-behaved. In this section we attempt to model the mass loss experienced by satellite halos using approximations based on simple dynamical arguments. Our ultimate goal is to develop a general prescription for predicting the mass loss and disruption timescale of a satellite galaxy in a galaxy cluster.

2.4.1 Tidal Approximation

As a first attempt, we use the tidal approximation to predict the mass lost by a satellite halo during a single orbit. Here, the tidal radius, r_t , is the distance from the centre of the satellite beyond which the differential tidal forces of the host potential exceed the self-gravity of the satellite. One predicts the mass external to this radius to be tidally stripped.

The precise definition of the tidal radius depends on the assumptions made in its derivation. If we assume that the gravitational potentials of both the satellite and the host are given by point masses, and that the satellite is small compared to its distance from the centre of the host, we find the Roche limit:

$$r_t = \left(\frac{m}{2M} \right)^{1/3} R \quad (2.17)$$

where m is the mass of the satellite, M is the mass of the host, and R is their relative distance. We obtain a more general expression by taking the extended mass profiles of both systems into account, and solving for r_t numerically in the following equation (Tormen, Diaferio & Syer, 1998; Klypin, Gottlöber & Kravtsov, 1999):

$$\frac{m(r_t)}{r_t^3} = \left(2 - \frac{R}{M(R)} \frac{\partial M}{\partial R} \right) \frac{M(R)}{R^3} \quad (2.18)$$

Note that the mean density of the satellite within r_t is of the order of the mean density of the host within R . A mean satellite density of twice that of the host

gives the Roche limit, whereas equation (2.18) corresponds to a smaller overdensity. Figure 2.17 shows the tidal radius, satellite mass within the tidal radius, and mean overdensity of the satellite relative to the host as a function of orbital radius for our satellite-host system. The tidal radius increases from $r_t \simeq 1 r_s$ to $r_t \simeq 10 r_s$ between an orbital radius of $10 r_s$ and $100 r_s$. The pericentric radii of our three orbits lie within this range so we expect the tidal radius approximation to predict nonzero mass loss.

We use the following procedure to estimate the mass lost during each orbit:

- identify the simulation output in which the satellite is closest to apocentre according to the position of the centre of the satellite determined via the moving centre technique
- count the number of self-bound particles within some radius r that is much larger than the tidal radius at orbital pericentre
- if $m(r)/r^3$ is less than the right-hand side of equation (2.18) evaluated at $R = r_{per}$, reduce r by dr
- repeat the previous two steps until $m(r)/r^3$ is greater than or equal to the right-hand side, and thus $r = r_t$, or until $r = 0$, in which case no solution exists
- the self-bound mass external to r_t , $m_{sb}(r > r_t)$, is predicted to be tidally stripped in the ensuing pericentric passage

We compare the predictions of the tidal approximation with the actual mass lost by the satellite in Figure 2.18. Here the actual fraction of self-bound mass lost $\Delta N_{sb}/N_{sb}$ during each of the first six orbits is plotted against the corresponding prediction of the tidal approximation for the optimally softened set of halos. The correlation between the two appears to be fairly strong, especially for the $N = 1000$ and $N = 3000$ halos. Overall, the predictions seem most accurate for the $r_{per} = 30 r_s$

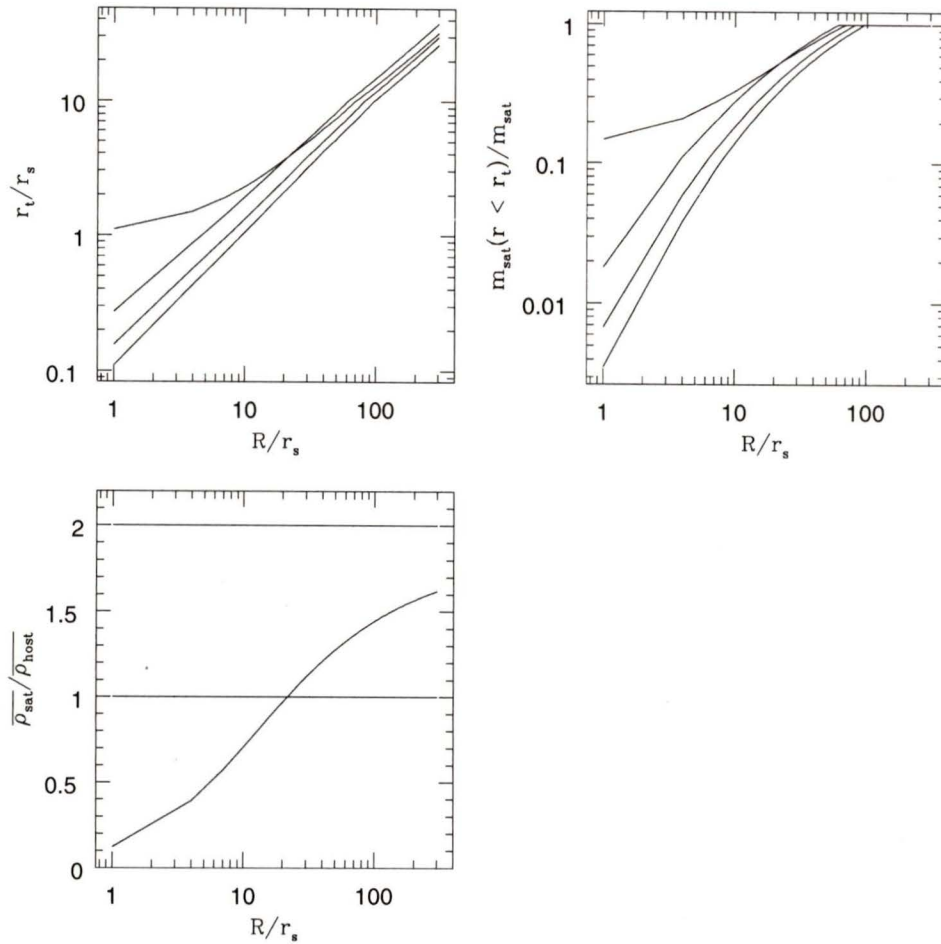


Figure 2.17: Top left: tidal radius as a function of orbital radius R in units of the satellite scale radius, r_s , for our satellite-host system. Three parallel curves show the tidal radius corresponding to $\overline{\rho_{\text{sat}}}/\overline{\rho_{\text{host}}} = 1, 2,$ and 3 (upper, middle, and lower curves, respectively), where $\overline{\rho_{\text{sat}}}/\overline{\rho_{\text{host}}}$ is the mean overdensity of the satellite within tidal radius relative to the mean density of the host within the orbital radius. Fourth curve shows tidal radius corresponding to equation (2.18). Top right: mass within tidal radius for the same four definitions of the tidal radius. Bottom left: $\overline{\rho_{\text{sat}}}/\overline{\rho_{\text{host}}}$ as a function of orbital radius.

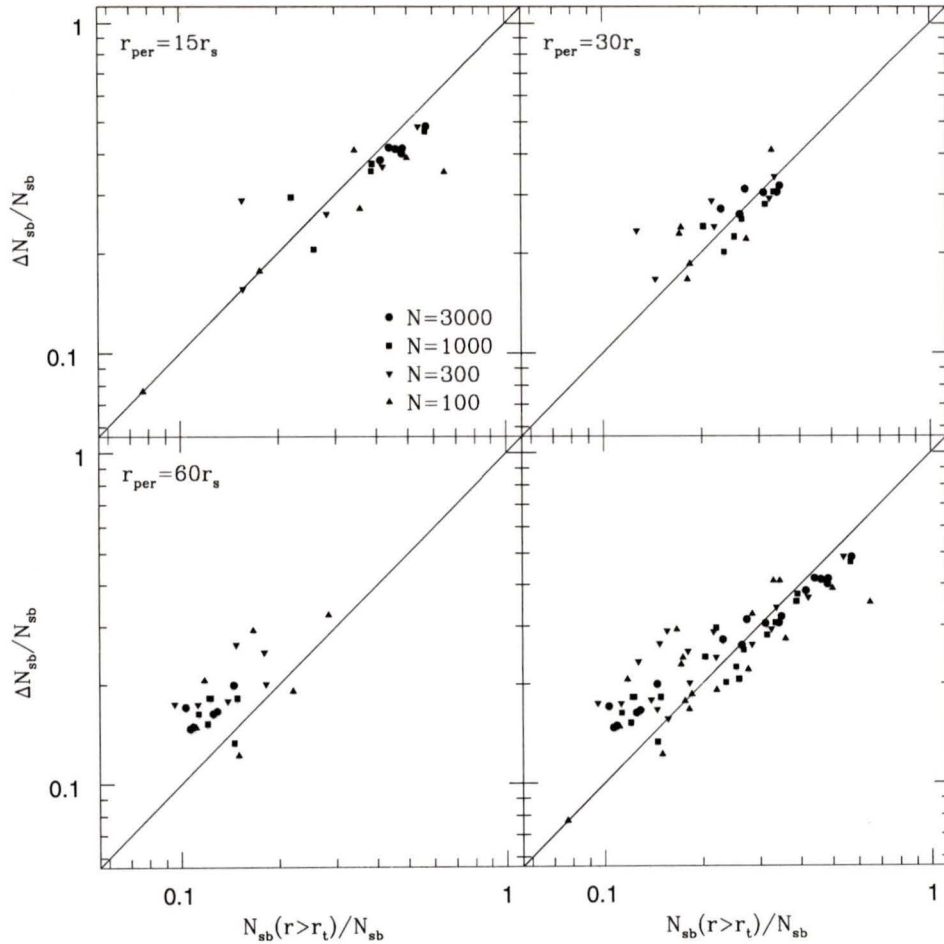


Figure 2.18: Change in self-bound mass between consecutive apocentric passages versus mass loss predicted by tidal approximation for optimally softened halos on elliptical orbits with $r_{per}/r_s = 15, 30, 60$ and total sample (lower right panel).

orbit, with a slight tendency to over-predict mass loss in the $r_{per} = 15 r_s$ orbit, and a more pronounced tendency to under-predict mass loss in the $r_{per} = 60 r_s$ orbit.

The tidal approximation is somewhat less effective in predicting mass loss in the non-optimally softened set of simulations. Figure 2.19 shows that this method is unable to account for the accelerated disruption experienced by the 100 and 300 particle halos. Two-body relaxation causes these halos to expand significantly between apocentric and pericentric passage, such that the halo at pericentre is much less bound than at the time of the mass loss prediction. Particles are therefore more susceptible to tidal stripping than the tidal approximation originally predicted.

2.4.2 Impulse Approximation

We attempt to improve our mass loss predictions by using a semi-analytic formulation of the impulse approximation. In general, the impulse approximation is valid for high-speed encounters in which the motions of particles within each system can be neglected, i.e. the relative speed of the two systems is large compared to their internal velocity dispersions. The following procedure, based on the prescription of Aguilar & White (1985), is used to apply the impulse approximation:

- calculate the orbital path of the satellite by solving the equations of motion using a Runge-Kutta integration scheme for 1000 steps equally spaced in time, per radial period
- identify the satellite at apocentre as in the tidal approximation and calculate the total change in velocity, $\Delta \mathbf{v}$, over one orbit for each self-bound particle in the satellite by summing the instantaneous acceleration due to the host potential at each step along the orbital path:

$$\Delta \mathbf{v} = \sum_{i=1}^{1000} \mathbf{a}(t_i) \Delta t \quad (2.19)$$

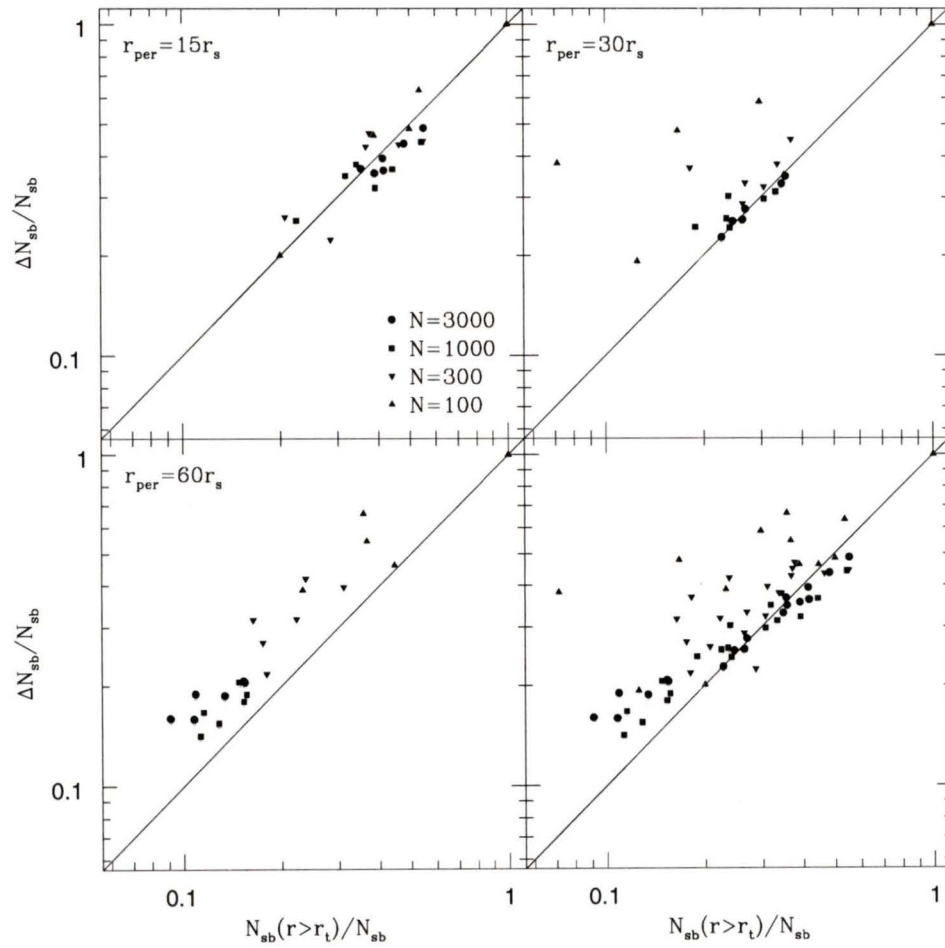


Figure 2.19: Same as Figure 2.18 for non-optimally softened halos.

- add this change in velocity to the initial velocity \mathbf{v}_0 and subtract the average velocity, \mathbf{v}_{avg} , to find the new velocity, \mathbf{v}_{imp} , for each particle

$$\mathbf{v}' = \mathbf{v}_0 + \Delta\mathbf{v} \quad (2.20)$$

$$\mathbf{v}_{avg} = \frac{\sum_{i=1}^N \mathbf{v}'}{N} \quad (2.21)$$

$$\mathbf{v}_{imp} = \mathbf{v}' - \mathbf{v}_{avg} \quad (2.22)$$

- apply the previously described unbinding algorithm to the (unchanged) particle positions and new particle velocities to identify unbound particles after that orbit. Note that this is equivalent to finding particles whose velocity is greater than the escape velocity with respect to the rest, $N(v_{imp} > v_{esc})$, since $v_{esc} = \sqrt{2\Phi(r)}$ and we have defined the self-bound particles as having $K = mv_{imp}^2/2 > m\Phi(r) = W$

Unlike the tidal approximation, this method incorporates both spatial and kinematic information about the halo particles and is more computationally expensive since the change in velocity is the sum of terms calculated at many timesteps and the unbinding algorithm requires multiple iterations for convergence in the number of self-bound particles. The predictions of the impulse approximation are compared with the actual change in self-bound mass in Figure 2.20. The predictions for the $r_{per} = 15 r_s$ orbit are again better than those for orbits with larger pericentric radii. This is expected, since the more circular orbits have longer orbital periods, and the motions of the particles become significant. Overall, the predictions of the impulse approximation seem slightly more accurate than those of the tidal approximation, and show marginally less scatter than those of the tidal approximation. Table 2.3 shows the error in the predictions of the tidal and impulse approximations for the optimally softened $N = 3000$ halos. The maximum error in the predictions of the impulse approximation is constant among the three different orbits whereas the max-

imum error in the tidal approximation is much greater for the $r_{per} = 60 r_s$ orbit. The tidal approximation under-predicts mass loss by as much as 40% for this orbit, while the maximum error in the impulse approximation predictions is less than 18% in all three orbits. Overall, the average error in the predictions of the impulse approximation is less than that of the tidal approximation predictions. The standard deviation of percent errors is also smaller for the impulse approximation predictions in two of the three orbits.

	% error (tidal)			
r_{per}	min	max	avg	σ
15	+5.6	+20.2	+13.3	5.8
30	-15.0	+12.5	-0.3	11.2
60	-40.0	-22.4	-27.8	6.1
	% error (impulse)			
r_{per}	min	max	avg	σ
15	+4.9	+17.8	+9.7	4.9
30	-17.8	+9.8	-5.0	10.1
60	-17.9	-5.7	-12.1	4.1

Table 2.3: Error statistics for single orbit predictions of tidal and impulse approximation over the first six orbits of the optimally softened $N = 3000$ satellite halo. Includes minimum, maximum, average, and standard deviation of percent error in single orbit predictions of $\Delta N_{sb}/N_{sb}$.

In summary, the tidal and impulse approximations predict mass loss on an orbit-by-orbit basis to within an average accuracy of 15% and 10%, respectively. The predictions of the impulse approximation are slightly more accurate and more consistent compared to those of the tidal approximation, especially for the least radial, $r_{per} = 60 r_s$ orbit, but at the cost of a more computationally expensive algorithm.

2.4.3 Modeling Cumulative Mass Loss

Thus far, we have only considered predictions of mass loss over a single radial orbit. We now apply our methods over several consecutive orbits and attempt to

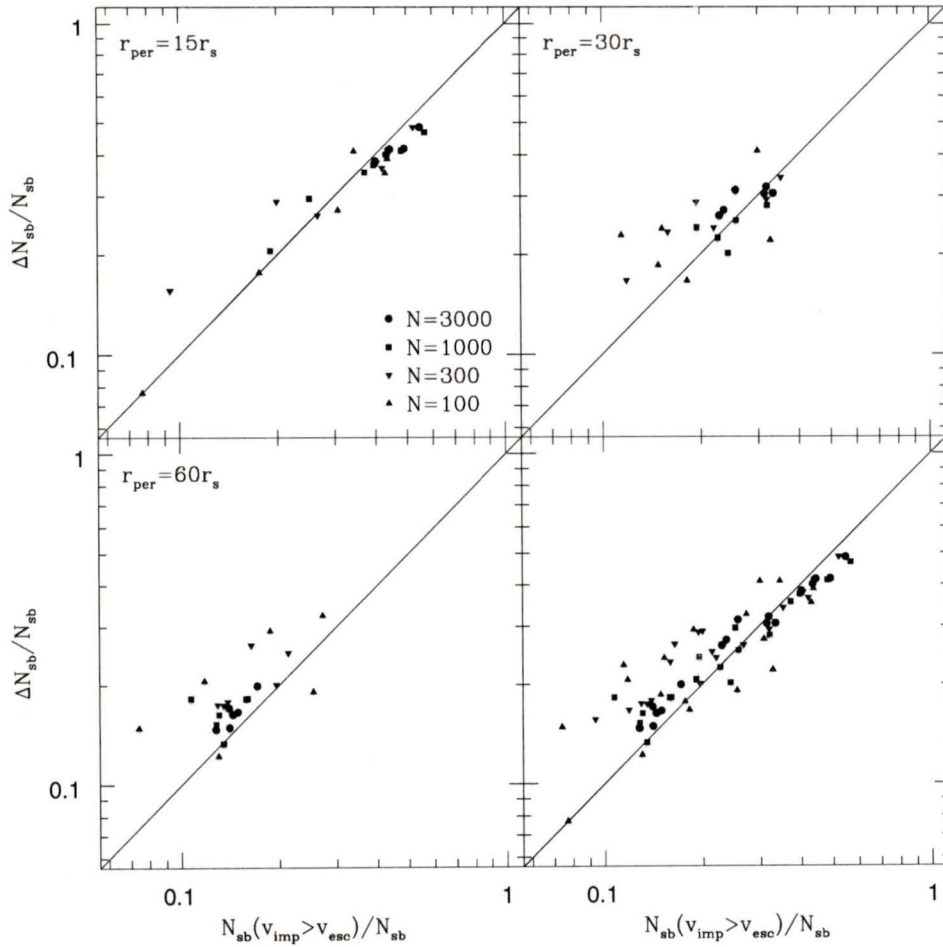


Figure 2.20: Change in self-bound mass between consecutive apocentric passages versus mass loss predicted by impulse approximation for optimally softened halos on elliptical orbits with $r_{\text{per}}/r_s = 15, 30, 60$ and total sample (lower right panel).

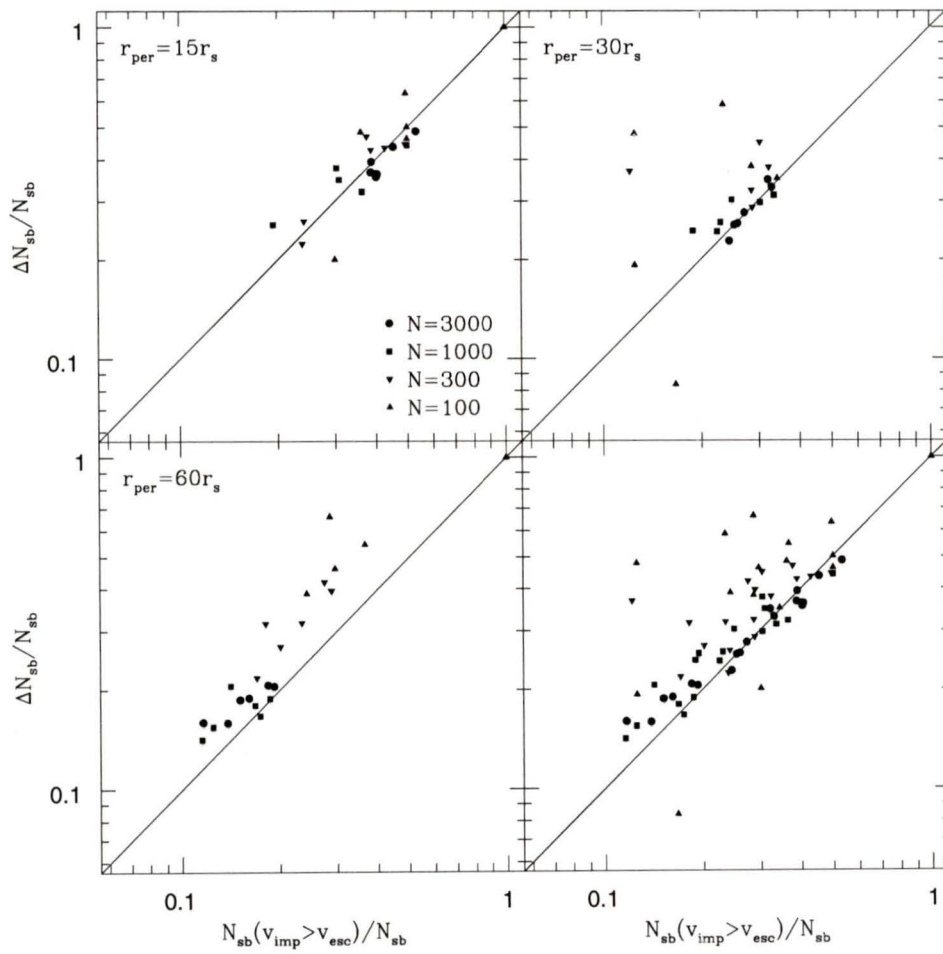


Figure 2.21: Same as Figure 2.20 for non-optimally softened halos.

predict the total amount of mass lost by the satellite as a function of time.

In the absence of any readjustment of halo particle positions, the tidal approximation predicts that the satellite halo is stripped down to the tidal radius in a single episode of mass loss. Clearly this is not what we observe in our simulations. Figure 2.7 shows that a halo simulated with sufficient mass resolution loses approximately the same fraction of mass during each pericentric passage. If we assume that the mass loss predicted by the tidal approximation corresponds to the fraction of mass lost each time the satellite passes through pericentre we predict that the mass of the satellite decreases exponentially with time:

$$\frac{N_{sb}}{N} = 10^{\frac{t}{t_{orb}} \log\left(\frac{N(r < r_t)}{N}\right)} \quad (2.23)$$

where $N(r < r_t)$ is the number of particles within the pericentric tidal radius. A similar prediction is obtained if the impulse approximation is used to calibrate the rate of mass loss. These predictions are shown in Figure 2.22 alongside the self-bound mass curves of the optimally softened $N = 3000$ satellite halos for the three different orbits. In all three cases, the cumulative prediction of the impulse approximation is more accurate than that of the tidal approximation. Note that since these predictions are based solely on an extrapolation of the prediction for the first orbit, discrepancies between the two initial estimates are amplified after each subsequent orbital period. Both tidal and impulse approximations substantially over-predict the rate of mass loss in the $r_{per} = 15 r_s$ and $r_{per} = 30 r_s$ orbits, however, both methods under-predict the mass loss rate of the $r_{per} = 60 r_s$ orbit. As previously noted, the tidal approximation more severely under-predicts mass loss for the latter orbit, thus the cumulative mass loss prediction of the impulse approximation is considerably more accurate in this case.

An additional prediction of the mass loss rate is obtained via repeated applications of the impulse approximation, i.e. by performing the procedure described in

section 2.4.2 for the first orbit, resetting the positions and velocities of the remaining bound particles to the centre of mass frame, repeating the procedure for the next orbit, and so on. The results are plotted as the right-angled, step-like curves in Figure 2.22. Note that the observed self-bound mass curves appear to lag the equally spaced impulse approximation steps because of a decrease in the orbital energy of the satellite halo. This effect was previously observed in the shell galaxy formation simulations of Heisler & White (1990), who noted that “tails stripped off the satellite during an encounter cause an effective drag which reduces the orbital energy of its core.”

The predictions of the repeated impulse approximation are of comparable accuracy to those of the extrapolated impulse approximation: the former method is more accurate for the $r_{per} = 15 r_s$ orbit and the latter is more accurate for the $r_{per} = 60 r_s$ orbit. The error in the predicted disruption timescale for all three methods is shown in Table 2.4. We define the disruption timescale as the time for the self-bound mass of the halo to decrease by 50% ($t_{50\%}$) or 90% ($t_{90\%}$) of the initial mass. Since the repeated impulse approximation predicts the remaining satellite mass after each orbit, the time resolution of this method is limited to a radial period. Nevertheless, this method predicts the disruption time to within one radial period for all but the $t_{90\%}$, $r_{per} = 60 r_s$ case, and to within 30% for all but the $t_{50\%}$, $r_{per} = 15 r_s$ case. The exponential extrapolation of the impulse approximation is equally accurate, predicting disruption times to 30% or better in all cases. In comparison, the prediction of the extrapolated tidal approximation misses the mark by as much as 80% or almost nine radial periods in some instances.

Clearly the impulse approximation-based predictions are superior to those based on the tidal approximation. However, the repeated impulse approximation underpredicts the disruption timescale in all cases, whereas the disruption times predicted by exponential extrapolations are greater than those observed in some cases and less in others (see Table 2.4). Thus, making conservative (over-) estimates of the disruption

timescale of satellite halos remains problematic using these methods. Recall that our ultimate objective is to determine whether tidal stripping alone is sufficient to account for overmerging in the central regions of clusters. To this end we prefer to overestimate satellite disruption times so that the distribution of surviving substructure predicted by our model represents an upper limit to the amount of substructure we can expect to observe in cosmological simulations. Any deficit we find in the density of surviving subhalos relative to that of galaxies in clusters can therefore be trusted as legitimate signature of overmerging.

	tidal exp		impulse exp		impulse rep		obs
r_{per}	$\frac{t_{50\%}}{t_{orb}}$	error (%)	$\frac{t_{50\%}}{t_{orb}}$	error (%)	$\frac{t_{50\%}}{t_{orb}}$	error (%)	$\frac{t_{50\%}}{t_{orb}}$
15	0.82	-0.38 (32%)	0.87	-0.33 (27%)	0.50	-0.70 (54%)	1.29
30	1.61	+0.03 (2%)	1.80	+1.22 (14%)	1.50	-0.08 (5%)	1.58
60	6.38	+2.85 (80%)	4.60	+1.07 (30%)	2.50	-1.03 (29%)	3.55
	tidal exp		impulse exp		impulse rep		obs
r_{per}	$\frac{t_{90\%}}{t_{orb}}$	error (%)	$\frac{t_{90\%}}{t_{orb}}$	error (%)	$\frac{t_{90\%}}{t_{orb}}$	error (%)	$\frac{t_{90\%}}{t_{orb}}$
15	2.72	-1.26 (32%)	2.89	-1.09 (27%)	3.50	-0.48 (12%)	3.98
30	5.36	-0.97 (15%)	5.99	-0.34 (5%)	5.50	-0.88 (13%)	6.30
60	21.18	+8.88 (72%)	15.27	-2.97 (24%)	9.50	-2.20 (23%)	12.29

Table 2.4: Predicted and observed disruption times for optimally softened $N = 3000$ satellite halos. Exponential extrapolation of tidal and impulse approximations (tidal exp, impulse exp), repeated application of impulse approximation (impulse rep) and disruption times observed in simulations (obs) are shown in units of radial period for 50% and 90% mass loss.

2.5 Summary

In this chapter, we have described a series of N -body experiments which simulate the orbit of a satellite galaxy in a cluster potential. These simulations explored a range of mass and force resolution, and orbits with three different apocentre-to-pericentre ratios. We followed the tidal disruption of the satellite halo by calculating its self-bound mass and observed changes in its internal structure by examining the time

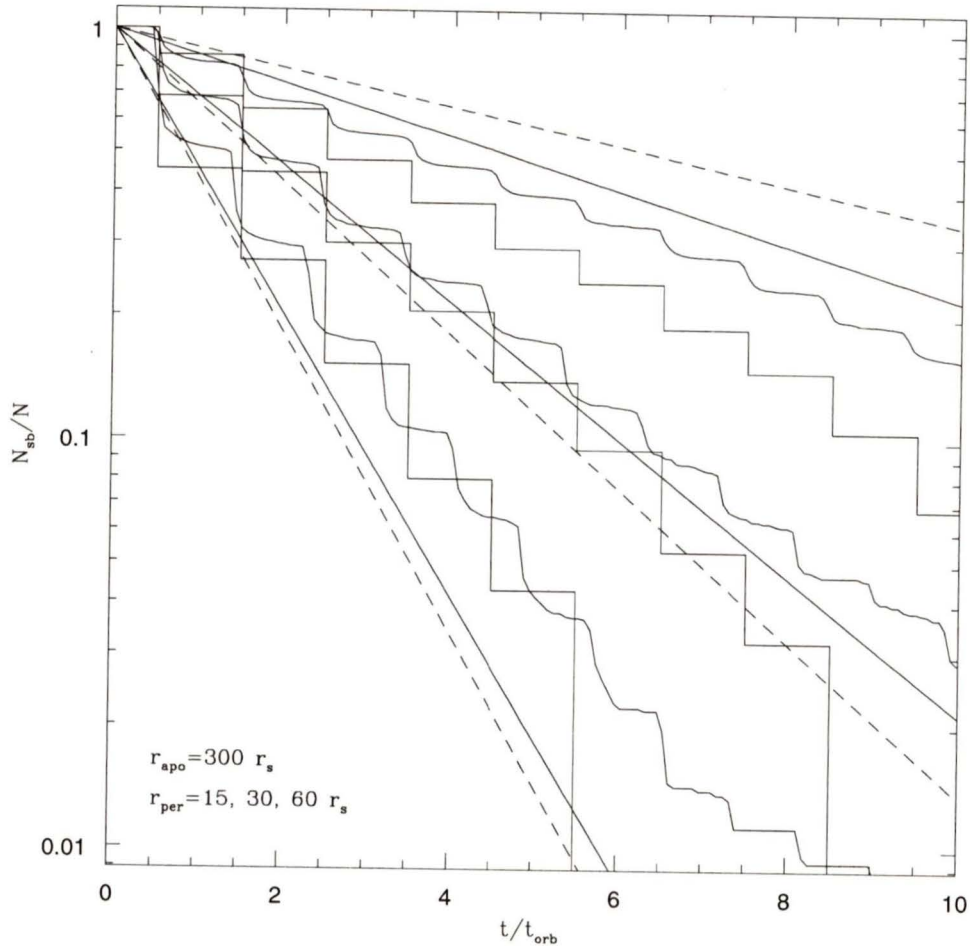


Figure 2.22: Cumulative mass loss predicted by three different methods. Straight dashed line shows tidal approximation prediction assuming a constant fraction of the remaining self-bound mass is lost each orbit. Straight solid line is the same for the impulse approximation. Step-like solid line shows the prediction for repeated applications of the impulse approximation. Simulation results for the optimally softened $N = 3000$ halos are shown as sloping steps. Upper, middle, and lower sets of curves correspond to orbits with apocentric radius $r_{ap} = 300 r_s$, and pericentric radii $r_{per} = 60, 30$, and $15 r_s$, respectively.

Chapter 3

Dynamical Evolution of Galaxy Clusters

Abstract

A series of simulations of satellite halos in a variety of radial and circular orbits reveal that simple methods of modeling tidal mass loss rates systematically under-predict disruption timescales of satellites on non-radial orbits. As an alternative, we use our simulation data to define an empirical relationship between the fraction of mass lost in the first orbit and the disruption timescale of the satellite. This relationship is used to construct a toy model for cluster evolution by solving for the orbital parameters of 1000 particles randomly selected from an NFW halo and using the impulse approximation to predict the mass lost in the first orbit by satellite halos corresponding to these particles. The resulting distribution of disruption timescales allows us to determine the spatial distribution of substructure in a cluster after dynamical evolution for a Hubble time. The number density profile of substructure halos is compared with the results of cosmological simulations and with observations from the Canadian Network for Observational Cosmology (CNOC) cluster survey. We find that tidal disruption erases substructure in the central regions of the cluster, and that the subhalo distribution is not consistent with the observed distribution of cluster galaxies. This suggests that fully self-consistent hydrodynamical simulations may be needed to properly model the formation of galaxy clusters.

In the previous chapter we investigated the tidal disruption of satellite halos by a massive host and developed methods for predicting mass loss and disruption

timescales. We now seek to further test these methods over a wide range of orbital conditions and, if necessary, to refine or improve upon them. Our goal is to apply these semi-analytic recipes for estimating mass loss to a large sample of satellite galaxies in order to investigate the dynamical evolution of a galaxy cluster. Ultimately we wish to compare the surviving substructure predicted by our model with the results of high resolution cosmological simulations as well as observations of galaxy clusters.

This chapter is organized as follows. In Section 3.1 we present additional simulations of the tidal disruption of a satellite galaxies which explore the parameter space of possible bound orbits. We use these to derive an empirical relationship between the fraction of mass lost in the first orbit and the disruption timescale of the satellite. This relationship in turn is used to construct a toy model for cluster evolution in Section 3.2. The spatial distribution of surviving substructure predicted by our model is compared with the results of cosmological simulations as well as observations from the Canadian Network for Observational Cosmology (CNOC) cluster survey in Section 3.3.

3.1 Supplementary Simulations

In order to gain a more complete understanding of the dependence of mass loss on the orbit of a satellite halo, we perform an additional set of simulations of satellites in static host potentials. We follow the procedure described in Section 2.2 to initialize these runs, and use only optimally softened $N = 3000$ particle halos in order to avoid numerical effects which lead to the premature disruption of insufficiently resolved satellite halos. The range of parameter space explored in these simulations is shown in Figure 3.1 and Table 3.1. The simulations described in Chapter 2 featured orbits with $r_{per} = 15, 30,$ and $60 r_s$ and $r_{ap} = 300 r_s$. We perform a similar series of simulations with orbits having the same set of pericentric radii, but a smaller apocentric radius, $r_{ap} = 100 r_s$. Another set of runs consists of orbits with the same pericentric radius

$r_{per} = 15 r_s$ and a range of different apocentric radii. Finally we simulate seven different circular orbits with orbital radii ranging from $r_{circ} = 15 r_s$ to $r_{circ} = 300 r_s$. Altogether this suite of simulations represents a fairly complete sample of orbits, with apocentre-to-pericentre ratios ranging from 1:1 to 20:1.

orbital parameters											
r_{ap}	r_{per}	v_{ap}	v_{per}	J	E_{orb}	e	ϵ_{circ}	t_{orb}	$\frac{t_{orb}}{t_{cross}}$	$\frac{t_{df}}{t_{orb}}$	
300	15	0.224	4.479	67.18	-2.28	0.905	0.261	556.6	17.6	20.0	
300	30	0.376	3.762	112.86	-2.24	0.818	0.430	581.7	18.4	28.3	
300	60	0.594	3.913	178.09	-2.13	0.538	0.751	639.9	20.2	35.4	
100	15	0.587	3.911	57.67	-4.66	0.739	0.505	150.4	4.8	13.8	
100	30	0.941	3.138	94.13	-4.39	0.538	0.751	170.8	5.4	16.5	
100	60	1.384	2.307	138.43	-3.87	0.250	0.949	218.0	6.9	15.5	
60	15	0.887	3.509	52.64	-6.15	0.600	0.665	88.5	17.6	16.2	
75	15	0.739	3.697	55.45	-5.47	0.631	0.592	110.8	3.5	11.9	
150	15	0.416	4.164	62.47	-3.64	0.818	0.398	238.9	7.6	10.4	
—	15	2.061	2.061	30.92	-10.18	0	1	45.7	1.4	21.7	
—	30	2.067	2.067	61.92	-7.17	0	1	91.2	2.9	13.2	
—	60	1.912	1.912	114.72	-4.71	0	1	197.2	6.2	9.7	
—	75	1.838	1.838	137.85	-4.06	0	1	256.4	8.1	7.7	
—	100	1.732	1.732	173.20	-3.33	0	1	362.8	11.5	6.4	
—	150	1.570	1.570	235.50	-2.49	0	1	600.3	19.0	3.5	
—	300	1.287	1.287	386.10	-1.48	0	1	1464.5	46.3	35.4	

Table 3.1: Numerical parameters of our simulations, where $e = (r_{ap} - r_{per}) / (r_{ap} + r_{per})$ is the generalized orbital eccentricity and $\epsilon_{circ} = J / J_{circ}(E)$ is the orbital circularity, defined by the ratio between the orbital angular momentum and the angular momentum of a circular orbit with the same energy. Upper and lower sections show radial and circular orbits (where $r_{circ} = r_{per}$), respectively.

3.1.1 Mass Loss

The self-bound mass curves of five radial orbits with the same pericentric radii, $r_{per} = 15 r_s$ are shown in Figure 3.2. Even though the apocentre-to-pericentre ratios for these orbits range from 4:1 to 20:1, mass loss occurs at virtually the same rate in all five cases; these halos consistently lose between 40% to 50% of their remaining

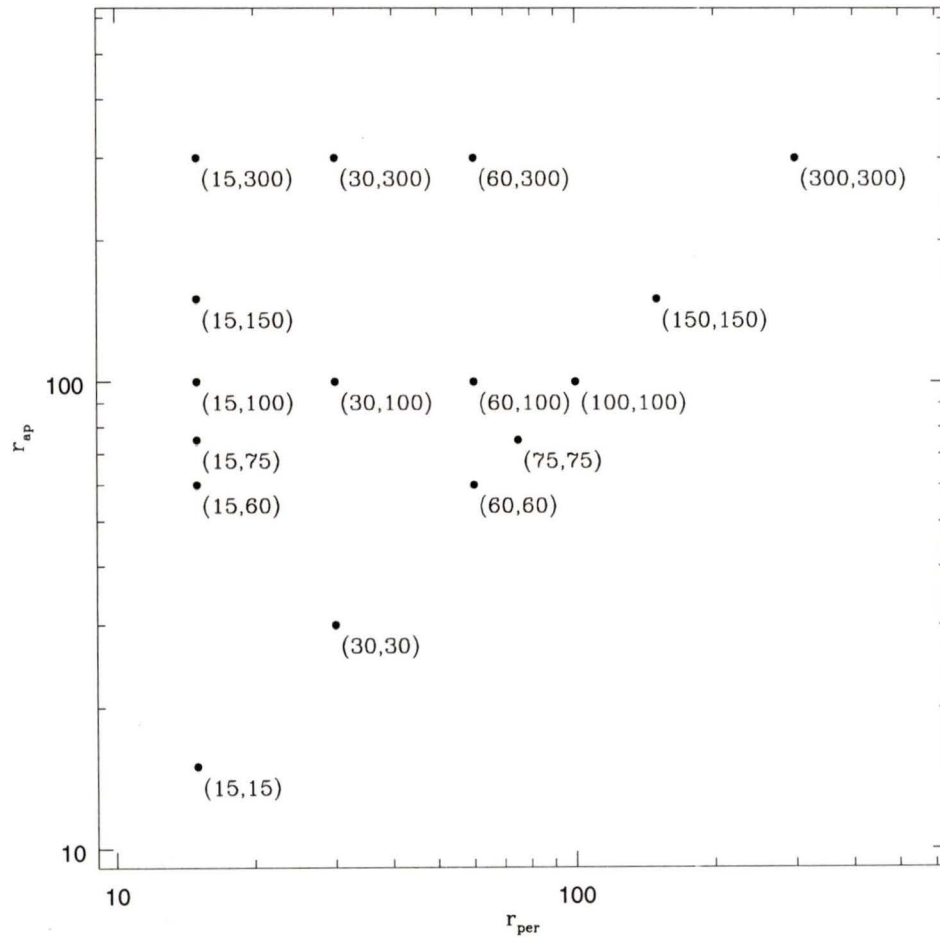


Figure 3.1: Pericentric and apocentric radii (r_{per} , r_{ap}) of orbits for all optimally softened $N = 3000$ satellite simulations.

self-bound mass per orbit. Satellites with smaller apocentric radii continue to lose significant mass between pericentric passages because, unlike those on highly radial orbits, they do not move far enough from the centre of the host potential to escape strong tidal forces. Figure 2.17 shows that the tidal radius is smaller than the initial size of the satellite (i.e. $r_t < r_{cut} = 10 r_s$) at all orbital radii less than $\sim 100 r_s$. As a result, the mass loss experienced by satellites which remain in this region throughout their orbits is more continuous and less than it is for satellites with larger apocentric radii. Also shown in Figure 3.2 is the self-bound mass of a satellite on a circular orbit with an orbital radius of $15 r_s$. This satellite loses mass continuously at rate similar to that experienced by the other satellites *at pericentre*, and therefore disrupts on a much faster timescale.

The pericentric radius of a satellite's orbit is clearly a major determinant of its mass loss rate. The apocentric radius and orbital circularity also appear to play a role, however. Figure 3.3 shows a comparison of the self-bound mass of six satellites on orbits with $r_{ap} = 300$ or $100 r_s$, and either of three different pericentric radii, $r_{per} = 15, 30$, or $60 r_s$. In all cases, the satellite on the less radial $r_{ap} = 100 r_s$ orbit loses significantly more mass during the first orbit compared to the satellite with the same pericentric radius but more distant apocentre. However, the mass loss rate of the $r_{ap} = 100 r_s$ satellites begins to decrease after the second or third orbit, and these satellites start to retain more mass than do their $r_{ap} = 300 r_s$ counterparts. This effect seems most pronounced for orbits with larger pericentric radii. Recall that for orbits with $r_{per} = 15 r_s$, changing the apocentre-to-pericentre ratio by a factor of five had little effect on the overall mass loss rate, whereas in this case decreasing the apocentric radius by a factor of three results in much different mass loss patterns for orbits with $r_{per} = 30$ and $60 r_s$.

Since satellites on different orbits with the same pericentric radius lose different amounts of mass, our implementation of the tidal approximation will inevitably fail to make accurate predictions in many cases. In addition, methods based on a simple

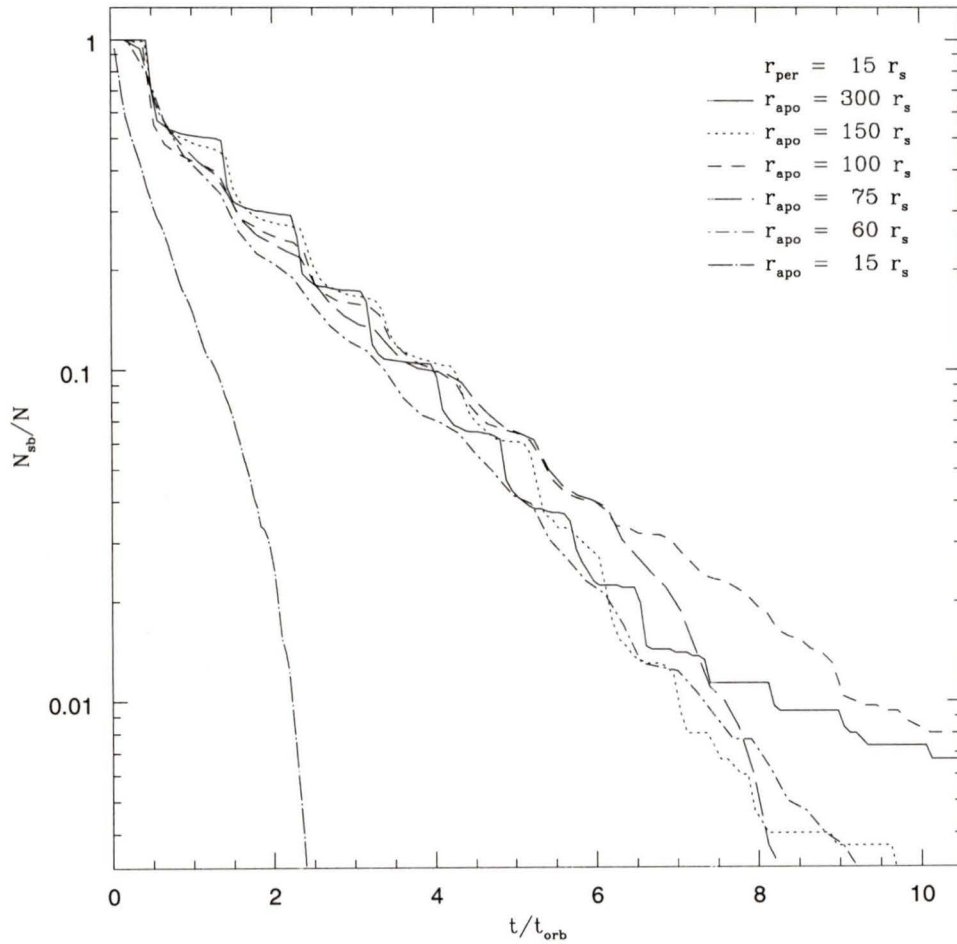


Figure 3.2: Time evolution of self-bound mass for optimally softened $N = 3000$ satellites on orbits with same pericentric radius, $r_{per} = 15 r_s$, but different apocentric radii, $r_{ap} = 300, 150, 100, 75, 60,$ and $15 r_s$ (circular orbit).

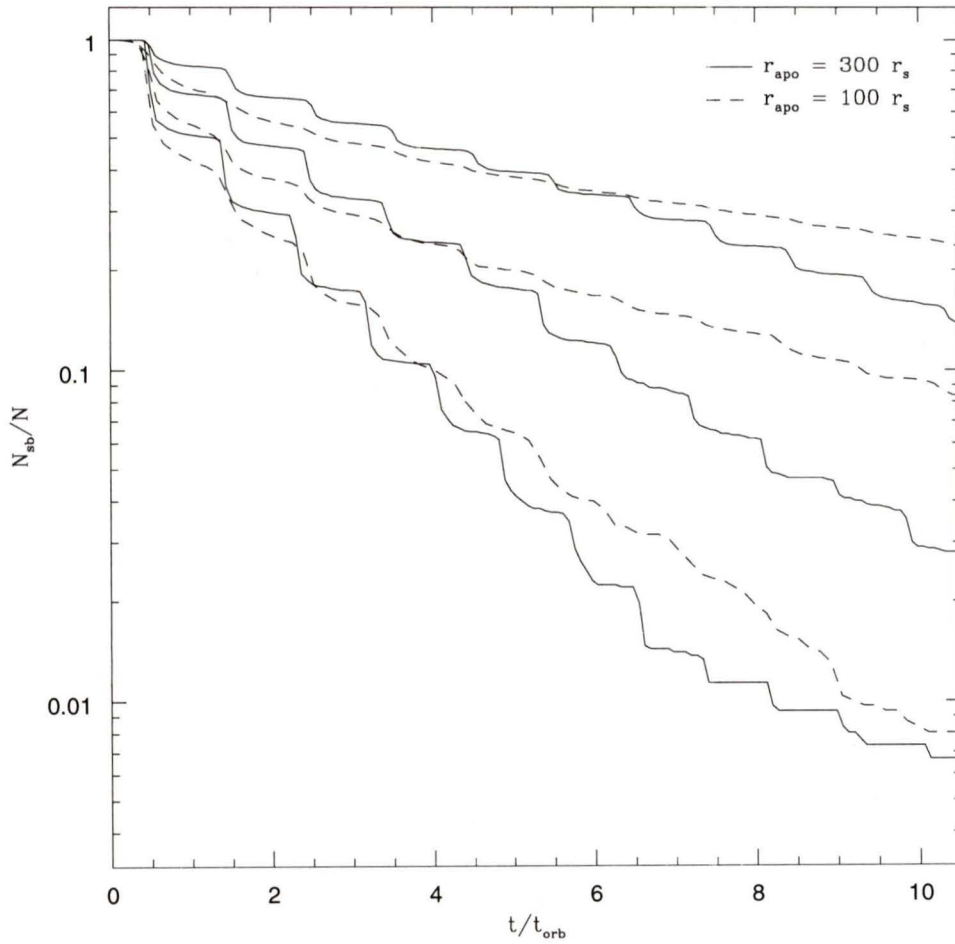


Figure 3.3: Time evolution of self-bound mass for optimally softened $N = 3000$ satellites on orbits with apocentric radii $r_{ap} = 300$ and $100 r_s$. Upper, middle, and lower sets of curves correspond to orbits with pericentric radii $r_{per} = 60, 30,$ and $15 r_s$, respectively.

extrapolation of mass loss over the first orbit are unable to account for subsequent changes in the mass loss rate, as observed in satellites on orbits with $r_{ap} = 100 r_s$ and $r_{per} = 30$, and $60 r_s$. Figure 3.4 for shows a similar change in the slope of the self-bound mass curves of satellites on circular orbits. Based on our previous simulations of radial orbits, one might expect the rate of mass loss to remain constant with time during a circular orbit in the absence of dynamical friction since the orbital radius is fixed. Instead, the self-bound mass curves show a steep decline during the first orbit, followed by a more gentle decrease in subsequent orbits. The mass loss rate after the first orbit is very similar among satellites on the four intermediate circular orbits ($60 r_s \leq r_{circ} \leq 150 r_s$), equal to $\sim 5\%$ per orbit. Satellites on the two closest orbits are stripped much more violently, losing 70% to 80% of their mass after their first orbit, and thereafter both lose mass at a faster rate relative to the more distant satellites. Note that mass loss is observed even in our most distant circular orbit, $r_{circ} = 300 r_s$, despite the fact that the tidal radius in this case is significantly larger than the initial size of the satellite (see Figure 2.17). Because the orbital period of this satellite is comparable to the relaxation time ($t_{orb} \simeq 46 t_{cross}$, $t_{relax} \simeq 104 t_{cross}$), numerical relaxation effects probably contribute to the mass loss that begins to occur after the third orbit.

In summary, mass loss occurs very differently in circular versus radial orbits. Satellites on radial orbits with apocentre-to-pericentre ratios greater than 3:1 lose approximately equal fractions of their remaining mass each time they pass through pericentre. Tidal stripping in circular orbits is characterized by a sharp decline in satellite mass during the first orbit followed by continuous mass loss at a reduced rate in subsequent orbits.

3.1.2 Disruption Timescale Predictions

In Chapter 2 we found that the two impulse approximation-based methods were most accurate in predicting the cumulative mass loss and disruption timescales of

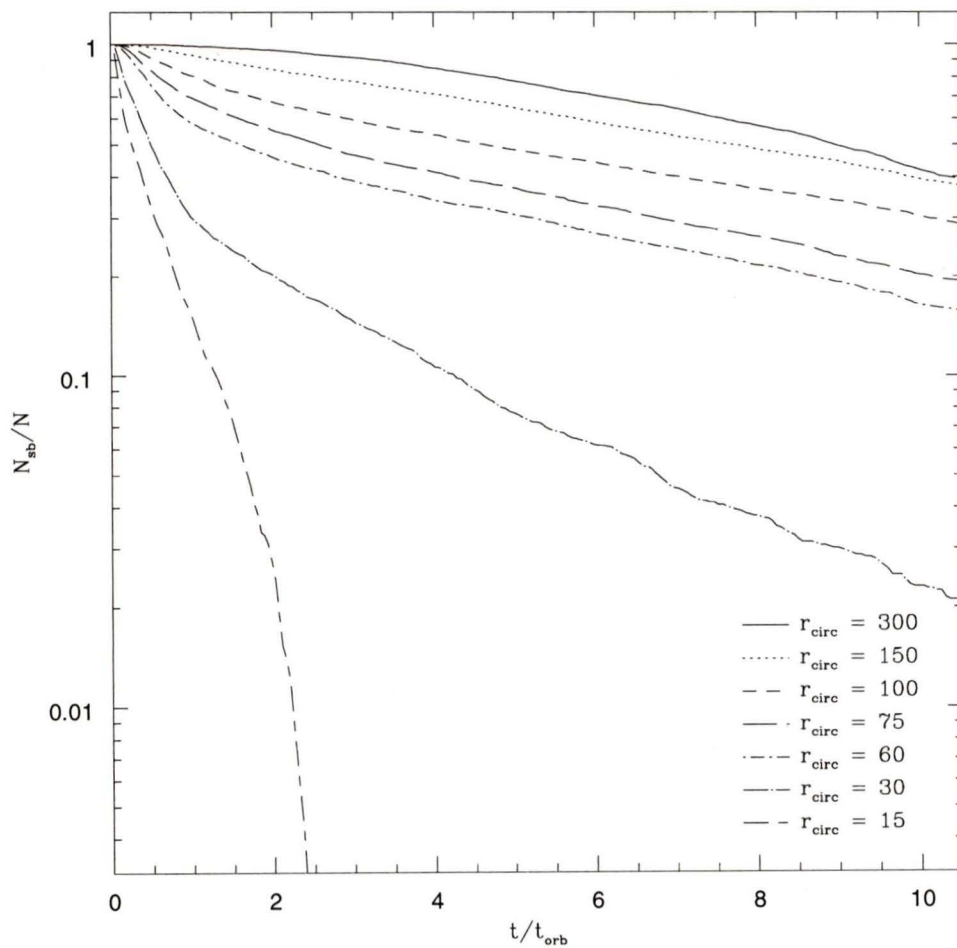


Figure 3.4: Time evolution of self-bound mass for optimally softened $N = 3000$ satellites on circular orbits with various orbital radii (r_{circ}).

satellite halos. The results of applying these methods to our new series of orbits are shown in Figures 3.5 and 3.6. As anticipated, the exponentially decreasing extrapolation of the first-orbit impulse approximation prediction severely overestimates mass loss in satellites on low eccentricity orbits. The observed and predicted 50% and 90% disruption timescales ($t_{50\%}$ and $t_{90\%}$, respectively) listed in Table 3.2 show that our impulse approximation-based predictions tend to grossly underestimate disruption times. Our methods of modeling mass loss are therefore ill-suited to making conservative predictions of satellite disruption timescales. However, on closer inspection Figures 3.5 and 3.6 show that in general our mass loss predictions are fairly accurate *for the first orbit*. The predictions of the impulse approximation are compared with the actual change in self-bound mass after the first orbit in Figure 3.7. The agreement is quite good for most of the 16 different orbits: the error is less than 20% in all but two cases, and the mean and median errors are 6% and 9%, respectively.

Bearing this result in mind, we attempt to find a correlation between the disruption time of a satellite and the fraction of mass it loses in its first orbit, since we can predict the latter to reasonable accuracy using the impulse approximation. Figure 3.8 shows the 50%, 70% and 90% disruption timescales as a function of the remaining mass of a satellite after its first orbit. As one might expect, the greater the initial mass loss experienced by a satellite, the sooner it is disrupted. Although there is too much scatter in the relation to make precise predictions, one can use the data to define an upper limit to the disruption time for a given initial mass loss. This relationship between disruption time and mass loss, hereafter the $t_{dis} - \Delta m$ relation, shown as the solid line in Figure 3.8, is given by

$$\log\left(\frac{t_{90\%}}{t_{orb}}\right) = C_1 \log\left(1 - \frac{\Delta N_{sb}}{N_{sb}}\right) + C_2 \quad (3.1)$$

where C_1 and C_2 are the logarithmic slope and intercept of the line, respectively. The value of the slope constant, $C_1 = 1.7$, is dictated by the upper envelope of the

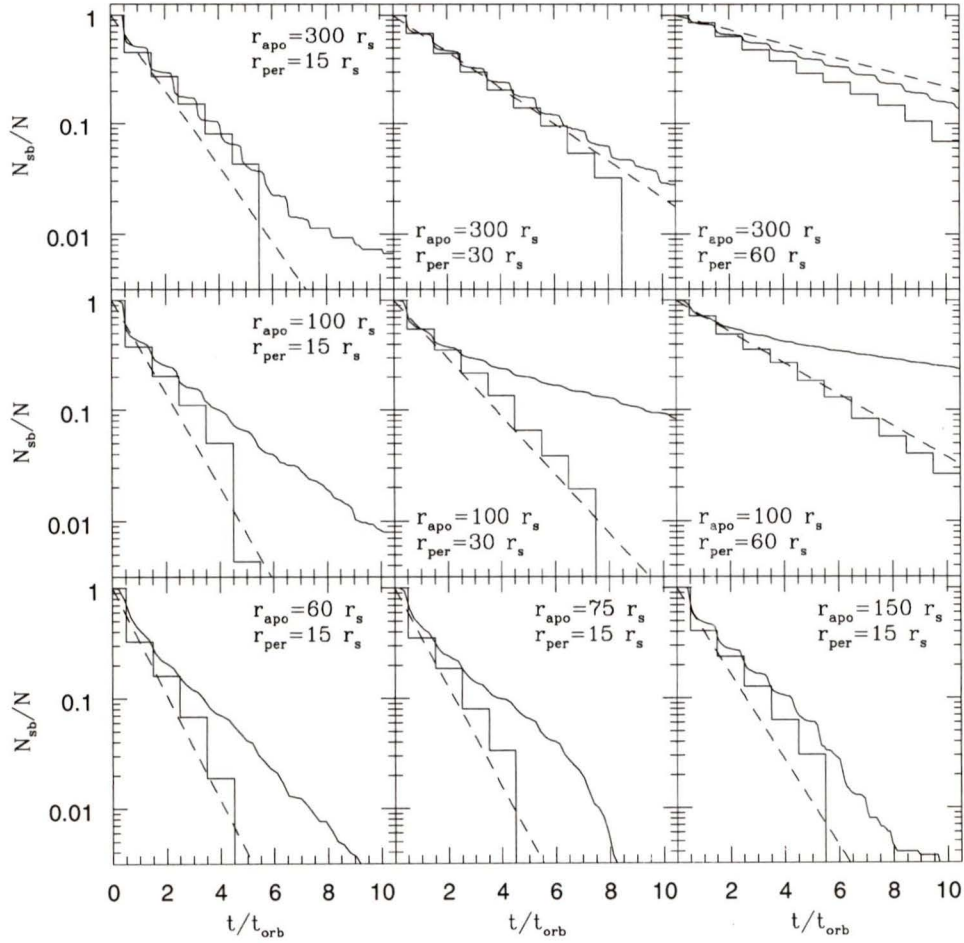


Figure 3.5: Cumulative mass loss predictions for nine different radial orbits. Straight dashed line shows the impulse approximation prediction assuming a constant fraction of the remaining self-bound mass is lost each orbit. Step-like solid line shows the prediction for repeated applications of the impulse approximation. Solid curves show simulation results for optimally softened $N = 3000$ halos. Upper, middle, and lower sets of curves correspond to orbits with apocentric radius $r_{ap} = 300 r_s$, and pericentric radii $r_{per} = 60, 30$, and $15 r_s$, respectively.

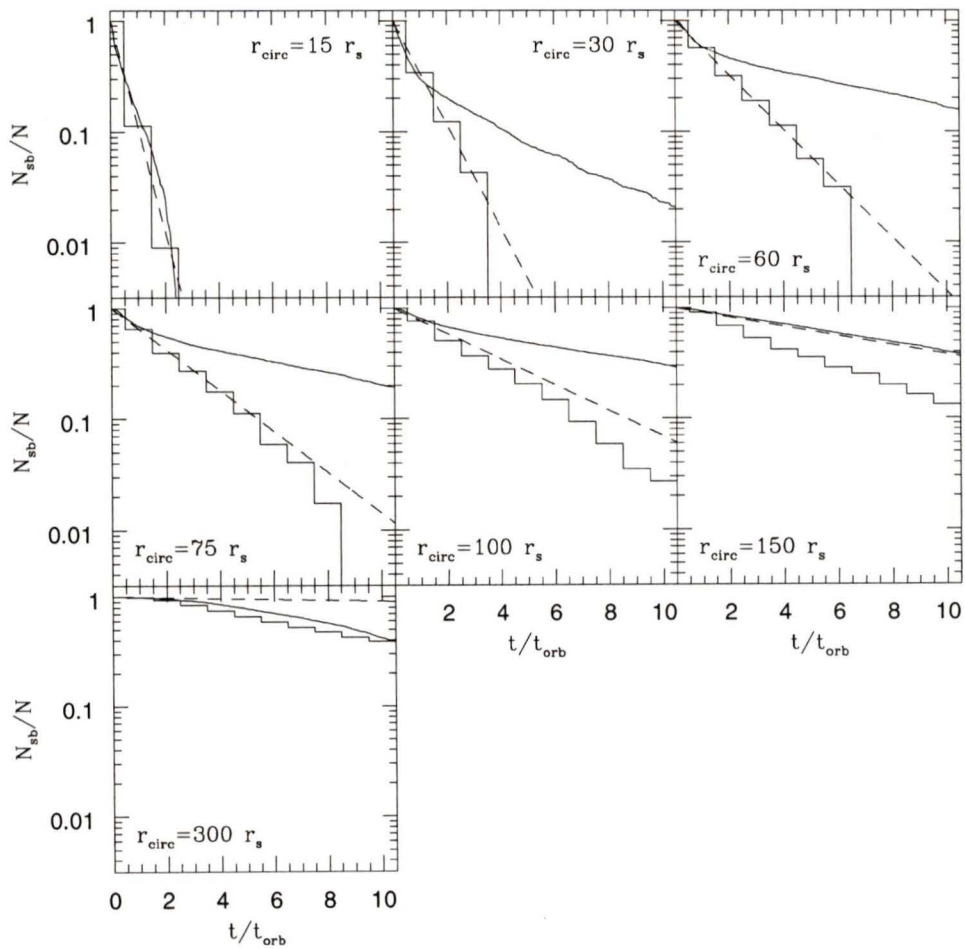


Figure 3.6: Same as Figure 3.5 for seven different circular orbits.

		impulse exp		impulse rep		obs
r_{ap}	r_{per}	$\frac{t_{50\%}}{t_{orb}}$	error (%)	$\frac{t_{50\%}}{t_{orb}}$	error (%)	$\frac{t_{50\%}}{t_{orb}}$
300	15	0.87	-0.33 (27%)	0.50	-0.70 (54%)	1.29
300	30	1.80	+1.22 (14%)	1.50	-0.08 (5%)	1.58
300	60	4.60	+1.07 (30%)	2.50	-1.03 (29%)	3.55
100	15	0.71	+0.12 (19%)	0.50	-0.13 (21%)	0.63
100	30	1.14	-0.18 (14%)	1.50	+0.18 (14%)	1.32
100	60	2.12	+0.44 (16%)	2.50	-0.16 (6%)	2.66
60	15	0.63	-0.15 (13%)	0.50	-0.28 (36%)	0.78
75	15	0.67	-0.09 (12%)	0.50	-0.26 (34%)	0.76
150	15	0.77	-0.13 (14%)	0.50	-0.40 (44%)	0.90
15	15	0.32	+0.06 (23%)	0.50	+0.24 (92%)	0.26
30	30	0.65	+0.14 (28%)	0.50	-0.04 (9%)	0.49
60	60	1.23	-0.39 (24%)	1.50	-0.12 (7%)	1.62
75	75	1.63	-0.96 (37%)	1.50	-1.19 (45%)	2.59
100	100	2.60	-2.03 (44%)	2.50	-2.13 (46%)	4.63
150	150	7.13	+0.59 (8%)	3.50	-4.22 (55%)	7.72
300	300	73.9	-64.9 (724%)	3.50	-5.46 (61%)	8.96
		impulse exp		impulse rep		obs
r_{ap}	r_{per}	$\frac{t_{90\%}}{t_{orb}}$	error (%)	$\frac{t_{90\%}}{t_{orb}}$	error (%)	$\frac{t_{90\%}}{t_{orb}}$
300	15	2.89	-1.09 (27%)	3.50	-0.48 (12%)	3.98
300	30	5.99	-0.34 (5%)	5.50	-0.88 (13%)	6.32
300	60	15.27	-2.97 (24%)	9.50	-2.20 (23%)	12.29
100	15	2.36	-1.74 (27%)	0.50	-0.70 (58%)	4.01
100	30	3.79	-5.51 (14%)	1.50	-0.08 (5%)	9.30
100	60	7.03	< -3 (> 30%)	2.50	-1.03 (29%)	> 10
60	15	2.08	-1.30 (33%)	0.50	-0.70 (58%)	3.38
75	15	2.21	-1.69 (43%)	1.50	-0.08 (5%)	3.90
150	15	2.56	-1.67 (39%)	2.50	-1.03 (29%)	4.23
15	15	1.06	-0.17 (13%)	1.50	+0.21 (16%)	1.29
30	30	2.14	-2.10 (50%)	2.50	-1.74 (41%)	4.24
60	60	4.09	< -6 (> 60%)	4.50	< -5.5 (> 45%)	> 10
75	75	5.42	< -4 (> 40%)	5.50	< -4.5 (> 45%)	> 10
100	100	8.62	< -1 (> 10%)	6.50	< -3.5 (> 35%)	> 10
150	150	23.7	- (-)	> 10	- (-)	> 10
300	300	245	- (-)	> 10	- (-)	> 10

Table 3.2: Predicted and observed disruption times for optimally softened $N = 3000$ satellite halos. Exponential extrapolation of impulse approximations (impulse exp), repeated application of impulse approximation (impulse rep) and disruption times observed in simulations (obs) are shown in units of radial period for 50% and 90% mass loss.

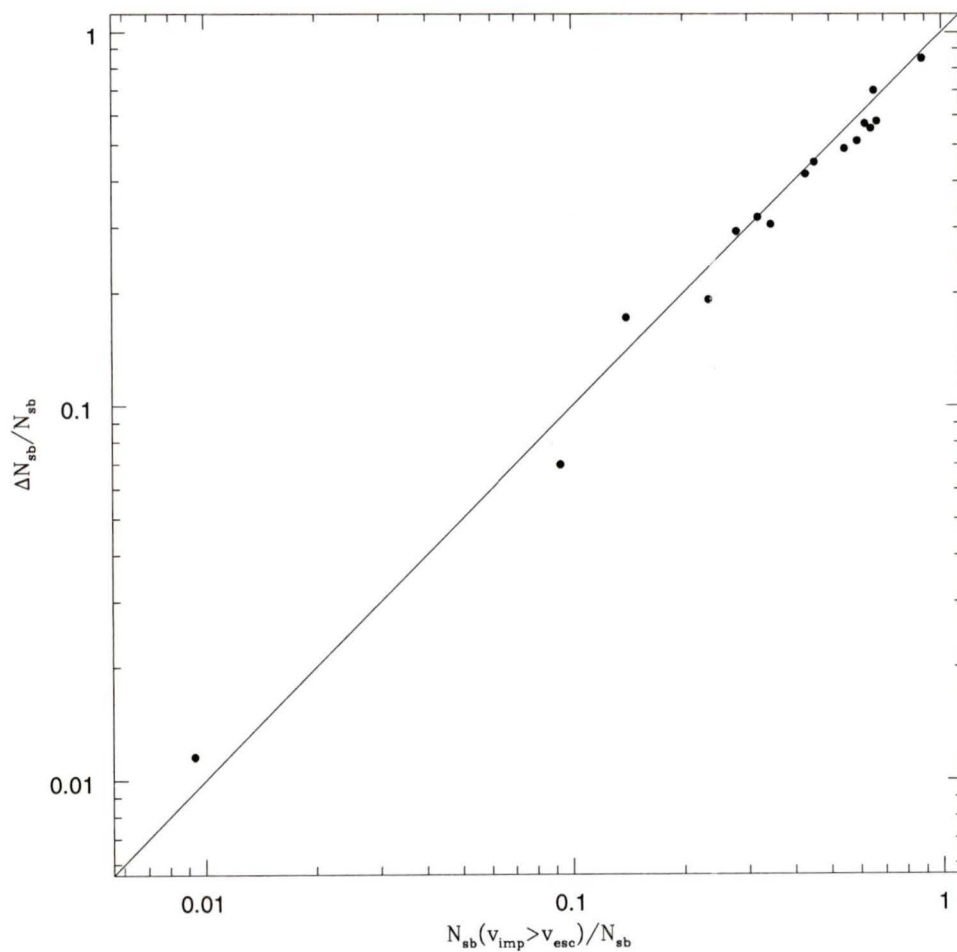


Figure 3.7: Change in self-bound mass in first orbit versus mass loss predicted by impulse approximation for optimally softened $N = 3000$ halos on various orbits.

the data in Figure 3.8, which is primarily defined by the three points that lie closest to the line (at $1 - \Delta N_{sb}/N_{sb} \simeq 0.15, 0.3, \text{ and } 0.7$). Solving for the intercept constant in equation (3.1) with the additional constraint that $t_{90\%} = 1 t_{orb}$ for $\Delta N_{sb}/N_{sb} = 0.9$ gives a value of $C_2 = 1.7$. The $t_{dis} - \Delta m$ relation with these values encompasses the data points in Figure 3.8 by a safe margin, and therefore provides a conservative upper limit to their disruption times. Note that the 70% and/or 90% disruption times were longer than the duration of the simulation, 10 radial periods, for many of the circular orbits (see Table 3.2) and therefore do not appear in Figure 3.8. In practice, this lower bound on the disruption timescales of these satellites is much longer than a Hubble time for any reasonable choice of physical units, i.e. $10 t_{orb} \gg 1/H_0$ for all orbits with $r_{per} \geq 60 r_s$.

3.2 A Toy Model for Cluster Evolution

In this section we use our results to investigate the dynamical evolution of a galaxy cluster. Our objective is not to precisely model cluster dynamics, but simply to determine whether tidal stripping alone is sufficient to account for overmerging in collisionless N -body simulations. The simulations we have conducted indicate that satellites which pass near the inner $1 R_s$ of cluster are relieved of 50% or more of their mass in a single orbit. The survival of substructure in the central regions of the cluster therefore seems highly unlikely.

We construct our cluster model as follows:

1. generate a high resolution NFW halo with the same mass, $M_{host} = 300 m_{sat}$, size, $R_s = 10 r_s$, and concentration, $c = 10$ as the static host potential in our previous simulations. We use $N = 3 \times 10^5$ particles and a softening length, $\epsilon = 0.18 R_s$, given by van Kampen's scaling law (equation 2.15). This produces a very smooth mass profile, $M(r)$, for the calculation of the velocity dispersion

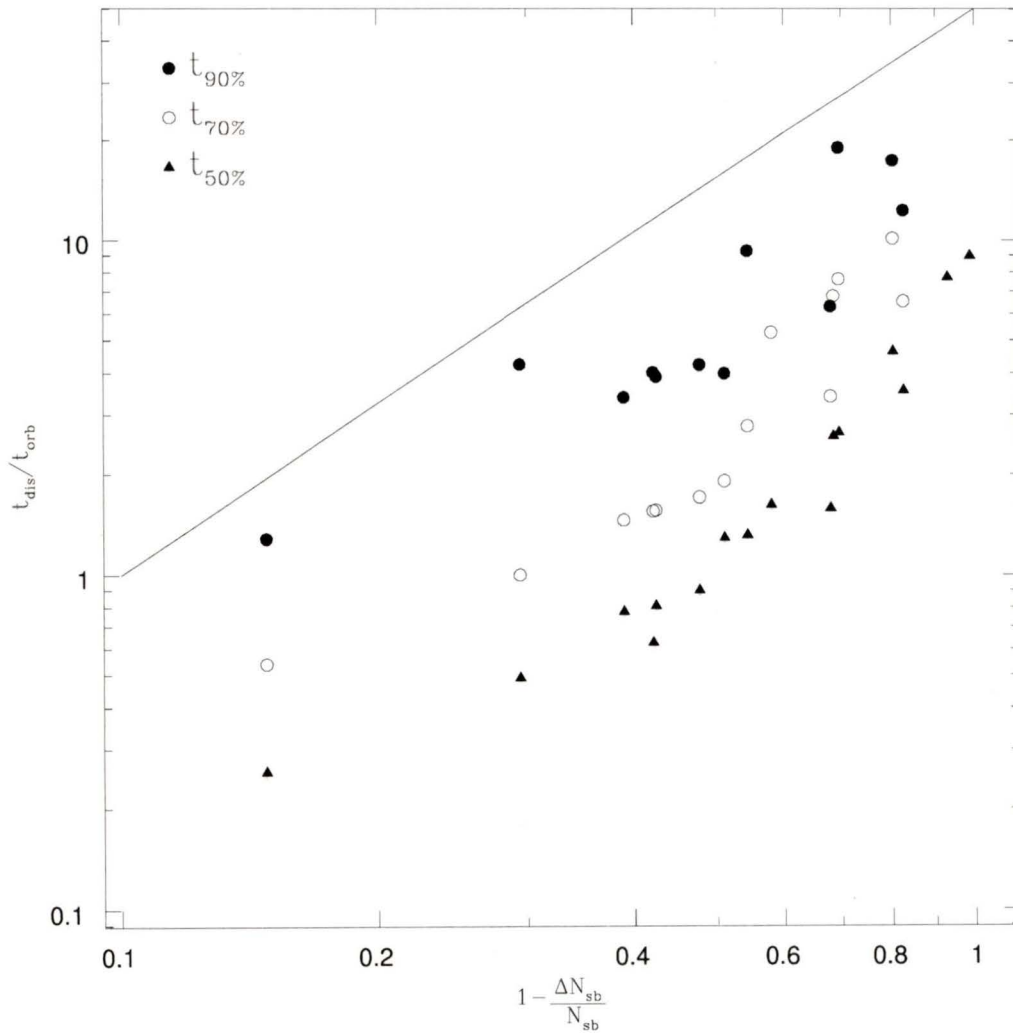


Figure 3.8: Disruption timescales as a function of remaining self-bound mass after the first orbit for optimally softened $N = 3000$ satellites on various orbits. Solid line shows the upper limit to the 90% disruption timescale ($t_{90\%}$) defined by equation (3.1).

in equation (2.14).

2. randomly select 1000 particles from this halo: each of these particles represents a satellite galaxy in the cluster.
3. calculate orbital parameters, r_{ap} , r_{per} , and t_{orb} for each satellite particle assuming an analytic NFW potential with the same scale radius and concentration as the halo generated in step 1.
4. project the position and velocity of each satellite onto its orbital plane and calculate its orbital path from initial time $t = 0$ to final time $t = t_{fin}$.
5. use the impulse approximation to estimate the fraction of mass lost by each satellite in its first orbit.
6. predict the disruption time for each satellite using the $t_{dis} - \Delta m$ relation.
7. identify all satellites with predicted disruption times greater than t_{fin} as surviving substructure. The final position of each satellite is given by its clustercentric distance at $t = t_{fin}$.

Note that, to be precise, the $t_{dis} - \Delta m$ relation we derived in Section 3.1 actually predicts the disruption time of a satellite assuming it starts orbiting the cluster from apocentre. Since the velocities of our satellite particles are distributed isotropically by construction, half of our satellite particles will pass through apocentre before reaching pericentre and vice versa for the other half. As a result, the $t_{dis} - \Delta m$ relation will underestimate the disruption times of the former by $\leq t_{orb}$ and overestimate t_{dis} for the latter by the same margin. Presumably these errors will offset one another given a sufficiently large sample of satellites.

In order to compare our results with a high resolution cluster formation simulation we adopt the cosmological parameters used by Ghigna *et al.* (1998; 2000) and Moore *et al.* (1999) in their $N = 5 \times 10^6$ Virgo cluster simulation. Specifically, we assume

a standard CDM (SCDM) universe with $\Omega = 1$ and $H_0 = 50$ km/s/Mpc. The Hubble time and age of the universe in this cosmology are $t_H \equiv 1/H_0 \simeq 19.6$ Gyr and $t_0 \simeq 13.1$ Gyr, respectively. The simulated Virgo cluster has a virial radius $R_{vir} = 1.0h^{-1}$ Mpc and a mass within this radius $M_{vir} \simeq 2 \times 10^{14}h^{-1} M_\odot$ (Ghigna *et al.*, 2000). The cluster forms at a redshift $z \sim 0.8$ (Ghigna *et al.*, 1998) which implies an age of 7.6 Gyr. For comparison, the crossing time of the cluster, $T_{cross} = \sqrt{R_{vir}^3/G M_{vir}} \simeq 2.1$ Gyr. We calculate our model for several different values of t_{fin} in order to obtain snapshots of the cluster at progressive stages in its dynamical evolution. Figure 3.9 shows a comparison of the distribution of orbital parameters, r_{ap} , r_{per} , $r_{ap} : r_{per}$, and t_{orb} of the initial and surviving satellites after 7.6 Gyr and 13.1 Gyr.

As expected, satellites on orbits that take them close to the centre of the cluster are prematurely disrupted. Over a Hubble time this depopulates the cluster exclusively of satellites with $r_{ap} \lesssim 3 R_s$ and $r_{per} \lesssim 2 R_s$. The median apocentric and pericentric radii of surviving satellites increases by $\sim 1 R_s$ and $\sim 0.3 R_s$, respectively. The cutoff in the distribution of apocentric radii is relatively sharp: virtually all satellites with $r_{ap} \lesssim 2 R_s$ are disrupted, whereas all satellites with $r_{ap} \gtrsim 3 R_s$ survive for at least a Hubble time. In comparison, the distribution of pericentric radii is depleted quite evenly between $0.1 R_s \lesssim r_{per} \lesssim 1 R_s$ and all satellites with $r_{per} > 2 R_s$ avoid disruption over a Hubble time. Interestingly, this results in a sampling of disrupted satellites from a wide range of apocentre-to-pericentre ratios between 1:1 and 10:1. Consequently the median $r_{ap} : r_{per}$ of satellite particles in our NFW cluster halo remains approximately 4:1 over the course of a Hubble time. In comparison, the median apocentre-to-pericentre ratio of satellites found in cosmological simulations ranges from 4:1 (van den Bosch *et al.*, 1999) to 6:1 (Ghigna *et al.*, 1998).

The evolution of the distribution of radial periods is similar to that of the apocentric radii, featuring a fairly abrupt transition from the totally depopulated part of the distribution ($t_{orb} \lesssim T_{cross}$) to the unchanged portion of the distribution ($t_{orb} \gtrsim 2 T_{cross}$).

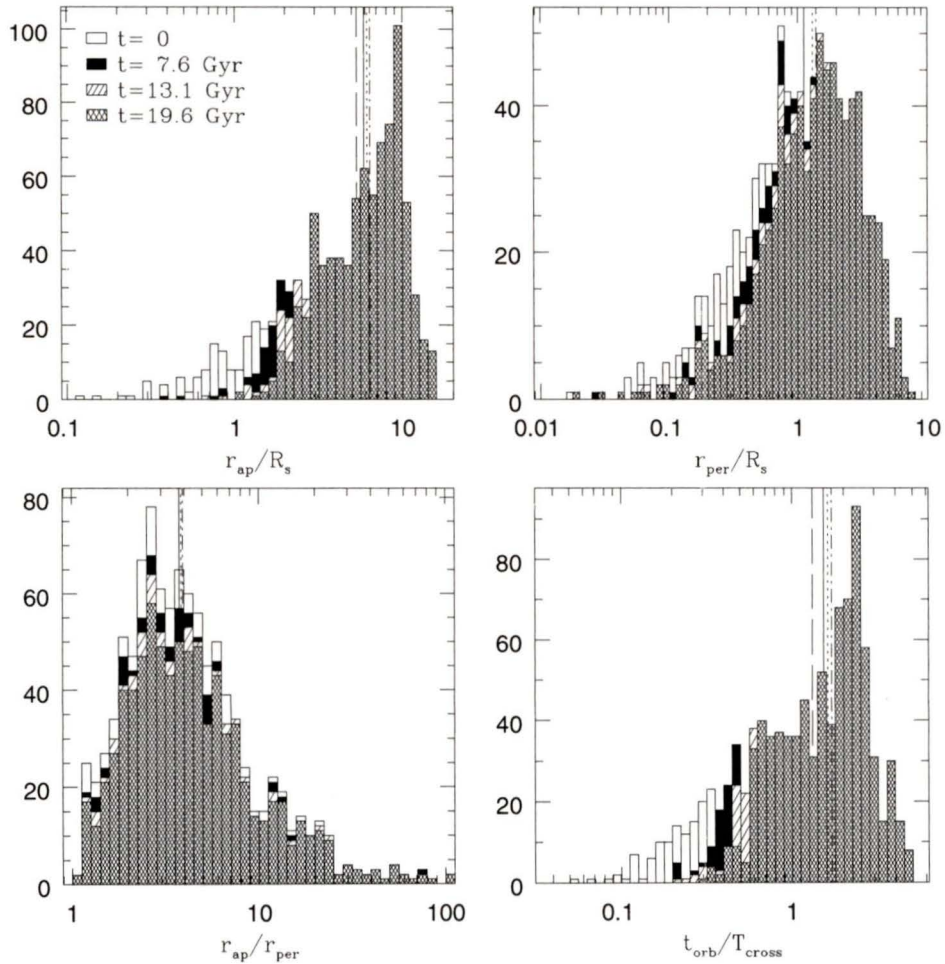


Figure 3.9: Distribution of orbital parameters of initial and surviving satellite galaxies, where apocentric and pericentric radii, r_{ap} and r_{per} , are given in units of the cluster scale radius R_s , and radial periods, t_{orb} , are in units of the crossing time of the cluster, $T_{cross} = \sqrt{R_{vir}^3/G M_{vir}}$. Long-dashed, solid, short-dashed, and dot-dashed lines show median values for times $t = 0$, $t = 7.6$ Gyr (age of cluster), $t = 13.1$ Gyr (age of universe), and $t = 19.6$ Gyr, respectively. Histograms are overlapped such that each distribution is a subset of the distribution at earlier time, i.e. distribution at time $t = 0$ includes distributions shown for all other times, etc.

Obviously, satellites whose radial periods are longer than twice the length of time for which the model was evolved (i.e. $t_{orb} \gtrsim 2 t_{fin}$) are unlikely to be disrupted since most mass loss occurs near pericentric passage, on average at time $t = t_{orb}/2$. Conversely, satellites with comparatively short radial periods are necessarily those that orbit within the central regions of the cluster, and therefore experience stronger tidal forces and more severe mass loss in addition to a greater number of pericentric passages during time t_{fin} .

The number density, $n(R)$, and cumulative fraction of surviving satellites, $N_{sur}(< R)/N_{sur}$, as a function of clustercentric distance, R , is shown in time sequence in Figure 3.10. The depopulation of satellites in the inner regions ($R \lesssim 1 R_s$) of the cluster is clearly evident in the time evolution of the number density profile. After 13.1 Gyr the innermost point ($R \simeq 0.5 R_s$) in the density profile of surviving halos is down by a factor of two relative to the initial density at the corresponding radius. Since the density of satellites in the outer regions of the cluster ($R \gtrsim 2 R_s$) remains virtually unchanged over a Hubble time, this results in a significant change in the overall shape of the density profile. The slope of the density profile of surviving satellites becomes shallower in the central $\sim 1 R_s$ of the cluster, and after a Hubble time a flat core of constant density has developed. Furthermore, the cumulative fraction of remaining satellites plotted in the lower panel of Figure 3.10 shows that the fraction of halos within $1 R_s$ of the cluster centre, initially greater than 10%, has dropped by more than half after 7.6 Gyr, and that after a Hubble time the central region is essentially devoid of substructure.

The number of surviving satellite halos is plotted as a function of time in Figure 3.11. Over a Hubble time satellites are disrupted at a fairly constant rate; the number of remaining satellites decreases by $\sim 10\%$ after 7.6 Gyr, $\sim 15\%$ after 13.1 Gyr, and $\sim 20\%$ after a Hubble time (19.6 Gyr). The inset of Figure 3.11 shows that most satellites are predicted to survive for much longer than a Hubble time. This supports the notion that given sufficient numerical resolution, cosmological simulations are

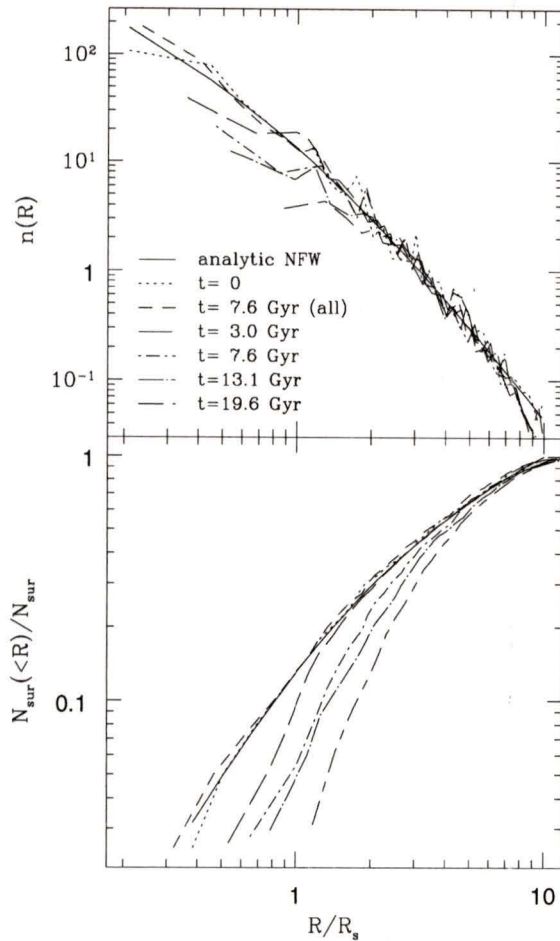


Figure 3.10: Time evolution of number density (upper) and cumulative fraction (lower) of surviving satellites as a function of clustercentric distance in units of the cluster halo scale radius, R_s . Profiles are calculated in bins of 25 satellite particles each. Initial analytic NFW profile and profiles of “all” (surviving as well as disrupted) are shown for reference along with profiles of surviving satellites at various times including 7.6 Gyr (estimated time since formation of cluster), 13.1 Gyr (age of universe), and 19.6 Gyr (Hubble time), assuming an SCDM ($\Omega = 1$, $\Lambda = 0$, $H_0 = 50$ km/s/Mpc) cosmology.

indeed capable of resolving much substructure in cluster halos. Tidal disruption erases only substructure near the centre of the cluster leaving the spatial distribution of the majority of satellite halos at $R \gtrsim 2 R_s$ relatively unchanged.

3.3 Comparison with Other Work

We are finally in a position to compare the predictions of our toy model with the results of cosmological simulations as well as observations of the spatial distribution of galaxies in clusters. The fractional number density of subhalos predicted by our model is compared with that of the aforementioned $N = 5 \times 10^6$ Virgo cluster simulation in Figure 3.12. The simulation data is taken directly from Figure 10 of Ghigna *et al.* (2000). It is important to note that one of the main results presented by Ghigna *et al.* (2000) and Moore *et al.* (1999; 1998) is that at “ultra-high” resolution the density profile of dark matter halos in cosmological simulations converges to an inner slope steeper than that of the NFW profile. The Moore *et al.* profile is of the form

$$\rho_{Moore}(r) = \frac{\rho_0}{(r/r_s)^{1.5}(1+r/r_s)^{1.5}} \quad (3.2)$$

where $\rho_{Moore}(r < r_s) \propto r^{-1.5}$ in contrast to the NFW profile where $\rho_{NFW}(r < r_s) \propto r^{-1}$. According to Moore *et al.* (1999), a scale radius of $r_s = 0.25 r_{vir}$, i.e. a concentration of $c \equiv r_{vir}/r_s = 4.0$, provides a good fit to the density profile of their Virgo cluster. Over the range of radii plotted in Figure 10 of Ghigna *et al.* (2000) ($r \gtrsim 0.05 r_{vir}$), however, an NFW profile with concentration $c = 7.1$ provides an equally good fit to the particle density distribution.

We choose to simply normalize our toy model density profiles to the virial radius and overlay them on the Virgo simulation results rather than attempt a more complicated renormalization scheme. Although our $c = 10$ halo profile is slightly more concentrated than the Moore *et al.* and NFW profiles that best fit the cluster

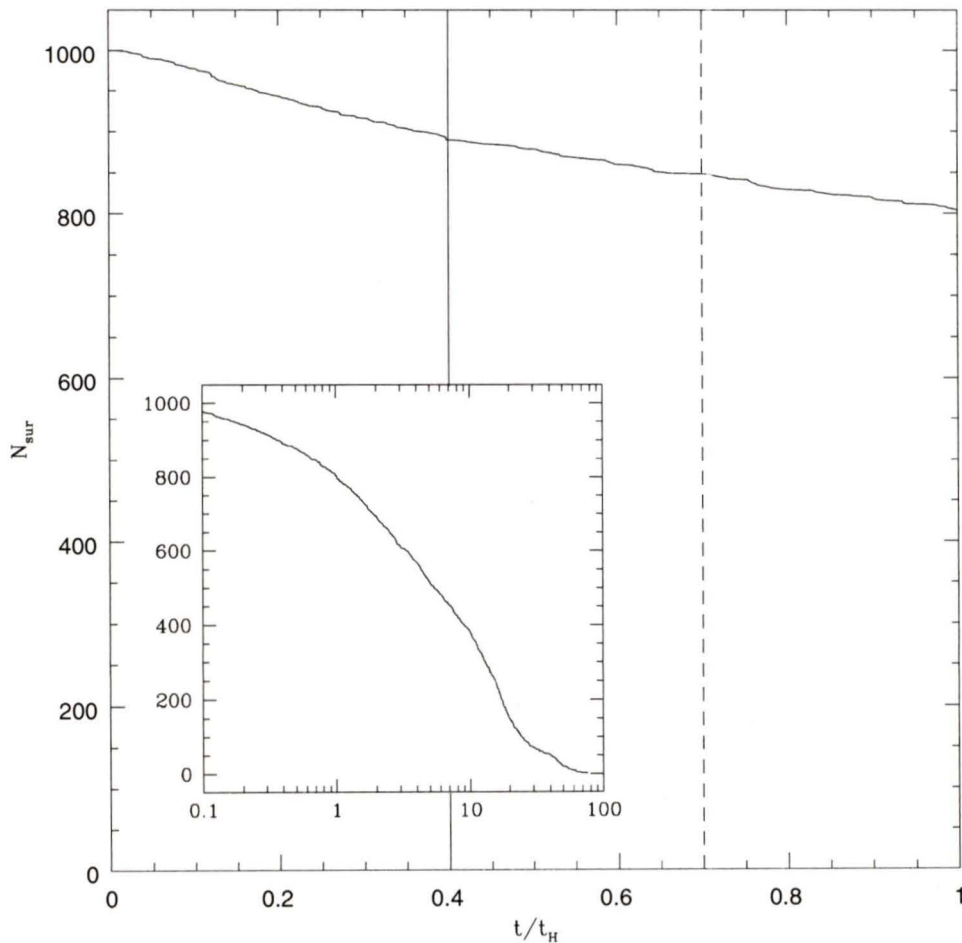


Figure 3.11: Number of surviving satellite galaxies as a function of time over a Hubble time, $t_H = 19.6$ Gyr, assuming $H_0 = 50$ km/s/Mpc. Solid and dashed vertical lines show the age of a typical cluster (7.6 Gyr), and the age of the universe (13. Gyr) in an SCDM ($\Omega = 1, \Lambda = 0$) cosmology, respectively. Inset shows time evolution of number of surviving satellites over all time in units of a Hubble time (on a logarithmic scale).

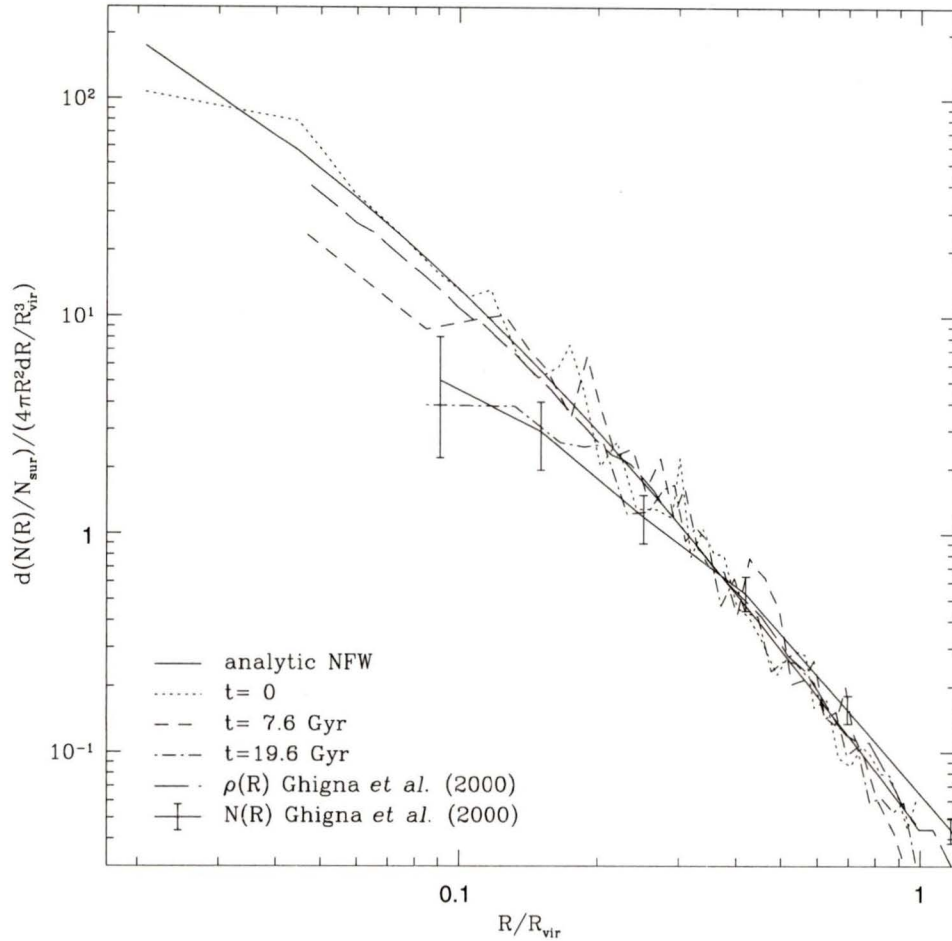


Figure 3.12: Fractional number density of surviving subhalos as a function cluster-centric distance in units of the cluster virial radius, R_{vir} . Number density profiles of satellites predicted to survive beyond the age of the Ghigna *et al.* (2000) Virgo cluster (7.6 Gyr) and beyond a Hubble time ($t_H = 19.6$ Gyr) assuming an SCDM cosmology ($\Omega = 1, \Lambda = 0, H_0 = 50$ km/s/Mpc) are plotted along with initial and analytic NFW profiles of the toy model halo. Also shown are the mass density and number density of subhalos with circular velocities $v_{circ} > 80$ km/s (with $1 - \sigma$ Poisson error bars) of the simulated cluster at $z = 0$ (see Figure 10 of Ghigna *et al.* (2000))

halo, this difference is inconsequential at the level of accuracy of this comparison. Figure 3.12 shows that the distribution of subhalos in the cosmological simulation is significantly underdense with respect to the mass in particles. (Note that the mass bound to substructure in the simulated Virgo cluster is less than 10% of the mass within its virial radius; most of the mass of the cluster is in the smooth background density of particles.) Ghigna *et al.* (2000) describe this as an “antibiassing” of the substructure halos relative to the mass density. Our toy model suggests that this antibias is primarily due to a disruption of substructure by strong tidal forces in the central regions of the cluster. Interestingly, we find excellent agreement between the simulation results and the number density profile of satellites which survive for longer than a Hubble time according to our model, despite the fact that this is ~ 2.5 times longer than the age of the cluster in the cosmological simulation. This may be partially a reflection of our conservative choice for the intercept constant in the $t_{dis} - \Delta m$ relation, equation (3.1). In other words, having cautiously overestimated disruption timescales of satellite halos, it is not surprising that a longer period of dynamical evolution is required to match the simulation results. Furthermore, the disruption of subhalos is accelerated in cosmological cluster simulations by a host of non-negligible secondary disruption mechanisms, such as interactions between the subhalos themselves, which we do not account for in our simple model. Our results suggest that the net effect of these processes is roughly equivalent to uniformly decreasing the disruption timescales of all satellites as a function of their initial mass loss, i.e. decreasing the value of the slope and/or intercept constants in the $t_{dis} - \Delta m$ relation. This would enable us to reproduce the good agreement in number density we obtain for a Hubble time’s worth of dynamical evolution using a more realistic timescale such as the age of the cluster.

In Figure 3.13 we attempt to compare our findings with observations of real galaxy clusters from the CNOC cluster redshift survey (Yee, Ellingson & Carlberg, 1996). The surface number density of profile of galaxies plotted in Figure 3.13 is

that of an “ensemble” cluster constructed by overlaying 1150 galaxies from 14 X-ray clusters (Carlberg, Yee, & Ellingson, 1997). Eke, Navarro, & Frenk (1998) find that the resulting profile is well fit by the average projected dark matter density profile of 10 N -body/gasdynamical cluster simulations. This is shown in Figure 3.13 as an analytic NFW surface density profile (given in Appendix A) with the same scale radius, $r_s \simeq 0.15 r_{vir}$ as the “average” ($z = 0$) profile presented in their Table 1. The only free normalization is that of the dark matter density, which has been chosen to match the galaxy number density data. These authors conclude from the similarity between the dark matter and galaxy profiles that there is little evidence for spatial segregation or dynamical bias of galaxies with respect to the mass distribution in clusters, and that the structure of clusters is consistent with the assumption that galaxies are fair tracers of mass. Note that these simulations were performed at relatively low resolution by today’s standards; each cluster was simulated with a maximum of 64,000 gas particles and an equal number of dark matter particles. Consequently, they were unable to resolve substructure in their clusters, hence their comparisons with observations were made using the mass density profile, as opposed to the number density of subhalos.

The projected number density of surviving satellite halos was calculated by integrating the volume number density $n(R)$ along the line-of-sight (Binney & Tremaine, 1987):

$$\Sigma_N(R_p) = 2 \int_{R_p}^{\infty} \frac{n(R)R}{\sqrt{R^2 - R_p^2}} dR \quad (3.3)$$

where R_p is the projected clustercentric radius. Unfortunately, because each satellite’s orbit was integrated in the orbital plane of the satellite, in two dimensions only, the position of each satellite particle at time $t = t_{fin}$ is known only in terms of its clustercentric distance. As a result, we are unable to project the positions of our satellite particles onto a common plane simply by selecting two of three orthogonal coordinates. Instead, we integrate equation (3.3) numerically in order to transform

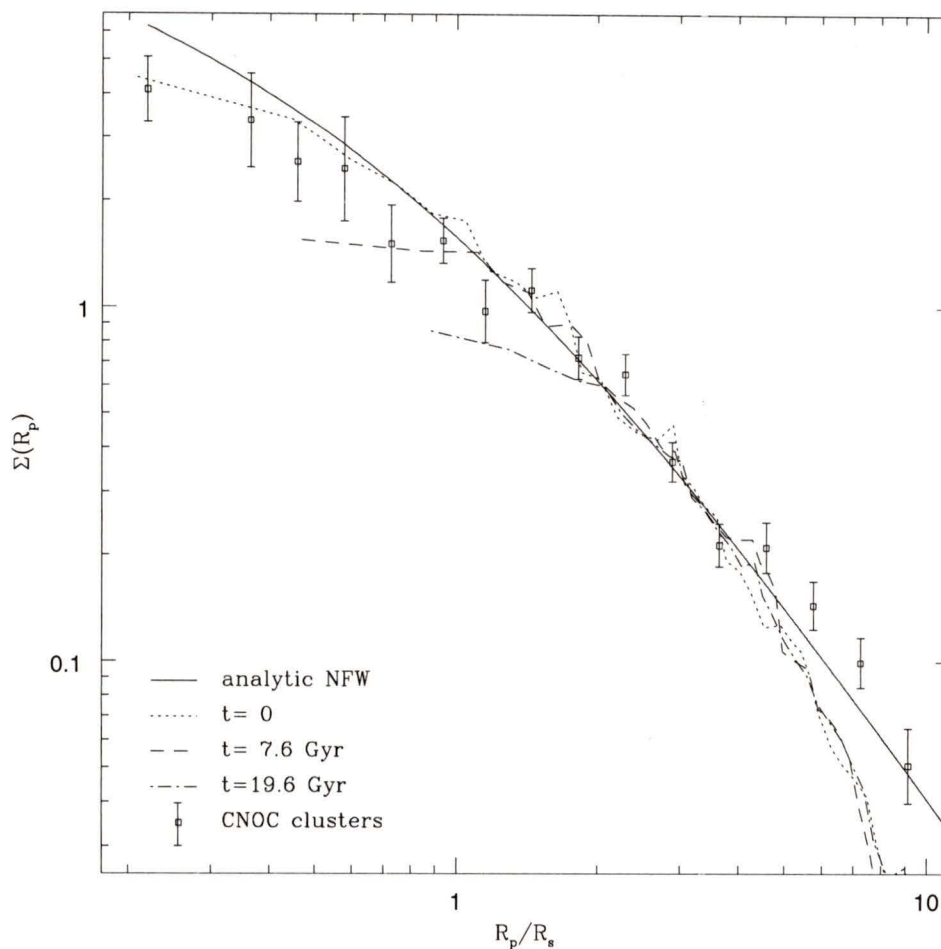


Figure 3.13: Surface number density profile of galaxies in the CNOC ensemble cluster (Carlberg, Yee, & Ellingson, 1997), analytic NFW fit to average projected dark matter mass density profile of 10 simulated clusters (Eke, Navarro, & Frenk, 1998), and projected number density of surviving satellite halos as predicted by our model as a function of projected clustercentric radius, R_p , in units of the scale radius, R_s . The analytic and subhalo profiles are scaled arbitrarily in the vertical direction to match the galaxy profile.

from volume density to surface density.

The projected number density of surviving subhalos predicted by our model shows the same underdensity, or antibias, relative to the initial number density and mass density of the cluster halo as was observed previously in volume density. Note that the discrepancy between the analytic NFW surface density and the projected density of subhalos at large projected radii, $R_p \sim R_{vir}$, is primarily due to the finite extent of our cluster halo. The analytic NFW surface density is derived by integrating the NFW volume density along the line-of-sight from negative to positive infinity. At projected radii close to the virial radius of the halo, most of the mass along the line-of-sight is in fact exterior to the virial radius of the halo in three dimensions. Conversely, the surface density of a truncated NFW halo approaches zero as the projected radius approaches the virial radius. Due to the scatter and magnitude of error in the observations, the number density of halos which survive longer than 7.6 Gyr remains consistent with the CNOC data. Over a Hubble time, however, the number density profile develops a flat, low density core which is not consistent with the observed surface density of galaxies. Although the surviving subhalo profile is within error for two of four possible data points at $R_p < 0.2R_{vir}$, its asymptotic slope is clearly shallower than that of the observed galaxy profile. As usual a more complete observational data set would likely improve constraints on the theoretical models. In addition, as a result of our two-dimensional integration of satellite orbits, our projected density profile is limited to values of R_p greater than the radius of the innermost bin in our volume number density profile. Three-dimensional positions for our satellite halo particles would allow us to probe to smaller R_p since bins in projected radius are concentric cylinders in three-space which extend indefinitely along the line of sight, and therefore encompass more satellite particles (per unit R_p) compared to spherical bins in three dimensional clustercentric radius (per unit R).

3.4 Limitations and Future Work

The toy cluster model presented here is a much simplified version of the cluster formation observed in cosmological simulations. Structure forms in these simulations via a complicated sequence of satellite accretions and halo mergers which build progressively larger halos from a hierarchy of smaller ones. Our model essentially treats the substructure in a cluster as a collection of independent satellites and considers their disruption solely via tidal stripping by the cluster potential. Many secondary physical effects which influence the dynamical evolution of cluster subhalos have been neglected in our simple model, most notably dynamical friction and halo-halo encounters, which we discuss below. The advantage of this approach is that our results can be understood in terms of the well known physics of tidal stripping. The details of even the most fundamental secondary processes such as dynamical friction continue to remain poorly understood (van Kampen, 2000b).

Dynamical friction is the process of orbital decay due to the gravitational interaction between the mass of the satellite and the medium in which it is orbiting. In general this effect tends to accelerate the disruption of the massive satellites by dragging its orbit closer to the cluster centre, thereby exposing it to stronger tidal forces. By the same token, however, the central regions of the cluster may temporarily become populated by these satellites, whose orbits have decayed but who have not yet been fully disrupted. According to the timescales for dynamical friction estimated using equation (2.16) (see also Table 3.1), this effect is not significant for the satellite mass we have chosen in our model. Nevertheless, since the dynamical friction timescale is proportional to ratio of the mass of the cluster to that of the satellite, this effect might become significant if a more realistic spectrum of satellite masses were included in our model.

Halo-halo interactions were found to contribute significantly to tidal heating of satellite halos by Moore, Katz, & Lake (1996). High speed encounters between subha-

los may in fact be responsible for the morphological transformation of cluster galaxies from spirals to dwarf spheroidals (Moore *et al.*, 1996). The cross section for mergers between satellite halos is extremely small, however, therefore it is unlikely that larger subhalos might be formed from the collision of two satellites. We therefore expect that the net effect of halo-halo encounters is to enhance disruption of substructure halos.

In addition to these missing physical processes, our model lacks the detailed satellite mass spectrum and accretion history that numerous authors have successfully incorporated into semi-analytic models for hierarchical structure formation (Kauffmann, *et al.*, 1999; Somerville & Primack, 1999; Cole *et al.*, 2000; Taylor & Babul, 2001). All of the simulations and models we have developed consist of satellites 300 times less massive than the cluster they inhabit. In addition, we initiate our model with all 1000 satellites already in place within the virial radius of the cluster. As a result, our model is somewhat inconsistent in that the total mass in satellites actually exceeds the virial mass of the cluster potential. A higher level of sophistication would require the use of Press-Schechter-type merger trees (Press & Schechter, 1974) to determine the accretion time, t_{acc} of each satellite. This would effectively increase satellite disruption times by changing the criterion for survival to $t_{acc} + t_{dis} > t_{fin}$. Adding satellites according to their accretion times, one could also build up the cluster halo in a self-consistent manner. However, incorporating such a time-varying potential into the model would undoubtedly complicate both the implementation of the model and the subsequent interpretation of its results.

3.5 Summary

We have developed a toy model for cluster formation that allows us to investigate the tidal disruption of substructure by the cluster potential. Strong tidal forces erase much of the substructure in the central regions of the cluster, leaving a distribution of

surviving subhalos that is underdense relative to the mass distribution of the cluster within $1 R_s$ of the cluster centre. This result is in agreement with the cosmological simulations of Ghigna *et al.* (2000), who find an antibias in the subhalo profile with respect to the particle density. Our model suggests that this antibias is primarily due to the tidal disruption of subhalos in densest region of the cluster.

The projected density profile of surviving subhalos after a Hubble time is marginally inconsistent with the surface number density of galaxies in the CNOC ensemble cluster. Although this result is weakened somewhat by scatter and error in the observational data, the lack of surviving substructure in the central regions of our toy model seems difficult to reconcile with the fact that a substantial fraction of cluster galaxies are observed near the centre. This implies that, even in the limit of infinite numerical resolution, collisionless N -body simulations are inadequate to properly model the formation and dynamical evolution of galaxies in clusters. The inclusion of a dissipational hydrodynamic component, i.e. gas, is therefore an essential ingredient in cluster formation simulations. As gas collapses in the gravitational potential of the dark matter, it dissipates energy radiatively and loses pressure support. This results in highly concentrated cores which might be dense enough to survive tidal disruption in the innermost regions of the cluster potential. If so, the number density profile of the baryonic cores would not suffer from the antibias that was observed in the distribution of surviving subhalos predicted by our model and seen in cosmological simulations. This would explain the good agreement between the average projected dark matter density profile found in Eke, Navarro, & Frenk's (1998) cluster simulations and the observed surface number density of galaxies in the CNOC ensemble cluster, since the baryonic cores would be fairer tracers of the mass distribution.

Chapter 4

Concluding Remarks

Is overmerging solved? The latest generation of cosmological simulations clearly demonstrate that with sufficient numerical resolution, one can resolve an abundance of substructure in the virialized regions of galaxy cluster halos. Our simulations of a single satellite in a cluster potential also indicate that numerical effects can contribute significantly to the disruption of substructure halos. However, the cluster model we have developed based on the timescales for tidal disruption of satellite halos suggests that, even in the limit of infinite numerical resolution, overmerging due to physical processes is sufficient to erase virtually all substructure within a scale radius of the centre of the cluster.

This implies that a dissipational hydrodynamic component is needed to properly model the dynamics of galaxy cluster, as was originally proposed by White and Rees (1978). In their model for galaxy formation gas cools radiatively as it collapses in the potential wells of dark matter halos, forming highly concentrated luminous cores. These tightly bound knots of gas are overdense with respect to the dark matter, and therefore much more resistant to tidal disruption. *N*-body/gasdynamical simulations have subsequently confirmed the basic elements of the “core condensation in heavy halos” theory (1992; 1996; 1998).

Incorporating baryonic physics into our model is an obvious avenue for future work. Repeating our single satellite simulations with the inclusion of a hydrodynamical component would allow us to investigate the effects of dissipation in detail. In particular, we would like to determine the effect of gas physics on the central density of the satellite and its consequences for disruption timescales. A revised $t_{dis} - \Delta m$ relation would allow us to reconstruct the spatial distribution of baryonic galaxy cores and repeat our comparisons with the dark matter mass profile and the observed cluster galaxy surface density.

Possible improvements to our model include the use of semi-analytic merger histories to generate a realistic distribution of mass and accretion times for infalling satellites as discussed previously in Chapter 3. Incorporating a prescription for dynamical friction based on Chandrasekhar's formula (Chandrasekhar, 1943) would also improve the accuracy of our model. Halo-halo encounters could be included as in Moore, Katz, & Lake (1996), by representing perturbing galaxies as analytic potentials orbiting along with the single live satellite halo in the main cluster potential.

A more ambitious version of our model would involve verifying our disruption timescale predictions by actually simulating each of the 1000 satellites in the static potential of the cluster. This is well within the capabilities of a moderately-sized cluster of workstations, and could easily be organized using a software package like Condor to manage distributed computational resources.¹ More sophisticated parallel N -body codes might also be used to incorporate a live cluster halo in order to directly simulate the effects of dynamical friction.

Finally, we would like to analyze a high resolution cosmological cluster simulation like that of Ghigna *et al.* (2000) in order to verify the antibias observed in the subhalo number density. A statistical comparison of the disruption timescales of subhalos in

¹Condor is "a software system that creates a High-Throughput Computing (HTC) environment by effectively harnessing the power of a cluster of UNIX workstations on a network" (see the Condor Project Homepage at <http://www.cs.wisc.edu/condor/> for further details).

the fully self-consistent simulation with those predicted by our model might lead to further insight about the relative importance of secondary dynamical processes as well as numerical effects such as heating of subhalos by the background density N -body particles in the cluster halo.

Appendix A

Properties of the NFW Model

The NFW density profile is characterized by a $1/r$ dependence at radii much less than the scale radius r_s and a $1/r^3$ dependence at large radii. The following form is convenient for our purposes:

$$\rho(r) = \frac{M_{vir}}{4\pi r_s^3 f(c) r/r_s (1 + r/r_s)^2} \quad (\text{A.1})$$

$$f(x) \equiv \ln(1 + x) - \frac{x}{1 + x} \quad (\text{A.2})$$

$$c \equiv \frac{r_{vir}}{r_s} \quad (\text{A.3})$$

where M_{vir} and r_{vir} are the virial mass and radius, respectively, and c is the halo concentration. The corresponding mass profile is

$$M(r) = M_{vir} \frac{f(r/r_s)}{f(c)} \quad (\text{A.4})$$

The surface density is given by integrating the volume density over the line-of-sight (Bartelmann, 1996):

$$\Sigma(R) = 2 \int_R^\infty \frac{\rho(r)r}{\sqrt{r^2 - R^2}} dr \quad (\text{A.5})$$

$$= \frac{2 \rho_0 r_s}{x} \begin{cases} 1 - \frac{2}{\sqrt{x^2-1}} \arctan \sqrt{\frac{x-1}{x+1}} & x > 1 \\ 1 - \frac{2}{\sqrt{1-x^2}} \operatorname{arctanh} \sqrt{\frac{1-x}{1+x}} & x < 1 \\ 0 & x = 1 \end{cases} \quad (\text{A.6})$$

The gravitational potential, obtained by integrating Poisson's equation, is

$$\Phi(r) = -\frac{GM_{vir} \ln(1+r/r_s)}{r_s f(c) r/r_s} \quad (\text{A.7})$$

where G is the gravitational constant. The potential energy within radius r is defined by

$$\Omega(r) = 2\pi \int_0^\infty \rho(r') \phi(r', r) r'^2 dr' \quad (\text{A.8})$$

$$\phi(r', r) = -4\pi G \left[\frac{1}{r'} \int_0^{r'} \rho(r'') r''^2 dr'' + \int_{r'}^r \rho(r'') r'' dr'' \right] \quad (\text{A.9})$$

The solution for an infinite NFW density profile is

$$\Omega(r) = -\frac{GM^2(1+c)^2(r^2 + 2rr_s - 2r_s^2(1+r/r_s) \ln(1+r/r_s))}{2((1+c) \ln(1+c) - c)^2 r_s^2 (1+r/r_s)^2} \quad (\text{A.10})$$

The kinetic energy of a spherical, isotropic model as a function of radius is given by

$$K(r) = 6\pi \int_0^r \rho(r) \overline{v_r^2} r^2 dr \quad (\text{A.11})$$

where $\overline{v_r^2}$ is the one-dimensional velocity dispersion obtained by solving the spherical Jeans equation (Hernquist, 1993):

$$\overline{v_r^2} = \frac{1}{\rho(r)} \int_r^\infty \rho(r) \frac{d\Phi}{dr} dr \quad (\text{A.12})$$

$$= \frac{1}{\rho(r)} \int_r^\infty \rho(r) \frac{GM(r)}{r^2} dr \quad (\text{A.13})$$

Bibliography

- Aarseth, S.: 1963, *M.N.R.A.S.* **126**, 223
- Aguilar, L. A., and White, S. D. M.: 1985, *Astrophys. J.* **295**, 374
- Bartelmann, M.: 1996, *Astron. & Astrophys.* **313**, 697
- Bullock, J. S., Kravtsov, A. V., and Weinberg, D. H. : 2000, *Astrophys. J.* **539**, 517
- Chandrasekhar : 1943, *Astrophys. J.* **97**, 255
- Cole, S., Lacey, C. G., Baugh, C. M., and Frenk, C. S.:2000 *M.N.R.A.S.* **319**, 168
- Benz, W., Bowers, R. L., Cameron, A. G. W., and Press, W. H.: 1990, *Astrophys. J.* **348**, 647
- Binney, J., Gerhard, O., and Silk, J.: 2001, *M.N.R.A.S.* **321**, 471
- Binney, J., and Tremaine, S.: 1987, *Galactic Dynamics*, Princeton University Press.
- Blumenthal, G. R., Faber, S. M., Primack, J. R., and Rees, M. J. : 1984, *Nature* **311**, 517
- Carlberg, R. G.: 1994, *Astrophys. J.* **433**, 468
- Carlberg, R. G., Yee, H. K., Ellingson, E.: 1997, *Astrophys. J.* **478**, 462
- Eke, V. R., Navarro, J. F., and Frenk, C. S. : 1998, *Astrophys. J.* **503**, 569
- Farouki, R. T., and Salpeter E. E. : 1982, *Astrophys. J.* **253**, 512
- Ghigna, S., Moore, B., Governato, F., Lake, G., Quinn, T., and Stadel, J. : 1998, *M.N.R.A.S.* **300**, 146
- Ghigna, S., Moore, B., Governato, F., Lake, G., Quinn, T., and Stadel, J. : 2000, *Astrophys. J.* **544**, 616

- Heisler, J., and White, S. D. M.: 1990, *M.N.R.A.S.* **243**, 199
- Hernquist, L.: 1990, *Astrophys. J.* **356**, 395
- Hernquist, L.: 1993, *Astrophys. J. Supp.* **86**, 389
- Katz, N., Weinberg, D. H., and Hernquist, L.: 1992, *Astrophys. J.* **399**, L109
- Katz, N., Weinberg, D. H., and Hernquist, L.: 1996, *Astrophys. J. Supp.* **105**, 19
- Kauffmann, G., Colberg, J. M., Diaferio, A., and White, S. D. M.: 1999, *M.N.R.A.S.* **303**, 188
- Klypin, A. Gottlöber, S., and Kravtsov, A. V.: 1999, *Astrophys. J.* **516**, 530
- Klypin, A., Kravtsov, A. V., Valenzuela, O., and Prada, F. : 1999, *Astrophys. J.* **522**, 82
- Lacey, C., and Cole, S.: 1993, *M.N.R.A.S.* **262**, 627
- Lake, G., Katz, N., Quinn, T., Stadel, J.: 1995, *Parallel Processing for Scientific Computing*, p. 307, SIAM 1995
- Moore, B.: 2000, Preprint [astro-ph/0009247]
- Moore, B.: 2001, Preprint [astro-ph/0103100]
- Moore, B., Ghigna, S., Governato, F., Lake, G., Quinn, T., Stadel, J., and Tozzi, P.: 1999, *Astrophys. J.* **524**, L19
- Moore, B., Governato, F., Quinn, T., Lake, G., Stadel, J.: 1998, *Astrophys. J.* **499**, L5
- Moore, B., Katz, N., and Lake, G.: 1996, *Astrophys. J.* **457**, 455
- Moore, B., Katz, N., Lake, G., Dressler, A., Oemler, A. : 1996, *Nature* **379**, 613
- Moore, B., Quinn, T., Governato, F., Stadel, J., and Lake, G.: 1999, *M.N.R.A.S.* **310**, 1147
- Moore, G. E.: 1965, *Electronics* **38**, 8, p. 114
- Navarro, J. F., Benz, W. : 1991, *Astrophys. J.* **380**, 320
- Navarro, J. F., Frenk, C. S., and White, S. D. M. : 1996, *Astrophys. J.* **462**, 563
- Navarro, J. F., Frenk, C. S., and White, S. D. M. : 1997, *Astrophys. J.* **490**, 493
- Navarro, J. F., and White, S. D. M.: 1993, *M.N.R.A.S.* **265**, 271

- Peebles, P. J. E.: 1970, *Astron. J.* **75**, 13
- Peebles, P. J. E.: 1982, *Astrophys. J.* **263**, 1
- Press, W. H., and Schechter, P. : 1974, *Astrophys. J.* **187**, 425
- Press, W. H., Teukolsky, A. A., Vetterling, W. T., and Flannery, B. P.: 1992, *Numerical Recipes in Fortran: The Art of Scientific Computing, 2nd ed.*
- Somerville, R. S., and Primack, J. R. : 1999, *M.N.R.A.S.* **310**, 1087
- Spergel, D. N. and Steinhardt, P. J.:2000, *Phys. Rev. Lett.* **84**, 3760
- Springel, V., White, S. D. M., Tormen, G., and Kauffmann, G.: 2000, Preprint [astro-ph/0012055]
- Taylor, J. E., and Babul, A.: 2001, in preparation
- Thomas, P. A., and Couchman, H. M. P.: 1992, *M.N.R.A.S.* **257**, 11
- Tormen, G., Bouchet, F. R., and White, S. D. M.: 1997, *M.N.R.A.S.* **286**, 865
- Tormen, G., Diaferio, A., and Syer, D.: 1998, *M.N.R.A.S.* **299**, 728
- van den Bosch, F. C., Lewis, G. F., Lake, G., Stadel, J.: 1999,
- van Albada, G. B.: 1961, *Astron. J.* **66**, 10
- van Kampen, E. : 1995, *M.N.R.A.S.* **273**, 295
- van Kampen, E. : 2000, Preprint [astro-ph/0002027]
- van Kampen, E. : 2000, Preprint [astro-ph/0008453]
- Weinberg, D., Katz, N., and Hernquist, L.: 1998, *Origins, ASP Conference Series* **148**, 21 Preprint [astro-ph 9708213]
- White, S. D. M.: 1976, *M.N.R.A.S.* **177**, 717
- White, S. D. M., and Rees, M. J.: 1976, *M.N.R.A.S.* **183**, 341
- Widrow, L. M.: 2000, *Astrophys. J. Supp.* **131**, 39
- Yee, H. K., Ellingson, E., Carlberg, R. G.: 1996, *Astrophys. J. Supp.* **102**, 269

VITA

Surname: Hayashi

Given Names: Eric Jeffrey

Place of Birth: Ottawa, Ontario, Canada

Educational Institutions Attended:

University of Victoria	1998 – 2001
University of Guelph	1993 – 1998

Degrees Awarded:

B.Sc. (Honours) University of Guelph	1998
--------------------------------------	------

Honours and Awards:

University of Victoria Fellowship	1998 – 2000
R.M. Petrie Memorial Fellowship	1999
Copernicus Scholarship	1997
College of Physics and Engineering Sciences Dean's Scholarship	1995
Canada Scholarship	1993 – 1996


University of Victoria Partial Copyright Licence

I hereby grant the right to lend my dissertation to users of the University of Victoria Library, and to make single copies only for such users or in response to a request from the Library of any other university, or similar institution, on its behalf or for one of its users. I further agree that permission for extensive copying of this dissertation for scholarly purposes may be granted by me or a member of the University designated by me. It is understood that copying or publication of this dissertation for financial gain shall not be allowed without my written permission.

Title of Dissertation:

Tidal Disruption of Substructure in Galaxy Clusters

Author:


Eric Hayashi
April 28, 2001